Applied Computational Electromagnetics Society

Journal

May 2011 Vol. 26 No. 5

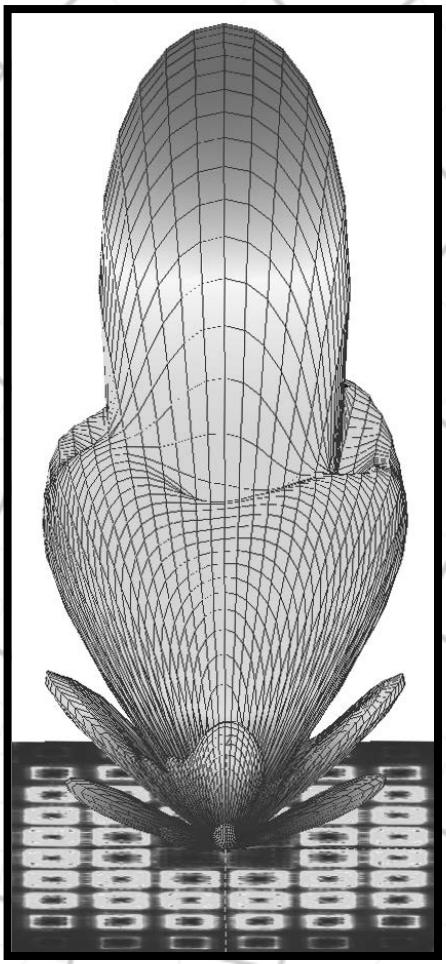

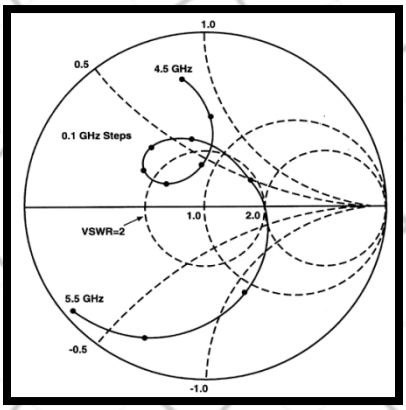

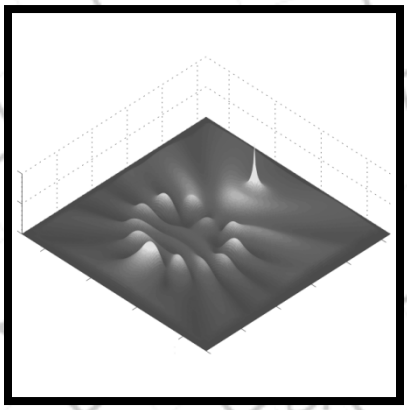

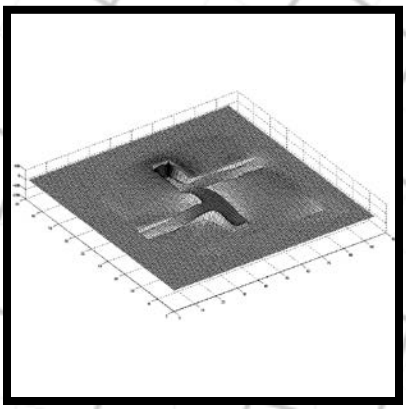

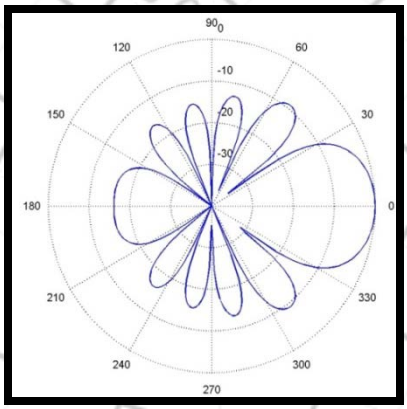

ISSN 1054-4887

GENERAL PURPOSE AND SCOPE: The Applied Computational Electromagnetics Society ***(ACES)*** Journal hereinafter known as the ***ACES Journal*** is devoted to the exchange of information in computational electromagnetics, to the advancement of the state-of-the art, and the promotion of related technical activities. The primary objective of the information exchange is to inform the scientific community on the developments of new computational electromagnetics tools and their use in electrical engineering, physics, or related areas. The technical activities promoted by this publication include code validation, performance analysis, and input/output standardization; code or technique optimization and error minimization; innovations in solution technique or in data input/output; identification of new applications for electromagnetics modeling codes and techniques; integration of computational electromagnetics techniques with new computer architectures; and correlation of computational parameters with physical mechanisms.

SUBMISSIONS: The ***ACES Journal*** welcomes original, previously unpublished papers, relating to applied computational electromagnetics. Typical papers will represent the computational electromagnetics aspects of research in electrical engineering, physics, or related disciplines. However, papers which represent research in applied computational electromagnetics itself are equally acceptable.

Manuscripts are to be submitted through the upload system of ***ACES*** web site http://aces.ee.olemiss.edu See "Information for Authors" on inside of back cover and at ***ACES*** web site. For additional information contact the Editor-in-Chief:

Dr. Atef Elsherbeni
Department of Electrical Engineering
The University of Mississippi
University, MS 386377 USA
Phone: 662-915-5382
Email: atef@olemiss.edu

SUBSCRIPTIONS: All members of the Applied Computational Electromagnetics Society are entitled to access and download the ***ACES Journal*** any published journal article available at http://aces.ee.olemiss.edu. Printed issues of the ***ACES Journal*** are delivered to institutional members. Each author of published papers receives a printed issue of the ***ACES Journal*** in which the paper is published.

Back issues, when available, are $50 each. Subscription to ***ACES*** is through the web site. Orders for back issues of the ***ACES Journal*** and change of address requests should be sent directly to ***ACES*** office at:

Department of Electrical Engineering
The University of Mississippi
University, MS 386377 USA
Phone: 662-915-7231
Email: aglisson@olemiss.edu

Allow four weeks advance notice for change of address. Claims for missing issues will not be honored because of insufficient notice, or address change, or loss in the mail unless the ***ACES*** office is notified within 60 days for USA and Canadian subscribers, or 90 days for subscribers in other countries, from the last day of the month of publication. For information regarding reprints of individual papers or other materials, see "Information for Authors".

LIABILITY. Neither ***ACES***, nor the ***ACES Journal*** editors, are responsible for any consequence of misinformation or claims, express or implied, in any published material in an ***ACES Journal*** issue. This also applies to advertising, for which only camera-ready copies are accepted. Authors are responsible for information contained in their papers. If any material submitted for publication includes material which has already been published elsewhere, it is the author's responsibility to obtain written permission to reproduce such material.

APPLIED COMPUTATIONAL ELECTROMAGNETICS SOCIETY JOURNAL

May 2011
Vol. 26 No. 5
ISSN 1054-4887

The ACES Journal is abstracted in INSPEC, in Engineering Index, DTIC, Science Citation Index Expanded, the Research Alert, and to Current Contents/Engineering, Computing & Technology.

The illustrations on the front cover have been obtained from the research groups at the Department of Electrical Engineering, The University of Mississippi.

MAY 2011 REVIEWERS

Ahmed Abdelrahman
Guido Ala
Shirook Ali
Rodolfo Araneo
Sami Barmada
Gerard Berginc
Ji Chen
Nicolas Cinosi
Jorge Costa
Said El-Khamy
Khaled ElMahgoub
Naftali Herscovici
Nathan Ida
Yasushi Kanai
Fadi Khalil
Slawomir Koziel
Mun Soo Lee
Ivor Morrow
Antonino Musolino
Rui Qiang
Luca Rienzo
Antonio Espirito Santo
Jerry Smith
Katherine Siakavara
Hossein Torkaman
Christopher Trueman
Shaoqiu Xiao

THE APPLIED COMPUTATIONAL ELECTROMAGNETICS SOCIETY

JOURNAL

Vol. 26 No. 5 May 2011

TABLE OF CONTENTS

Surface Integral Equation Method for Scattering by DB Objects with Sharp Wedges

Johannes Markkanen, Pasi Ylä-Oijala, and Ari Sihvola

Department of Radio Science and Engineering
Aalto University School of Electrical Engineering
PO Box 13000, FI-00076 AALTO, Finland
johannes.markkanen@aalto.fi, pasi.yla-oijala@aalto.fi, ari.sihvola@aalto.fi

Abstract – A surface integral equation method is used to analyze time-harmonic electromagnetic scattering by arbitrarily shaped three-dimensional DB objects with sharp wedges. At the DB boundary surface, the electric and magnetic flux densities $\boldsymbol{D}$ and $\boldsymbol{B}$ normal to the surface are zero. The DB boundary conditions are enforced by expanding the unknown equivalent surface current densities with divergence-free loop basis functions. The equations are tested with Galerkin's method. The integral equation method is applied to investige field behavior at sharp DB wedges and the results are compared with the quasistatic solution in order to determine the accuracy of numerical solution at the sharp DB wedges.

Index Terms – DB boundary condition, field singularity, integral equation method.

I. INTRODUCTION

In computational electromagnetics, boundary conditions are often used as approximations of real material interfaces. The perfect electric conductor (PEC) boundary condition, which requires the vanishing of the tangential component of the electric field at the boundary surface, is probably the most well-known and commonly used boundary condition. It is often used as an approximation of conducting surfaces, for example metallic surfaces at low frequencies. There are also other boundary conditions that can be useful in computional electromagnetics. Especially since they can be used for modelling exotic material interfaces, e.g. PEMC [1]. In [2] the use of such canonical surfaces in computational electromagnetics have been summarized.

Electromagnetic soft surfaces [3], on which the power does not propagate along the surface, have many micro- and millimeterwave engineering applications. For example, they can be used for reducing coupling between radiating elements in antenna arrays or creating rotational symmetric radiation patterns for horn antennas [4]. Anisotropic soft surfaces are generally fabricated by corrugated structures, which are quite difficult to model by using standard numerical softwares, because they contain a lot of fine details. A relatively easy way to approximate isotropic soft surfaces is to apply a DB boundary condition [5] in calculations.

The DB boundary condition requires that the normal components of the electric and magnetic flux densities vanish at the boundary. Analytical solutions for objects involving the DB boundaries have been studied in [5, 6, 7], and the integral-equation-method based numerical solution for the scattering by DB objects was introduced in [8]. However, in most practial cases, a discretization of geometry leads to sharp wedges and corners which can cause problems for numerical calculations. At these sharp wedges and corners, fields can be singular. This fact gives motivation to analyze behavior of fields near DB wedges. It is possible to solve field behavior near sharp wedges by using quasistatic analysis, because the geometry is independent of any scale parameter, and therefore, the incident field can be analyzed by using static approach. A quasistatic solution is a well-known result for PEC and dielectric wedges [9, 10]. In this paper, we use a similar approach for analyzing field behavior near the DB wedge. Also, we compare the quasistatic solution with the integral-equation-method based nu-

merical solution, and study the accuracy of the solution at the DB wedge.

II. DB BOUNDARY CONDITION

The DB boundary condition, introduced in [5], requires that the normal components of the electric and magnetic flux densities $\boldsymbol{D}, \boldsymbol{B}$ vanish on the surface:

$$\boldsymbol{n} \cdot \boldsymbol{D} = 0, \quad \boldsymbol{n} \cdot \boldsymbol{B} = 0. \tag{1}$$

In linear, homogeneous, and isotropic medium, where permittivity ϵ and permeability μ are constants, the DB boundary condition (1) can be expressed as

$$\boldsymbol{n} \cdot \boldsymbol{E} = 0, \quad \boldsymbol{n} \cdot \boldsymbol{H} = 0. \tag{2}$$

A look at the Poynting vector illuminates the character of a DB boundary. The average propagating power-density can be calculated from the real part of the complex Poynting vector

$$< S(t) >= \frac{1}{2} \Re\{\boldsymbol{E} \times \boldsymbol{H}^*\}, \tag{3}$$

where $\boldsymbol{H}^*$ denotes the complex conjugate of the magnetic field $\boldsymbol{H}$. At the DB boundary, the following can be written:

$$\boldsymbol{n} \times (\boldsymbol{E} \times \boldsymbol{H}^*) = \boldsymbol{E}(\boldsymbol{n} \cdot \boldsymbol{H})^* - (\boldsymbol{n} \cdot \boldsymbol{E})\boldsymbol{H}^* = 0. \tag{4}$$

Hence, the Poynting vector at the DB boundary has only the normal component and the tangential component vanishes. A soft surface has been defined [3] as a surface where the power flux along the boundary is zero. Therefore, the DB boundary is an isotropic soft surface.

III. INTEGRAL EQUATIONS FOR DB BOUNDARY

Consider an arbitrarily shaped three-dimensional object with the DB boundary condition in a homogeneous background medium and an incident time harmonic field ($e^{-i\omega t}$). The surface of the object is denoted by S and the electromagnetic parameters of the background medium are ε and μ. Our goal is to solve scattering of the electromagnetic waves by this obstacle. We begin with the following representation of the total time-harmonic electric and magnetic fields [11]

$$\begin{aligned} \Omega \boldsymbol{E} &= -\nabla \mathcal{S}(\boldsymbol{E}_n) + i\omega\mu \mathcal{S}(\boldsymbol{J}) - \mathcal{K}(\boldsymbol{M}) + \boldsymbol{E}^p \\ \Omega \boldsymbol{H} &= -\nabla \mathcal{S}(\boldsymbol{H}_n) + i\omega\varepsilon \mathcal{S}(\boldsymbol{M}) + \mathcal{K}(\boldsymbol{J}) + \boldsymbol{H}^p, \end{aligned} \tag{5}$$

where Ω is the relative solid angle subtended by the surface ($\Omega = 1/2$ on smooth surfaces), $\boldsymbol{E}_n$ and $\boldsymbol{H}_n$ are the normal components of the fields at the surface, $\boldsymbol{J} = \boldsymbol{n} \times \boldsymbol{H}$ and $\boldsymbol{M} = -\boldsymbol{n} \times \boldsymbol{E}$ are the equivalent electric and magnetic surface current densities, respectively, $\boldsymbol{E}^p$ and $\boldsymbol{H}^p$ are the primary fields, and $\boldsymbol{n}$ is the outer unit normal vector of the surface. The surface integral operators are defined as

$$\mathcal{K}(\boldsymbol{F})(\boldsymbol{r}) = \nabla \times \mathcal{S}(\boldsymbol{F})(\boldsymbol{r}), \tag{6}$$

$$\mathcal{S}(\boldsymbol{F})(\boldsymbol{r}) = \int_S G(\boldsymbol{r}, \boldsymbol{r}') \boldsymbol{F}(\boldsymbol{r}') \, \mathrm{d}S(\boldsymbol{r}), \tag{7}$$

where G is the free space Green's function

$$G(\boldsymbol{r}, \boldsymbol{r}') = \frac{e^{ik|\boldsymbol{r} - \boldsymbol{r}'|}}{4\pi|\boldsymbol{r} - \boldsymbol{r}'|}, \tag{8}$$

$\boldsymbol{r}$ is the observation point, $\boldsymbol{r}'$ is the source point, and $k = \omega\sqrt{\varepsilon\mu}$ is the wavenumber of the background. Let us define two surface integral operators as

$$\begin{aligned} \mathcal{F}_t &= -\boldsymbol{n} \times \boldsymbol{n} \times \mathcal{F} \\ \mathcal{F}_r &= \boldsymbol{n} \times \mathcal{F}. \end{aligned} \tag{9}$$

Due to the DB boundary conditions (2), $\boldsymbol{E}_n$ and $\boldsymbol{H}_n$ can be removed from (5). Normalizing the fields in the following way (to get better balance between the unknowns and the matrix elements, [12])

$$\tilde{\boldsymbol{E}} = \sqrt{\varepsilon}\boldsymbol{E}, \quad \tilde{\boldsymbol{H}} = \sqrt{\mu}\boldsymbol{H}, \tag{10}$$

so called T- equations is obtained by taking the tangential components

$$\begin{bmatrix} \tilde{\boldsymbol{H}}_t^p \\ \tilde{\boldsymbol{E}}_t^p \end{bmatrix} = \begin{bmatrix} -ik\mathcal{S}_t & -\frac{1}{2}\mathcal{I}_r - \mathcal{K}_t \\ \frac{1}{2}\mathcal{I}_r + \mathcal{K}_t & -ik\mathcal{S}_t \end{bmatrix} \begin{bmatrix} \tilde{\boldsymbol{M}} \\ \tilde{\boldsymbol{J}} \end{bmatrix}. \tag{11}$$

Another set of equations, called N- equations, is obtained by taking the cross product with the normal vector $\boldsymbol{n}$

$$\begin{bmatrix} -\tilde{\boldsymbol{E}}_r^p \\ \tilde{\boldsymbol{H}}_r^p \end{bmatrix} = \begin{bmatrix} \frac{1}{2}\mathcal{I}_t - \mathcal{K}_r & ik\mathcal{S}_r \\ -ik\mathcal{S}_r & \frac{1}{2}\mathcal{I}_t - \mathcal{K}_r \end{bmatrix} \begin{bmatrix} \tilde{\boldsymbol{M}} \\ \tilde{\boldsymbol{J}} \end{bmatrix}. \tag{12}$$

The integral equation formulations for DB objects contaning only T- or N- equations, however, suffer from internal resonances, i.e., the solution is not unique at certain frequencies. Internal resonances can be eliminated by combining equations (11) and (12) in

a similar fashion as the T- and N- equations are combined in [13] in the case of penetrable objects. This gives the following combined field integral equation (CFIE) formulation for DB objects

$$\begin{bmatrix} -\tilde{\boldsymbol{F}}_r \\ \tilde{\boldsymbol{F}}_t \end{bmatrix} = \begin{bmatrix} \mathcal{N}_t & -\mathcal{N}_r \\ \mathcal{N}_r & \mathcal{N}_t \end{bmatrix} \begin{bmatrix} \tilde{\boldsymbol{M}} \\ \tilde{\boldsymbol{J}} \end{bmatrix}, \tag{13}$$

with

$$\mathcal{N}_t = \frac{1}{2}\mathcal{I}_t - \mathcal{K}_r - ik\mathcal{S}_t \text{ and } \tilde{\boldsymbol{F}}_t = \tilde{\boldsymbol{H}}_r^p + \tilde{\boldsymbol{E}}_t^p. \tag{14}$$

IV. NUMERICAL SOLUTION TO THE INTEGRAL EQUATIONS

Integral equations (11–13) are solved numerically with the method of moments [14]. First, the unknown equivalent electric $\boldsymbol{J}$ and magnetic $\boldsymbol{M}$ surface current densities are represented as linear combinations of known tangential vector basis functions $\boldsymbol{f}$ and $\boldsymbol{g}$

$$\begin{aligned} \boldsymbol{J} &\approx \sum_{k=1}^{N} j_k \boldsymbol{f}_k \\ \boldsymbol{M} &\approx \sum_{l=1}^{M} m_l \boldsymbol{g}_l, \end{aligned} \tag{15}$$

where j_k and m_l are scalar coefficients. By using Maxwell's equations and certain vector identities, we can find a relation between the normal components of the fields and the divergences of the equivalent surface currents

$$\begin{aligned} \nabla_s \cdot \boldsymbol{J} &= i\omega\varepsilon \boldsymbol{n} \cdot \boldsymbol{E} \\ \nabla_s \cdot \boldsymbol{M} &= i\omega\mu \boldsymbol{n} \cdot \boldsymbol{H}. \end{aligned} \tag{16}$$

As we can see, on the surface of a DB object the surface divergences of the currents vanish (if $\omega \neq 0$) due to the DB boundary conditions (2). Therefore, we have to expand both the electric and magnetic equivalent surface current with a set of basis functions which span a solenoidal vector space. We have used the RWG loop basis functions [15] to expand the equivalent currents, and the equations are tested with Galerkin's scheme using the RWG loop functions as testing functions.

A numerical solution requires calculation of singular integrals because the Green's function becomes singular when the distance between the source point and the observation point goes to zero. These integrals are evaluated by using the singular subtraction technique [16].

V. FIELD BEHAVIOR AT A DB WEDGE

Singularities of the fields appear near sharp wedges and corners with a proper incident field, and these singularities can cause problems for the numerical solution. For example, in case of a PEC or dielectric wedge the fields are singular, and hence, we need to use mesh refinement near the wedges and corners in order to obtain an accurate solution. In this section, we study singularities of fields in the case of a DB wedge.

Consider a three-dimensional sharp wedge with a DB boundary condition. Since the wedge is sharp, we can use quasistatic approximation. Therefore, the electric field $\boldsymbol{E}$ near the wedge can be expressed in terms of the electrostatic potential $\boldsymbol{E} = -\nabla\phi$. In the static and source-current free case we can also express the magnetic field in terms of a scalar potential $\boldsymbol{H} = -\nabla\phi_m$, but here we only consider the electric field because the analysis is identical in both cases.

We know that the potential function outside the wedge must satisfy the Laplace's equation

$$\nabla^2\phi = 0, \tag{17}$$

because the divergence of the electric field must be zero in a source free region. Also, the field must satisfy the boundary condition at the surface. We can approximate this problem with the two-dimensional infinite wedge, see Fig. 1.

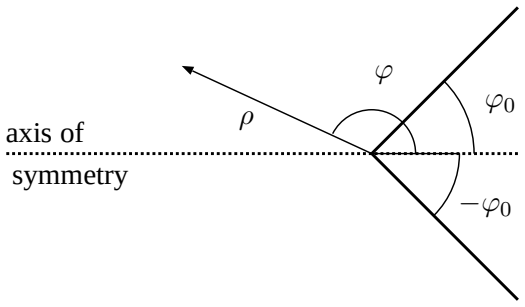

Fig. 1. Two-dimensional infinite wedge. Surface of the wedge is at $\varphi = \varphi_0$ and $\varphi = -\varphi_0$.

In the polar coordinate system the Laplace's equation (17) can be expressed as

$$\nabla^2\phi(\rho,\varphi) = \frac{1}{\rho}\frac{\partial}{\partial\rho}\left(\rho\frac{\partial\phi(\rho,\varphi)}{\partial\rho}\right) + \frac{1}{\rho^2}\frac{\partial^2\phi(\rho,\varphi)}{\partial\varphi^2} = 0, \tag{18}$$

where ρ is the radial coordinate and φ is the angular coordinate. This equation can be solved by the separation of variables

$$\phi(\rho,\varphi)=\sum_n P_n(\rho)\Phi_n(\varphi), \tag{19}$$

which leads to two separate differential equations

$$\frac{\partial^2\Phi_n(\varphi)}{\partial\varphi^2}+\nu_n^2\Phi_n(\varphi)=0 \tag{20}$$

$$\rho\frac{\partial}{\partial\rho}\left(\rho\frac{P_n(\rho)}{\partial\rho}\right)-\nu_n^2P_n(\rho)=0. \tag{21}$$

General solutions for the equations (20) and (21) are

$$\begin{aligned}\Phi_n(\varphi)&=A_n\sin(\nu_n\varphi)+B_n\cos(\nu_n\varphi)\\ P_n(\rho)&=C_n\rho^{\nu_n}+D_n\rho^{-\nu_n},\end{aligned} \tag{22}$$

where A_n, B_n, C_n, and D_n are the unknown coefficients. The coefficient D_n must be zero, because a negative exponent $\rho^{-\nu_n}$ leads to an infinite energy at the origin.

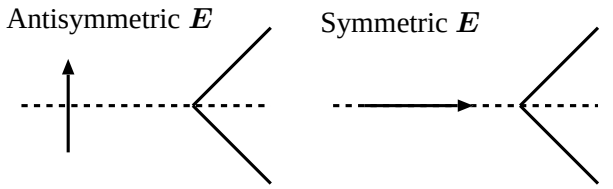

Fig. 2. Antisymmetric and symmetric excitations with respect to the wedge.

If the incident field is symmetric with respect to the plane of symmetry $\varphi=0$ (see Fig. 2), the potential function can be expressed as

$$\phi(\rho,\varphi)=\sum_n B_n\rho^{\nu_n}\cos(\nu_n(\pi-\varphi)), \tag{23}$$

if $\varphi_0\le\varphi\le 2\pi-\varphi_0$. By taking the gradient of the potential function, we obtain the electric field

$$\begin{aligned}\boldsymbol{E}(\rho,\varphi)&=-\nabla\phi(\rho,\varphi)\\ &=-\boldsymbol{u}_\rho\sum_n B_n\rho^{\nu_n-1}\nu_n\cos(\nu_n(\pi-\varphi))\\ &\quad-\boldsymbol{u}_\varphi\sum_n B_n\rho^{\nu_n-1}\nu_n\sin(\nu_n(\pi-\varphi)).\end{aligned} \tag{24}$$

By using the DB boundary condition $\boldsymbol{u}_\varphi\cdot\boldsymbol{E}=0$ at $\varphi=\varphi_0$, we find that

$$\sum_n B_n\rho^{\nu_n-1}\nu_n\sin(\nu_n(\pi-\varphi_0))=0, \tag{25}$$

which is satisfied if

$$\nu_n=\frac{\pi}{\pi-\varphi_0}n,\quad n=1,2,... \tag{26}$$

Next, we consider the antisymmetric case where the incident field is normal to the plane of symmetry ($\varphi=0$). Now the potential function is

$$\phi(\rho,\varphi)=\sum_n A_n\rho^{\nu_n}\nu_n\sin(\nu_n(\pi-\varphi)), \tag{27}$$

if $\varphi_0\le\varphi\le 2\pi-\varphi_0$, and the electric field can be expressed as

$$\begin{aligned}\boldsymbol{E}(\rho,\varphi)&=-\nabla\phi(\rho,\varphi)\\ &=-\boldsymbol{u}_\rho\sum_n A_n\rho^{\nu_n-1}\nu_n\sin(\nu_n(\pi-\varphi))\\ &\quad+\boldsymbol{u}_\varphi\sum_n A_n\rho^{\nu_n-1}\nu_n\cos(\nu_n(\pi-\varphi)).\end{aligned} \tag{28}$$

In the case of the DB boundary condition

$$\sum_n A_n\rho^{\nu_n-1}\nu_n\cos(\nu_n(\pi-\varphi_0))=0, \tag{29}$$

which is satified if

$$\nu_n=\frac{\pi}{2(\pi-\varphi_0)}n,\quad n=1,3,5,... \tag{30}$$

Parameter ν_n defines the order of singularity of field, since the field strength is related to a term ρ^{ν_n-1}. It is easy to see that the field has a singularity if the smallest value of the parameter $\nu_n<1$. Figure 3 shows the value of the parameter ν_1 as a function of angle φ_0. We can see that the DB wedge has a singularity if the excitation field is antisymmetric, and the angle $\varphi_0<90$ degrees.

It is important to note that a solution in the case of an arbitrarily polarized field can be found as a linear combination of symmetric and antisymmetric excitations. This analysis is valid also if $\boldsymbol{E}$ is replaced by $\boldsymbol{H}$ because of the symmetry of the DB boundary condition.

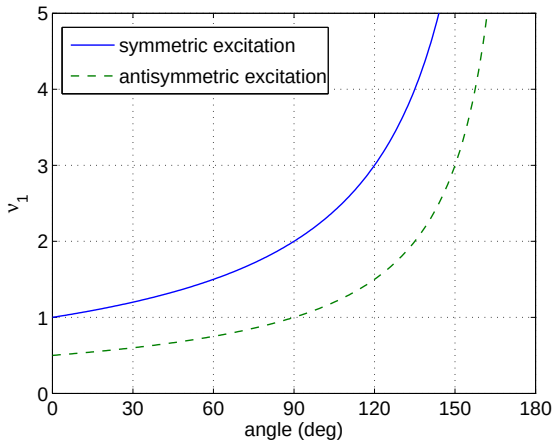

Fig. 3. Parameter ν_1 as a function of angle φ_0 with either symmetric or antisymmetric excitations. The field is singular if the parameter $\nu_1 < 1$.

VI. NUMERICAL RESULTS

Let us first investigate the behavior of the equivalent surface currents near a 90° wedge, which is characterized by either DB or PEC boundary conditions. We can solve the problem for the DB boundary in the static case by using equations (26) and (30) and requiring $\varphi_0 = \pi/4$. In Table 1, we see singularity factors ($\rho^{\nu_n - 1}$) in case of 90° DB and PEC wedges with symmetric and antisymmetric excitations. The PEC case can be solved in a similar way as the DB case, but we have to apply the PEC boundary conditions $\boldsymbol{u}_\rho \cdot \boldsymbol{E} = 0$ and $\boldsymbol{u}_\varphi \cdot \boldsymbol{H} = 0$.

Table 1: Singularities of 90° DB and PEC wedges

Excitation	Field	DB	PEC
Symmetric $\boldsymbol{E}^i$	$\boldsymbol{E} \cdot \boldsymbol{u}_\rho$	$\rho^{\frac{1}{3}}$	0
Symmetric $\boldsymbol{H}^i$	$\boldsymbol{H} \cdot \boldsymbol{u}_\rho$	$\rho^{\frac{1}{3}}$	$\rho^{\frac{1}{3}}$
Symmetric $\boldsymbol{E}^i$	$\boldsymbol{E} \cdot \boldsymbol{u}_\varphi$	0	$\rho^{-\frac{1}{3}}$
Symmetric $\boldsymbol{H}^i$	$\boldsymbol{H} \cdot \boldsymbol{u}_\varphi$	0	0
Antisymmetric $\boldsymbol{E}^i$	$\boldsymbol{E} \cdot \boldsymbol{u}_\rho$	$\rho^{-\frac{1}{3}}$	0
Antisymmetric $\boldsymbol{H}^i$	$\boldsymbol{H} \cdot \boldsymbol{u}_\rho$	$\rho^{-\frac{1}{3}}$	$\rho^{-\frac{1}{3}}$
Antisymmetric $\boldsymbol{E}^i$	$\boldsymbol{E} \cdot \boldsymbol{u}_\varphi$	0	$\rho^{\frac{1}{3}}$
Antisymmetric $\boldsymbol{H}^i$	$\boldsymbol{H} \cdot \boldsymbol{u}_\varphi$	0	0

We can see that the tangential components of both fields are singular in the case of the DB wedge with antisymmetric excitation, but with symmetric excitation fields are not singular. Also, we can see that the normal components of fields vanish at the wedge due to the DB boundary condition. In case of the PEC wedge, the tangential electric field and the normal component of the magnetic field are zero. With the symmetric electric field incident, the normal component of the electric field is singular but the tangential component is non-singular. Also, the antisymmetric magnetic field incident creates a singularity to the tangential component of the magnetic field at the wedge.

Now, we know how fields behave near DB wedges, and we can study the accuracy of the surface-integral-equation-method based solution near DB wedges. Consider a small cube with DB boundary condition. This cube with edge length a is illuminated by a linearly polarized planewave with wavelength $\lambda = 10\,a$. We can choose the alignment of the cube so that the behavior of fields at the wedge corresponds to the 2-D case with either symmetric or antisymmetric excitations.

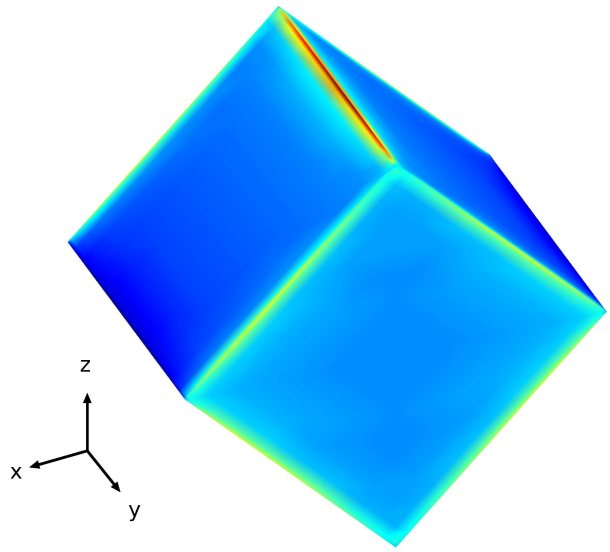

Fig. 4. Real part of the equivalent electric surface current density at the surface of DB cube. The cube is illuminated by a planewave which is propagating along z-axis and the electric field is polarized along y-axis and the magnetic field along x-axis. The equivalent current $\boldsymbol{J}$ has a singularity at the top edge, because the incident magnetic field is antisymmetric with respect to the wedge on top.

Figure 4 shows the real part of the equivalent electric surface current density $\boldsymbol{J}$ on the surface of the DB cube. We can see that the equivalent electric surface current ($\boldsymbol{J} = \boldsymbol{n} \times \boldsymbol{H}$) is singular at the wedge on top, because in this case we have an antisymmetric incident magnetic field with respect to the wedge on top.

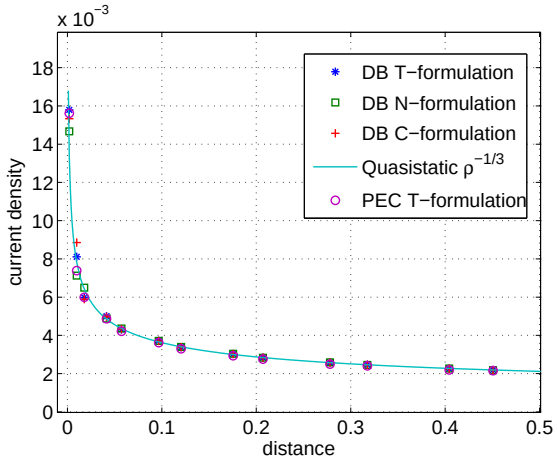

Fig. 5. Amplitude of the equivalent electric surface current density as a function of distance from the sharp 90 degree DB and PEC wedges. Solutions are obtained by using different formulations of surface integral equation method and quasistatic analysis.

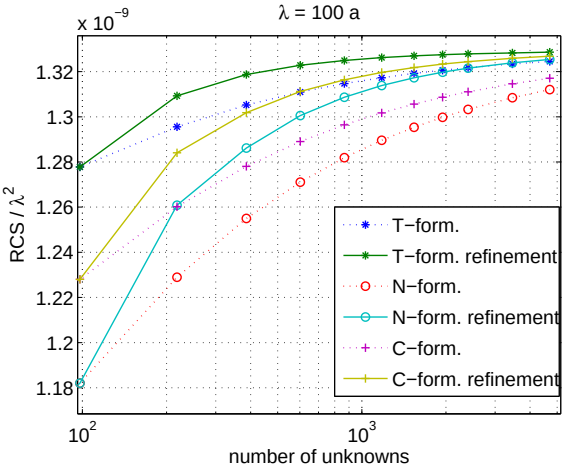

Fig. 6. Calculated backscattered radar cross section of a cube with edge length a and wavelength $\lambda = 100\,a$ as a function of number of unknowns. T-, N- and C- formulations have been applied. The cube is discretized by using triangular meshes with or without mesh refinement on the edges. Solid lines correspond to the cases with mesh refinements and dotted lines without mesh refinements.

In Figure 5, the amplitude of the equivalent electric surface current density is shown as a function of distance from the wedge. The calculations are done by using T-, N-, and C- formulations and the results are compared with the quasistatic solution.

As can be seen, all three formulations give almost identical results for the equivalent current densities near 90° DB wedge, and the numerical results have a good agreement with the quasistatic solution. However, there are some variations in the amplitude of currents between formulations especially if the distance to the sharp wedge is short. Figure 5 also shows the behavior of the equivalent surface current at the PEC wedge. The PEC case is calculated by using the conventional tangential electric field integral equation (EFIE) formulation with RWG basis and testing functions [17].

As the quasistatic analysis predicts, at the DB and PEC wedge tangential fields have the same order of singularity and the numerical results agree with it. It is important to note that the normal component of the electric field is singular in case of the PEC wedge, if the incident electric field is symmetric with respect to the wedge. We know that there is a relation between the normal component of field and the divergence of the equivalent surface current (16), but this singularity does not affect the result in Figure 5 because the incident electric field is not symmetric at the wedge.

Let us next study the convergence of the numerical solution in case of a DB cube. The setup is the same as in Figure 4. In Figure 6, the backscattered radar cross section (RCS) as a function of the number of unknowns is shown. The edge length of the cube is a and the wavelength is $\lambda = 100\,a$. In Figure 7 we can see the convergence of RCS with wavelength $\lambda = 2\,a$. We have used T-, N-, and C-formulations for calculations, and the surface of the cube is discretized by triangular mesh with mesh refinement on the edges, or without mesh refinement on the edges.

In this example wavelengths are 100 and 2 times the edge length of the cube, and hence, both frequencies are not at internal resonant frequencies. This means that the solutions of T-, N-, and C- formulations are unique. We can see that the T- formulation gives the most accurate results for backscatted RCS. The convergence of N- formulation is quite slow. The accuracy of C- formulation is between T- and N- formulations which makes sense because C- formulation is a combination of T- and N- formulations. This agrees with the earlier results in the PEC case [18] where T-formulation agrees with EFIE, N-formulation with MFIE, and C-formulation with CFIE, respectively. Figures 6 and 7 also show that the solutions converge faster if mesh refinements on wedges are used.

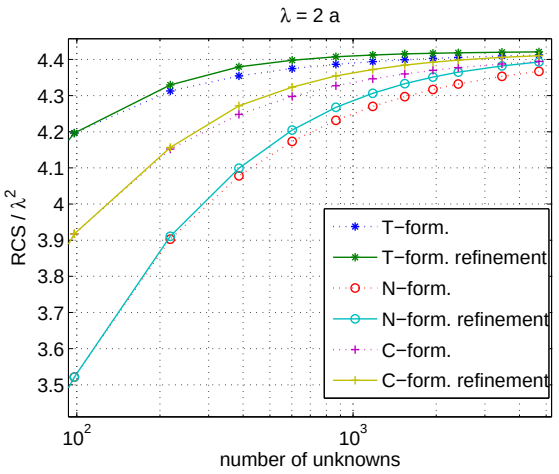

Fig. 7. Calculated backscattered radar cross section of a DB cube with wavelength $\lambda = 2\,a$. Otherwise the setup is the same as in Figure 6.

VII. CONCLUSIONS

In this paper, the accuracy of a surface-integral-equation based solution for DB objects has been studied. A quasistatic solution for the field near DB wedges has been derived and the results have been compared with numerical calculations. The numerical examples demonstrate that the surface-integral-equation-method based solution is quite accurate near DB wedges even if the field is singular at the wedge. We have also showed that the tangential magnetic field at the PEC wedge has the same order of singularity as that of the DB wedge. The normal component of the electric field can be singular at the PEC wedge, but there is not such singularity at the DB wedge, because normal components of fields vanish at the DB boundary. However, the effect of this singularity to the equivalent surface current in the case of the PEC wedge is much weaker than the effect of the singularity in the tangential field. Therefore, we need to use similar mesh refinements at the DB wedges as the PEC wedges in order to obtain an accurate solution.

ACKNOWLEDGMENT

This study was supported by the Academy of Finland projects 125979 and 124204.

REFERENCES

[1] A. Sihvola, P. Ylä-Oijala, and I. Lindell, "Scattering by PEMC (Perfect Electromagnetic Conductor) Spheres using Surface Integral Equation Approach," *ACES Journal*, vol. 22, no. 2, pp. 236–249, 2007.

[2] P. R. Kildal, A. Kishk, and Z. Sipus, "Introduction to Canonical Surfaces in Electromagnetic Computations: PEC, PMC, PEC/PMC Strip Grid, DB Surface," *26th Annual Review of Progress in Applied Computational Electromagnetics, Tampere, Finland, 2010*, pp. 514–519.

[3] P.-S. Kildal, "Definition of Artificially Soft and Hard Surfaces for Electromagnetic Waves," *Electronics Letters*, vol. 24, pp. 168–170, Feb. 1988.

[4] P.-S. Kildal, "Artificially Soft and Hard Surfaces in Electromagnetics," *IEEE Trans. Antennas and Propagation*, vol. 38, pp. 1537 –1544, Oct. 1990.

[5] I. V. Lindell and A. H. Sihvola, "Electromagnetic Boundary and Its Realization with Anisotropic Metamaterial," *Physical Review E (Statistical, Nonlinear, and Soft Matter Physics)*, vol. 79, no. 2, p. 026604, 2009.

[6] I. V. Lindell and A. H. Sihvola, "Spherical Resonator with DB-Boundary Conditions," *Progress In Electromagnetics Research Letters*, vol. 6, pp. 131–137, 2009.

[7] A. Sihvola, H. Wallén, P. Ylä-Oijala, M. Taskinen, H. Kettunen, and I. V. Lindell, "Scattering by DB Spheres," *Antennas and Wireless Propagation Letters, IEEE*, vol. 8, pp. 542–545, 2009.

[8] J. Markkanen, P. Ylä-Oijala, and A. Sihvola, "Computation of Scattering by DB Objects with Surface Integral Equation Method," *IEEE Trans. Antennas and Propagation*, vol. 59, pp. 154 –161, Jan. 2011.

[9] J. G. Van Bladel, *Electromagnetic Fields*. Wiley Interscience, 2nd ed., 2007.

[10] J. D. Jackson, *Classical Electrodynamics*. John Wiley & Sons, 3rd ed., 1998.

[11] J. A. Stratton, *Electromagnetic Theory*. McGraw-Hill Company, New York, London, 1941.

[12] M. Taskinen and P. Ylä-Oijala, "Current and Charge Integral Equation Formulation," *IEEE Trans. Antennas and Propagation*, vol. 54, pp. 58–67, Jan. 2006.

[13] P. Ylä-Oijala and M. Taskinen, "Application of Combined Field Integral Equation for Electromagnetic Scattering by Dielectric and Composite Objects," *IEEE Trans. Antennas and Propagation*, vol. 53, pp. 1168 – 1173, Mar. 2005.

[14] R. F. Harrington, *Field Computation by Moment Methods*. IEEE press, New York, 1993.

[15] G. Vecchi, "Loop-Star Decomposition of Basis Functions in the Discretization of the EFIE," *IEEE Trans. Antennas and Propagation*, vol. 47, pp. 339 –346, Feb. 1999.

[16] S. Järvenpää, M. Taskinen, and P. Ylä-Oijala, "Singularity Subtraction Technique for High-Order Polynomial Vector Basis Functions on Planar Triangles," *IEEE Trans. Antennas and Propagation*, vol. 54, pp. 42 – 49, Jan. 2006.

[17] S. Rao, D. Wilton, and A. Glisson, "Electromagnetic Scattering by Surfaces of Arbitrary Shape," *IEEE*

Trans. Antennas and Propagation, vol. 30, pp. 409–418, May 1982.

[18] P. Ylä-Oijala, M. Taskinen, and S. Järvenpää, "Analysis of Surface Integral Equations in Electromagnetic Scattering and Radiation Problems," *Engineering Analysis with Boundary Elements*, vol. 32, pp. 196–209, 2008.

Johannes Markkanen was born in Kerava, Finland, in 1984. He received the M.Sc. (Tech.) degree in Electrical Engineering from the Helsinki University of Technology (TKK), Espoo, Finland, in 2009. Currently, he is working toward the D.Sc. (Tech.) degree in the Aalto University, School of Electrical Engineering, Department of Radio Science and Engineering, Finland. His research interests include integral equation methods in computational electromagnetics.

Pasi Ylä-Oijala received the M.Sc. and Ph.D. degrees in Applied Mathematics from the University of Helsinki, Helsinki, Finland, in 1992 and 1999, respectively. Currently, he is working as a senior researcher with the Aalto University, School of Electrical Engineering, Department of Radio Science and Engineering, Finland. His field of interest focuses on the development of efficient and stable integral equation based formulations and algorithms in computational electromagnetics, and analysis of electromagnetic phenomena.

Ari Sihvola was born in 1957 in Valkeala, Finland. He received the degrees of Diploma Engineer in 1981, Licentiate of Technology in 1984, and Doctor of Technology in 1987, all in Electrical Engineering, from the Helsinki University of Technology (TKK), Finland. Besides working for TKK and the Academy of Finland, he was visiting engineer in the Research Laboratory of Electronics of the Massachusetts Institute of Technology, Cambridge, in 1985-1986, and in 1990-1991, he worked as a visiting scientist at the Pennsylvania State University, State College. In 1996, he was visiting scientist at the Lund University, Sweden, and for the academic year 2000-01, he was visiting professor at the Electromagnetics and Acoustics Laboratory of the Swiss Federal Institute of Technology, Lausanne. In the Summer of 2008, he was visiting professor at the University of Paris XI, France. Ari Sihvola is professor of electromagnetics in Aalto University School of Electrical Engineering (former name before 2010: Helsinki University of Technology) with interest in electromagnetic theory, complex media, materials modelling, remote sensing, and radar applications. He is Chairman of the Finnish National Committee of URSI (International Union of Radio Science), official member for Finland of URSI Commission B (Fields and Waves), and Fellow of IEEE. He was awarded the five-year Finnish Academy Professor position starting August 2005. He is also director of the Finnish Graduate School of Electronics, Telecommunications, and Automation (GETA).

Design of a Compact Circular Waveguide Antenna of Low Polarization Level using EBG Structures

Josefa Gómez, Abdelhamid Tayebi, Iván González, and Felipe Cátedra

Computer Sciences Department
University of Alcalá, 28871 Alcalá de Henares (Madrid), Spain
josefa.gomezp@uah.es, hamid.tayebi@uah.es, ivan.gonzalez@uah.es, felipe.catedra@uah.es

Abstract ─ A new technique to improve the performance, in terms of bandwidth, gain and polarization purity, of conventional circular waveguide antennas using an electromagnetic band gap (EBG) structure is presented. The proposed antenna is composed by a circular waveguide and two layers with squared holes located over the waveguide aperture. The dimensions of the antenna have been obtained by means of an optimization process that uses a rigorous analysis tool. According to the results, a notable enhancement in polarization purity and gain is demonstrated when incorporating the second grid. The EBG antenna has the peak gain 14.36 dBi and the cross polarization level is lower than 40 dB within a wide bandwidth of 17%. A prototype has been fabricated and measured operating at 9.1GHz.

Index Terms ─ Antenna measurements, antenna radiation patterns, method of moments (MoM), waveguide antennas.

I. INTRODUCTION

It is well known that electromagnetic band gap (EBG) materials are designed to impede the propagation of electromagnetic waves at certain frequency bands that are determined by the periodicities of the materials and their dielectric constants. Recently, various applications of EBG materials, such as microwave filters, antennas, amplifiers, microstrip devices, ground plane structures, and base station antennas have been reported in the literature [1-4]. For example, EBG material has been shown to enhance the directivity of a patch antenna from 8 dB to 20 dB [1]. Palikaras *et al.* [2] described a method to design directive antennas by incorporating cylindrical EBG structures. On the other hand, [3] presents a resonator antenna that increases its gain and bandwidth with an EBG structure over the device. It has also been demonstrated [4] that the EBG materials are able to provide good results while reducing the size of some kind of filters.

The work presented in [5] summarizes the benefits of using EBG materials to improve the performance of microwave and optical applications. Some experimental results are discussed to check the properties of these materials.

According to [6], an increase in directivity can be obtained by adding a partially reflecting sheet in front of the antenna because of the multiple reflections between the sheet and the screen. The resonance distance between both elements must be such that the rays projected through the sheet have equal phases in the normal direction. Our contribution is focused on that investigation line. However, a deeper study is done here: we analyze the inclusion of a second grid over the antenna aperture and its influence over the cross polarization level. Numerical results demonstrate an improvement in gain, bandwidth and polarization purity when comparing several antenna configurations varying the distances between both grids.

The aim of this paper is to design a compact EBG antenna that provides a gain greater than 14.0 dBi, polarization purity greater than 40 dB, and a bandwidth greater than 10% while

maintaining a very small size. To fulfill these requirements, the dimensions of the antenna were optimized by using a powerful electromagnetic solver. After obtaining the optimum dimensions, a prototype made of aluminum was built and measured.

II. GEOMETRICAL MODEL

The proposed antenna configuration is depicted in Fig. 1 where the dimensions are in meters. The antenna model is defined by a long metallic cylinder with a 13.9 mm radius, a short metallic cylinder with a 16.9 mm radius, and 12.5 mm length, an 80 x 80 mm ground plane and the EBG structure (also 80 x 80 mm). According to Fig. 1.b, an electric dipole located at λ/4 from the bottom of the circular waveguide has been used to model the feeding of the waveguide in the simulations. The dipole is oriented in the *x* axis parallel to the bottom of the waveguide.

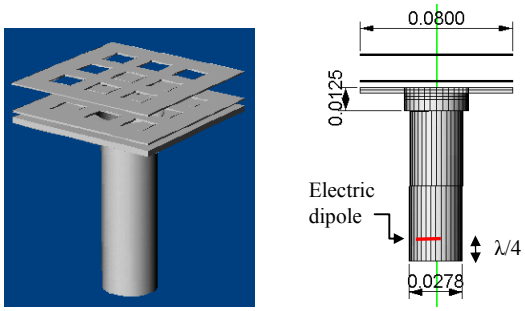

Fig. 1. Schematic representation of the proposed antenna, 3-D (left) and side view (right).

Each grid is composed of a metallic sheet with nine square holes. Figure 2 shows the dimensions (in meters).

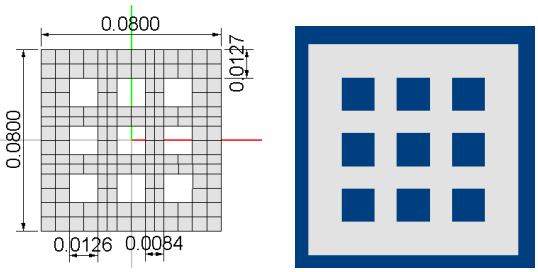

Fig. 2. Physical dimensions (in meters) of the EBG structure.

The distance between the ground plane and the first metallic grid was established to prevent cavity resonances at the operating frequency whereas the distance between the two metallic grids was set to obtain the classical EBG mode that permits an efficient antenna performance.

A parametric analysis was conducted to find the dimensions shown in Fig. 2. The first step in the design process was choosing the unit cell shape of the periodic structure. Some candidates were studied, such as rectangles, triangles, circles, rhombs, and crosses. After an exhaustive study, the square hole was chosen because of its simplicity and its good response. The next point was the optimization of the structure dimensions a central frequency of 9.1 GHz. Several geometrical parameters (the distance between adjacent holes, the size of the holes, the number of holes, etc.) were optimized. After the analysis of the position of the periodic structures, we conclude that the upper grid must be located 17.5 mm from the ground plane and the lower grid must be situated 3.5 mm from the ground plane. Those are the optimum physical dimensions to achieve the desirable radiation characteristics of high gain and low cross polarization level. The remaining geometrical parameters related to the waveguide were fixed.

The design was implemented using Monurbs [7], a versatile electromagnetic solver based on the moment method that uses parametric surfaces for representing the geometrical model and the current of the structures under analysis. Monurbs has been validated with real measurements in many applications. The optimization process was carried out using a new module of the tool that allows us to set the requirements and the geometrical parameters to vary. The simulation process finishes when the optimization module finds the optimum parameter values that provide the desired radiation pattern. As mentioned before, in this case the cost function was defined to obtain high polarization purity and high gain over a wide bandwidth. The values of the geometrical parameters must be assigned within a certain range defined by the user. The minimum and maximum values for the size of the squared holes were 8mm and 14mm, respectively. Regarding the resonance distances between the grids, the height of the lower grid from the ground plane was optimized within the range from 3mm to 7.5mm and the

height of the upper grid from the ground plane was optimized within the range from 9 and 18mm.

III. RESULTS

To validate the simulation results, a prototype of the designed EBG antenna was built based on the optimized antenna geometry. The prototype was measured in an anechoic chamber. Figure 3 depicts a photograph of the built antenna.

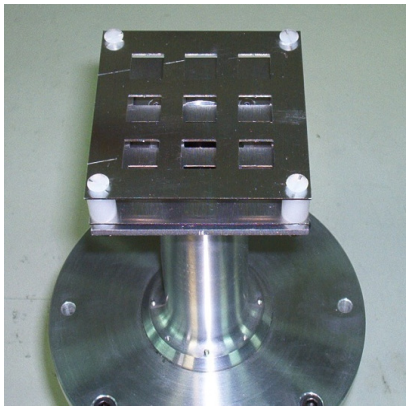

Fig. 3. Prototype of the EBG antenna.

The antenna was made of aluminum and weighed nearly 400 g. The pair of metallic grids was kept fixed by four plastic screws. The screws crossed the ground plane and kept the three different parts together. The antenna was fed to radiate linear polarization.

Figures 4 through 7 show comparisons between the measurements and the simulated values for the three main radiation cuts at 9.1 GHz.

The proposed antenna provides the maximum radiation in the axial direction. Good agreement between real measurements and computations was shown. The slight discrepancies between measurements and simulation values may be due to unwanted effects as well as non-idealities introduced by the four screws and the manufacturing errors. Also, the cross polarization level in the E and H plane cuts is below -40dB.

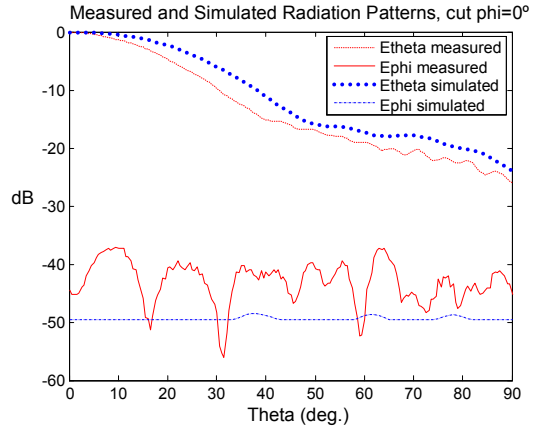

Fig. 4. Comparison of the simulated and measured radiation patterns. E-plane cut at 9.1GHz.

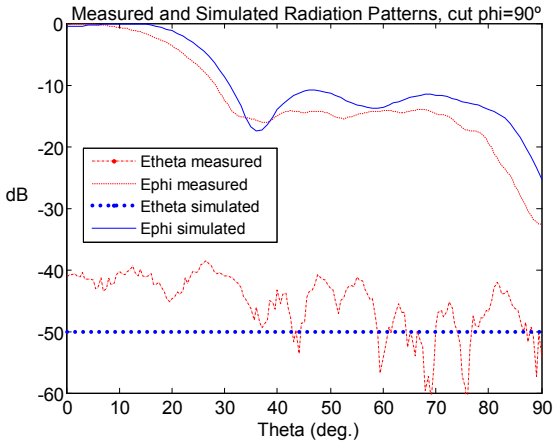

Fig. 5. Comparison of the simulated and measured radiation patterns. H-plane cut at 9.1 GHz.

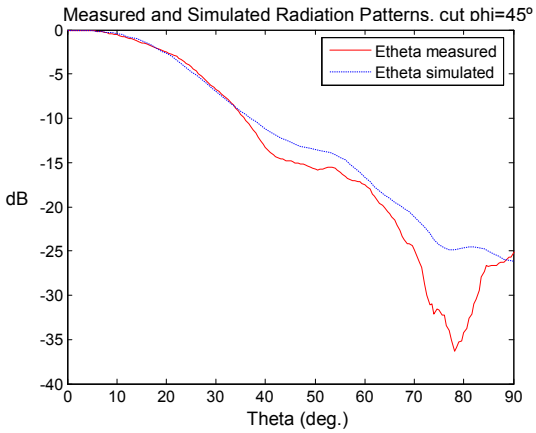

Fig. 6. Comparison of the simulated and measured radiation patterns. Diagonal-plane cut at 9.1GHz. Etheta component.

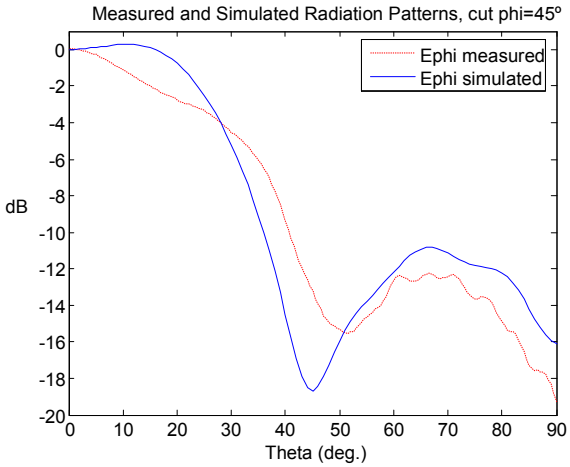

Fig. 7. Comparison of the simulated and measured radiation patterns. Diagonal-plane cut at 9.1GHz. Ephi component.

To verify the behavior of the EBG structure, several simulations were made to compare the results when the height of the cases were studied fixing the upper grid position at 17.5mm and changing the lower grid position at h1=4.3mm, h2=5.1mm, h3=5.9mm, h4=6.7mm, and h5=7.5mm. A decrease in gain was proven when the height of the lower grid increases, that is to say, when both grids are closer. This comparison ensures that the effect of including the second EBG structure is an enhancement in the gain lower grid changes or when there is only one grid.

The gain variation versus frequency is plotted in Fig. 8. Notice that a significant enhancement in gain is produced when including the second grid. It can be observed that the peak gain is located at 8 GHz when there is only one grid situated at 17.5mm from the ground plane. The maximum gain for the best configuration with two grids is 14.36 dBi at 9.0 GHz and the enhanced bandwidth (where gain did not decrease more than 3 dB below the maximum value) extends from 8.2 to 9.7 GHz, which means about a bandwidth of 17%.

On the other hand, a second comparison is shown in Figs. 9-10 to analyze the effect of moving the lower. Five different cases were studied fixing the upper grid position at 17.5mm and changing the lower grid position at h1=4.3mm, h2=5.1mm, h3=5.9mm, h4=6.7mm, and h5=7.5mm. A decrease in gain was proven when the height of the lower grid increases, that is to say, when both grids are closer.

This comparison ensures that the effect of including the second EBG structure is an enhancement in the gain at the central frequency.

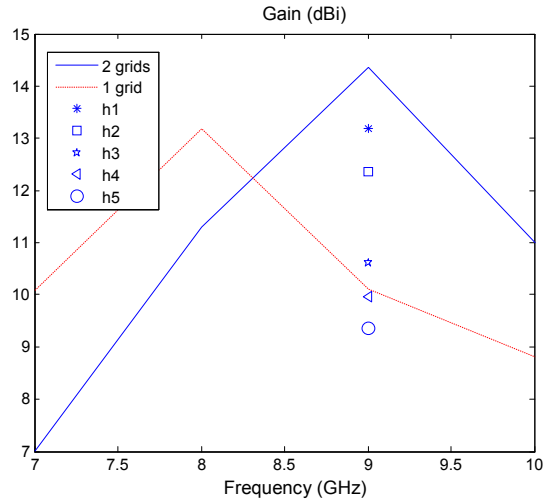

Fig. 8. Gain versus frequency. Comparison between results obtained considering only one grid (red line) and two grids located at optimum distances (blue line). The gain for several values of the height of the lower grid for the case of two grids is also shown for a frequency of 9.0 GHz.

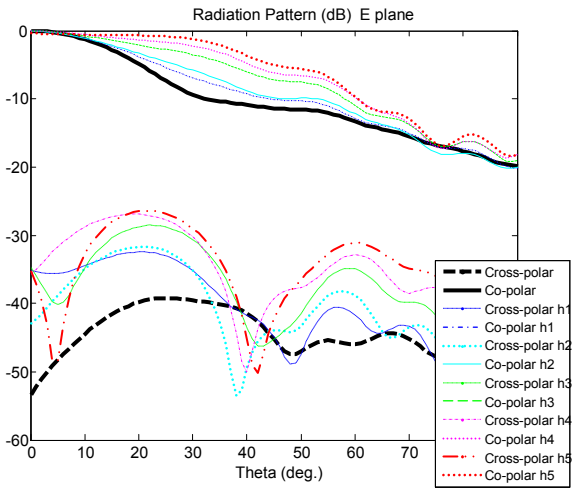

Fig. 9. Comparison between the simulated E-plane cuts at 9.0 GHz for several values of the height of the lower grid. The results for the optimum configuration are depicted in thick lines.

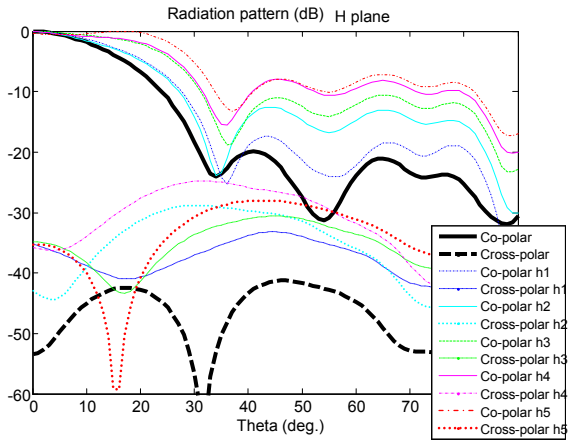

Fig. 10. Comparison between the simulated H-plane cuts at 9.0 GHz for several values of the height of the lower grid. The results for the optimum configuration are depicted in thick lines.

Table 1 summarizes the results of gain and cross polarization level at 9.0 GHz considering several EBG structures. The best configuration is obtained when the second grid is located at 3.5mm from the ground plane. The gain for that case is 14.36dBi and the cross polarization level is 53.38dB. It is worth to highlight that the other configurations provide worse results.

Figs. 9 and 10 present the radiation patterns obtained for the six situations. The optimum configuration is shown in black color. The benefit of including the two EBG structures over the polarization purity can be observed in both E and H plane cuts.

Table 1: Gain and cross polarization level comparison when varying the height of the lower grid at 9GHz

Height of upper grid	**Height of lower grid**	**Gain (dBi)**	**CP-XP (dB) θ=0º, φ=0º**
17.5mm	3.5mm	14.36	53.38
17.5mm	h1 = 4 .3mm	13.19	35.12
17.5mm	h2 = 5.1mm	12.35	42.94
17.5mm	h3 = 5.9mm	10.61	34.8
17.5mm	h4 = 6.7mm	9.96	35.81
17.5mm	h5 = 7.5mm	9.35	34.9

We compare the radiation pattern of the antenna with and without the grids in Figs. 11 and 12. A significant enhancement in polarization purity can be appreciated. The improvement of the horn gain employing the EBG structure relative to the simple horn is shown in Figs. 13-15 for the three main cuts. Finally, return losses have been also computed and measured considering the antenna with and without grids. Figures 16-17 depict the results.

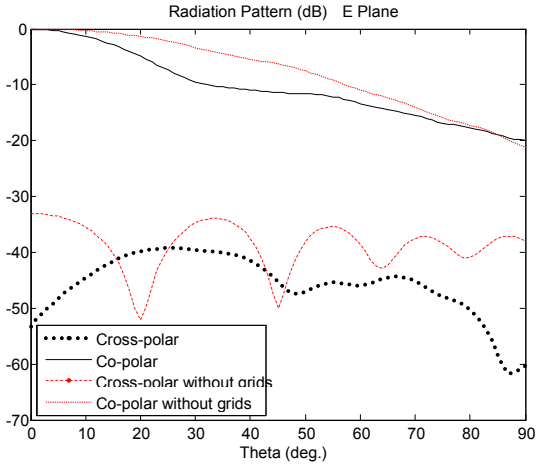

Fig. 11. Comparison between the simulated radiation patterns with and without grids. E-plane cut at 9.0 GHz.

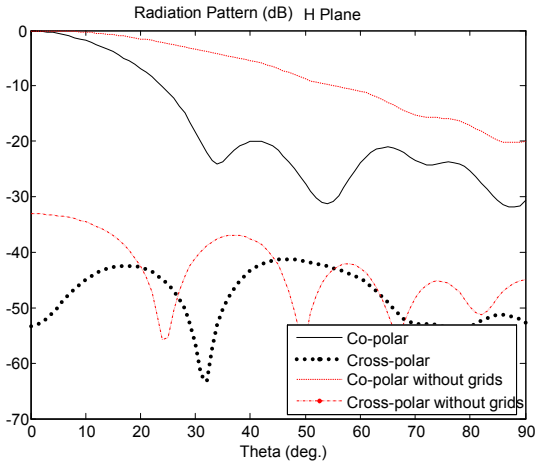

Fig. 12. Comparison between the simulated radiation patterns with and without grids. H-plane cut at 9.0 GHz.

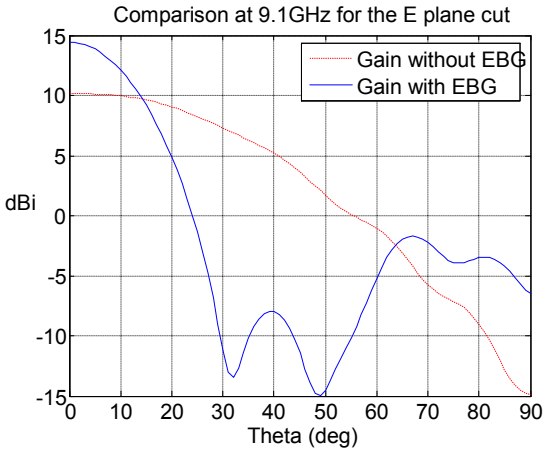

Fig. 13. Comparison for the antenna gain in the E-plane cut with and without grids.

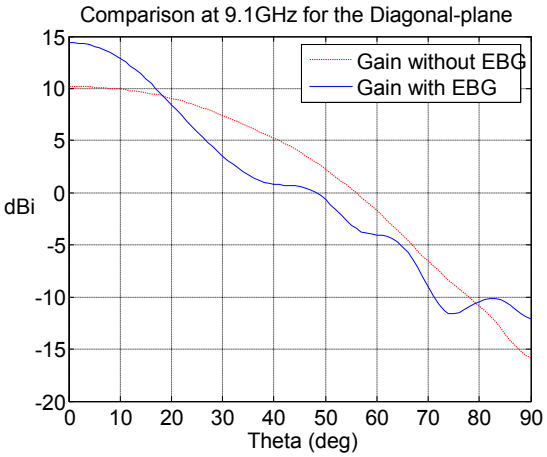

Fig. 14. Comparison for the antenna gain in the diagonal-plane cut with and without grids.

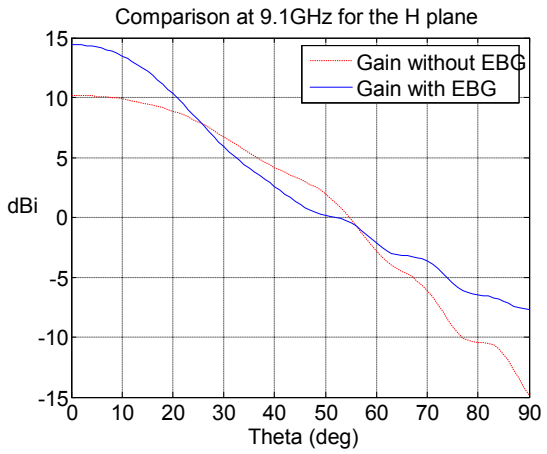

Fig. 15. Comparison for the antenna gain in the H-plane cut with and without grids.

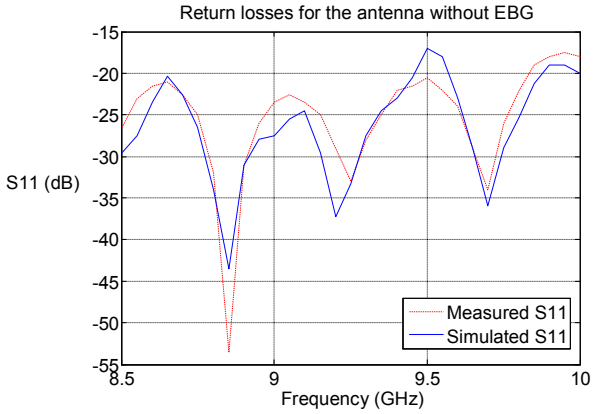

Fig. 16. Comparison of the return losses for the antenna without EBG.

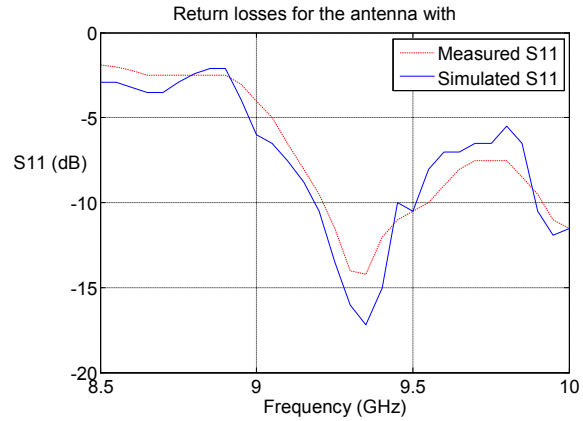

Fig. 17. Comparison of the return losses for the antenna with EBG.

IV. CONCLUSIONS

A novel compact EBG antenna operating at 9.1GHz has been presented. This new EBG antenna is an excellent candidate for several applications due to its good polarization purity. One of these applications is the design of compact antennas of medium or moderate gain and good polarization purity. Although a common horn antenna with an aperture surface equal to the proposed EGB antenna presents better performances in terms of directivity and polarization purity, the horn requires a length two or three times greater due to the large taper section it needs to fit the waveguide cross section to its final aperture surface. A second application is the design of arrays using the proposed antenna as a unit cell, as it is shown in Fig. 18. It is expected

that the array will have good radiation characteristics for feeding multibeam reflector antennas which require a relative high gain for each array element. In this particular case, the usage of an array of horn antennas with similar gain is very difficult because of the collision between horns due to their large aperture size.

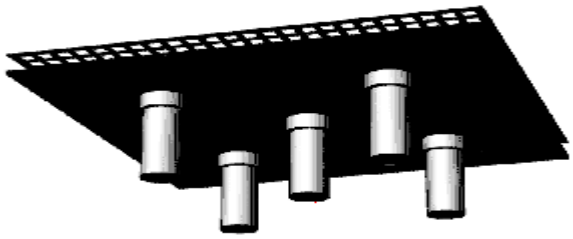

Fig. 18. Geometrical model of an array of antennas composed by five small waveguide antennas and an EBG structure that acts as a lens.

ACKNOWLEDGMENT

This work has been supported, in part by the Comunidad de Madrid Project S-2009/TIC1485, by the Castilla-La Mancha Project PPII10-0192-0083, by the Spanish Department of Science, Technology Projects TEC 2010-15706 and CONSOLIDER-INGENIO Nº CSD-2008-0068.

REFERENCES

[1] M. Thevenot, C. Cheype, A. Reineix, and B. Jecko, "Directive Photonic- Bandgap Antennas", *IEEE Transactions on Microwave Theory and Techniques*, vol. 47, no. 11, November 1999.

[2] G. K. Palikaras, A. P. Feresidis, and J. C. Vardaxoglou, "Cylindrical Electromagnetic Bandgap Structures for Directive Base Station Antennas", *IEEE Antennas and Wireless Propagation Letters*, vol. 3, 2004.

[3] A. R. Weily, K. P. Esselle, T. S. Bird, and B. C. Sanders, "Dual Resonator 1-D EBG Antenna with Slot Array Feed for Improved Radiation Bandwidth", *IET Microwaves, Antennas & Propagation*, vol. 1, no. 1, February 2007.

[4] J.-W. Baik, S.-M. Han, C. Jeong, J. Jeong, and Y.-S. Kim, "Compact Ultra-Wideband Bandpass Filter With EBG Structure", *Microwave and Wireless Components Letters*, vol. 18, no. 10, October 2008.

[5] Y. Rahmat-Samii, "The Marvels of Electromagnetic Band Gap (EBG) Structures," *ACES Journal*, vol. 18, no. 3, pp. 1-10, 2003.

[6] G. V. Trentini, "Partially Reflecting Sheet Arrays", *IRE Transactions on Antennas and Propagation*, vol. 4, pp. 666–671, October 1956.

[7] I. González, E. Garcia, F. Saez de Adana, and M. F. Cátedra., "MONURBS: A Parallelized Multipole Multilevel Code for Analyzing Complex Bodies Modeled by NURBS Surfaces", *Applied Computational Electromagnetics Society (ACES) Journal,* vol. 23, no. 2, June 2008.

Josefa Gómez Pérez was born in 1984. She received the B.S. and M.S. degrees in Telecommunications Engineering from the University Polytechnic of Cartagena (UPCT), Spain, in 2005 and 2007, respectively. Since 2007, she is pursuing the Ph.D. degree at the Computation Science Department, University of Alcalá, Spain. She has participated in several research projects with Spanish and European companies. She has published three papers and more than fifteen conference contributions at international symposia. Her research interests are design and optimization of antennas, electromagnetic radiation and scattering, on-board antennas analysis and design of graphical user interfaces.

Abdelhamid Tayebi Tayebi was born in 1983. He received the B.S. and M.S. degrees in Telecommunications Engineering from the University Polytechnic of Cartagena (UPCT), Spain, in 2005 and 2007, respectively. Since 2007, he currently is pursuing the Ph.D. degree at the Computation Science Department, University of Alcalá, Spain. He has participated in several research projects with Spanish and European companies. He has published three papers and more than fifteen conference contributions at international symposia. His research interests are design and optimization of antennas, electromagnetic radiation and scattering, on-board

antennas analysis and design of graphical user interfaces.

Iván González Diego was born in Torrelavega, Spain in 1971. He received the B.S. and M.S. degrees in Telecommunications Engineering from the University of Cantabria, Spain, in 1994 and 1997, respectively, and the Ph.D. degree in Telecommunications Engineering from the Univeristy of Alcalá , Madrid, Spain in 2004. He worked in the Detectability Laboratory of the National Institute of Technical Aerospace (INTA), Madrid, Spain in RCS prediction and measurements and as Assistant Researcher at the University of Alcalá. Since 2004, he works as Assistant Professor in the University of Alcalá in the Computation Science Department teaching concepts about Data Base Systems. He has participated in several research projects with Spanish and European companies, related with analysis of on board antennas, radio propagation in mobile communications, RCS computation, etc. His research interests are in numerical methods applied to the electromagnetic problems, rigorous and asymptotic techniques like Method of Moments, GTD/UTD, PO, etc. Also, the numerical methods to represent complex bodies for the electromagnetic techniques and computer graphics is one of his research area.

Manuel F. Cátedra Pérez received his M.S. and Ph.D. degrees in Telecommunications Engineering from the Polytechnic University of Madrid (UPM) in 1977 and 1982, respectively. From 1976 to 1989, he was with the Radiocommunication and Signal Processing Department of the UPM. He has been Professor at the University of Cantabria from 1989 to 1998. He is currently Professor at the University of Alcalá, in Madrid, Spain. He has worked on about 90 research projects solving problems of Electromagnetic Compatibility in Radio and Telecommunication Equipment, Antennas, Microwave Components and Radar Cross Section and Mobile Communications. He has developed and applied CAD tools for radio-equipment systems such as Navy-ships, aircraft, helicopters, satellites, the main contractors being Spanish or European Institutions such as EADS, ALCATEL, CNES, ALENIA, ESA, DASA, SAAB, INTA, BAZAN, INDRA, the Spanish Defence Department.

He has directed about 18 Ph.D. dissertations, has published about 70 papers (IEEE, Electronic Letters, etc), three books, about 10 chapters in different books, has given short courses and has given around a hundred and thirty presentations in International Symposia.

An Alternative Multiresolution Basis in EFIE for Analysis of Low-Frequency Problems

Jianjun Ding, Jian Zhu, Ru-shan Chen, Z. H. Fan, and K. W. Leung

Department of Electronic Engineering
Nanjing University of Science and Technology, Nanjing, 210094, China
draksea@yahoo.com, zhujian82gogo@hotmail.com, eerschen@mail.njust.edu.cn,
zhfan@mail.njust.edu.cn, eekleung@cityu.edu.hk

Abstract ― An alternative multiresolution (MR) basis is presented for the method-of-moments (MoM) solution of the electric-field integral equation (EFIE) for the analysis of low-frequency problems. The proposed MR basis functions can be treated as an extension of the traditional loop-tree basis function to hierarchical functions. Similar to the loop-tree basis, the MR basis functions are linear combinations of standard Rao-Wilton-Glisson (RWG) functions. Therefore, the MR algorithm can be easily applied to MoM codes with RWG basis. Since the MR basis is immune from the so-called low-frequency breakdown, the MR basis is especially suitable for the analysis of low-frequency problems. Compared with the previous MR basis, the present MR basis is easier to construct and comprehend, and the basis-changing matrix is sparser. Physical interpretation and comparison are given for the previous and present MR bases. Numerical results demonstrate that the both the previous and present MR bases are efficient for 3D electromagnetic scattering problems at low frequencies.

Index Terms ― EFIE, electromagnetic scattering, low frequency, method of moments (MoM), multiresolution techniques.

I. INTRODUCTION

The method of moments (MoM) is one of the most powerful numerical methods applicable to a wide variety of practical electromagnetic radiation and scattering problems [1, 2]. The electric field integral equation (EFIE) is always preferred in MoM. However, the EFIE suffers the so called low-frequency breakdown problem which occurs when the harmonic field wavelength is substantially larger than the characteristic size of the MoM grid. An effective solution to this problem is to separate the solenoidal part of the current [3-11]. The loop-star basis and loop-tree basis are proposed in early 1980s [3, 4]. Both of them introduce divergence-free loop functions which can effectively separate the solenoidal part of the current. The detailed discussion and application of the loop-star basis and loop-tree basis can be found in [5-9], and a comparison of the frequency dependent iterative solver convergence for RWG, loop-tree, and loop-star basis functions is given in [10].

In recent years, the multiresolution (MR) basis has been proposed and acted as an efficient physics-based preconditioner [12-27]. Compared with the loop-star/tree basis, the MR basis has a much faster MoM convergence rate when an iterative solver is applied. The reasons why the MR basis can positively act on the spectrum of a MoM matrix has been investigated and discussed in [20, 21]. The MR basis was first mentioned by G. Vecchi in [7], where he pointed out that a MR basis can be efficiently constructed to replace the loop-star basis. Consequently, a MR basis was proposed in [12]. Then, a modified MR basis was proposed in [13] to simplify the generation procedure. However, the MR bases in [12, 13] has a limit in modeling the curved structures, since the shape of the hierarchical meshes is restricted by the coarse mesh. To remedy this drawback of MR basis, a curvilinear MR basis is proposed in [15]. More recently, a new MR algorithm was proposed in [16-19] to overcome the shortcoming of the MR

basis defined over triangular patches. In the new MR algorithm, the concepts of the generalized mesh and generalized RWG (gRWG) basis were introduced. The generalized mesh is generated by a grouping algorithm. The gRWG basis is the generalization of the standard RWG basis and it is defined on the generalized meshes. The new MR basis functions are constructed as linear combinations of gRWG basis functions and can finally be represented by linear combinations of the RWG basis functions.

Inspired by the novel idea of generalized mesh and generalized RWG basis, an alternative MR basis is proposed in this paper which is also defined on the generalized meshes. Contrary to the MR algorithm in [16-19] which relies on mathematical operations, the MR basis proposed in this paper is generated via geometric operations. Compared with the previous MR basis, the proposed MR basis can be constructed in a much easier fashion and provide more direct physical meanings. Also, the basis-changing matrix of the RWG basis functions to the MR basis functions is sparser and can be generated faster. Furthermore, physical interpretations are provided for both MR bases and the number of MR basis functions of each level is clearly given which explains why the MR bases span the same space as the RWG basis. Numerical examples demonstrate that the MR bases have a much faster convergence rate for iterative solvers than the traditional loop-tree basis as explained in [20, 21].

This paper is organized as follows. Section II introduces the hierarchical generalized meshes and the gRWG basis. Section III gives a detailed description of the MR basis generation. Section IV provides physical interpretations for the MR bases. A discussion on the computational complexity of the MR basis is given in Section V. Section VI presents numerical results to validate and demonstrate the performance of the MR basis. Finally, the work is concluded in Section VII.

II. GENERALIZED MESH AND GRWG BASIS

Before discussing the new MR basis, the essential concepts of the generalized mesh and gRWG basis are briefly described as preliminary knowledge. Since the detailed generation algorithm of the generalized mesh and gRWG basis has already been given in [17, 18], only a brief description is provided in this section.

A. Hierarchical generalized meshes

Generation of the hierarchical generalized meshes starts from an input triangular mesh which is called level-0 mesh and denoted by M^0. Using a grouping algorithm, the nearby cells of the level-0 mesh are grouped into level-1cells. The union of the level-1 cells is called level-1 mesh, M^1. Applying the same grouping algorithm to the level-1 cells will generate the level-2 mesh (M^2) and so on and a set of hierarchical generalized meshes $\{M^l,\ l = 1, \ldots, L\}$ will be obtained. The last level L is usually decided by the maximum size of the generated cells that should be smaller than the wavelength, with a typical range of $\lambda/8 - \lambda/4$. To demonstrate the grouping algorithm, the hierarchical generalized meshes of a circular plate are shown in Fig. 1.

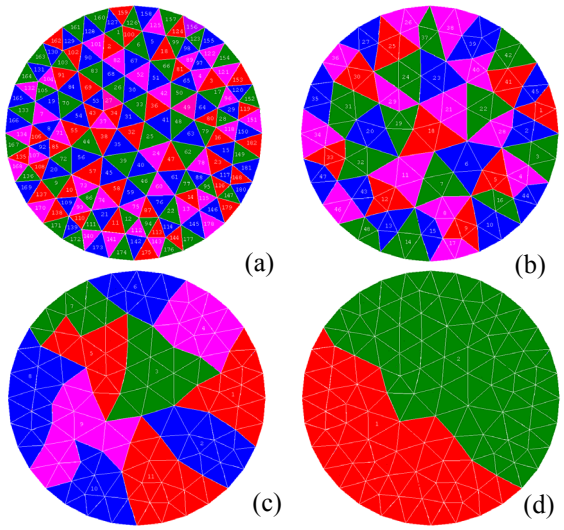

Fig. 1. An example of hierarchical generalized meshes on a circular plate. (a) level-0 mesh, (b) level-1 mesh, (c) level-2 mesh, (d) level-3 mesh.

B. Generalized RWG basis

Similar to the definition of the RWG basis, a gRWG basis function is defined on a pair of adjacent cells of its corresponding level. Denoting a level-l gRWG basis function as $\vec{R}_i^l(\vec{r})$, its divergence is given as

$$\nabla_s \cdot \vec{R}_i^l(\vec{r}) = \begin{cases} \ell_i^l / A_{+,i}^l & \vec{r} \in C_{+,i}^l \\ -\ell_i^l / A_{-,i}^l & \vec{r} \in C_{-,i}^l \\ 0 & \text{otherwise,} \end{cases} \quad (1)$$

where $A_{+,i}^l$ and $A_{-,i}^l$ are the areas of the two adjacent cells ($C_{+,i}^l$, $C_{-,i}^l$), and ℓ_i^l is the length of the level-*l* generalize edge shared by the two cells and is a polygonal line in general.

C. Inter-mesh reconstruction relationship

The inter-mesh reconstruction relationship can be derived through the charge matrix. In the inter-mesh reconstruction relationship, a level-*l* *g*RWG function $\vec{R}_i^l(\vec{r})$ can be expressed as the linear combination of the level-(*l*-1) gRWG functions $\vec{R}_n^{l-1}(\vec{r})$ (n = 1,…, N_i^{l-1}) which are completely defined in the domain $C_{+,i}^l \cup C_{-,i}^l$ of $\vec{R}_i^l(\vec{r})$, i.e.

$$\vec{R}_i^l(\vec{r}) = \sum_{n=1}^{N_i^{l-1}} R_{n,i}^l \vec{R}_n^{l-1}(\vec{r}) . \tag{2}$$

where $R_{n,i}^l$ is the reconstruction coefficient. Applying the surface divergence to both sides of (2), we have

$$\nabla_s \cdot \vec{R}_i^l(\vec{r}) = \sum_{n=1}^{N_i^{l-1}} R_{n,i}^l \nabla_s \cdot \vec{R}_n^{l-1}(\vec{r}), \tag{3}$$

Projecting (3) on the cells C_m^{l-1} (m = 1, …, $N_{c,i}^{l-1}$) in the domain of $\vec{R}_i^l(\vec{r})$, a linear system can be obtained as

$$\left[Q_i^l\right] \cdot \left[R_i^l\right] = \left[q_i^l\right], \tag{4}$$

where $\left[Q_i^l\right]$ is the $N_{c,i}^{l-1} \times N_i^{l-1}$ charge matrix whose element is given by

$$\left[Q_i^l\right]_{m,n} = \nabla_s \cdot \vec{R}_n^{l-1}(\vec{r})\Big|_{C_m^{l-1}}$$

$$\left[R_i^l\right] = \left[R_{1,i}^l, R_{2,i}^l, \ldots, R_{N_i^{l-1},i}^l\right]^T, \ \left[q_i^l\right]_m = \nabla_s \cdot \vec{R}_n^l(\vec{r})\Big|_{C_m^{l-1}} .$$

As will be discussed in the next section, the maximum number of the linear independent functions $\vec{R}_n^{l-1}(\vec{r})$ (n = 1,…, N_i^{l-1}) is $N_{c,i}^{l-1} - 1$ according to Euler's theorem. Therefore, the rank of the matrix $\left[Q_i^l\right]$ is $N_{c,i}^{l-1} - 1$ and a full row rank matrix $\left[\tilde{Q}_i^l\right]$ can be obtained by deleting an arbitrary row of $\left[Q_i^l\right]$. When $N_{c,i}^{l-1} - 1 < N_i^{l-1}$, the matrix equation (4) has infinitely many solutions and the least squares solution can be taken as the reconstruction coefficients $\left[R_i^l\right]$, i.e.

$$\left[R_i^l\right] = \left[\tilde{Q}_i^l\right]^+ \left[q_i^l\right], \tag{5}$$

where $\left[\tilde{Q}_i^l\right]^+$ is the Moore-Penrose pseudoinverse of $\left[\tilde{Q}_i^l\right]$.

III. MR BASIS GENERATION

For a general 3-D surface (without torus), the Euler's theorem states that [9, 19]

$$V + F = E - N_\Gamma + 2, \tag{6}$$

where V, E, F, N_Γ denote the number of vertices, edges, faces, and separated boundary contours, respectively. Since the number of vertices and edges on the boundary contours is equal, we have

$$V_{\text{int}} + F = E_{\text{int}} - N_\Gamma + 2, \tag{7}$$

where V_{int}, E_{int} is the number of internal vertices and edges, respectively.

For a domain (e.g. a cell or a pair of cells of level-*l*) composed of $N_{c,i}^{l-1}$ cells of level-(*l*-1), we have

$$N_i^{l-1} - (V_{\text{int}} + N_\Gamma - 1) = N_{c,i}^{l-1} - 1 . \tag{8}$$

N_i^{l-1} is the number of the gRWG functions in the domain, since the gRWG functions are defined on the interior edges. If connecting all the cells in a tree (see e.g. Fig. 2) and avoid forming any loop on the tree, then the maximum number of edges on the tree will be $N_{c,i}^{l-1} - 1$. Obviously, the gRWG functions corresponding to the edges on the tree are linear independent. Therefore, the maximum number of the linear independent gRWG functions in the domain is equal to $N_{c,i}^{l-1} - 1$.

If the surface is discretized with triangles, the number of solenoidal functions N_S and the number of nonsolenoidal functions N_X of loop-star basis are given by [7, 9]

$$N_S = V_{\text{int}} + N_\Gamma - 1 \tag{9}$$

$$N_X = F - 1 . \tag{10}$$

Their sum is equal to the number of the RWG functions, i.e.

$$N_S + N_X = N, \tag{11}$$

where N is the number of the RWG functions.

Similar to the loop-star/tree basis, the MR basis can also be split into the solenoidal and nonsolenoidal parts. It will be shown in the next section that the solenoidal and nonsolenoidal functions of the MR basis span the same space as for the loop-tree/star basis, and the numbers of the solenoidal and nonsolenoidal functions of the MR basis can also be given by equations (9)-(11).

A. Solenoidal basis

It has already been shown in [17] that the use of a hierarchical decomposition of the nonsolenoidal part together with a non hierarchical loop basis suffices to obtain well conditioned MoM matrices and, hence, quickly convergent solvers for low-frequency and very dense discretizations. The difference between the low-frequency and very dense discretization is addressed in [11]. Therefore, for simplicity, the loop basis generated on level-0 mesh is chosen as the solenoidal part of the MR basis. The detailed discussion of the loop basis can be found in [7, 9], whereas the topic of generating the loop basis functions on the more complex surfaces (e.g. wire-surface structure) can be found in [28].

After generating the loop basis, the solenoidal basis of the MR basis can be written as

$$\left[\vec{f}_L\right]=\left[T_L\right]^T\left[\vec{R}^0\right], \tag{12}$$

where $\left[\vec{f}_L\right]^T=\left[\vec{f}_{1,L},\vec{f}_{2,L},\ldots,\vec{f}_{N_S,L}\right]$ is the solenoidal MR basis, $\left[T_L\right]$ is the basis-changing matrix, and $\left[\vec{R}^0\right]^T=\left[\vec{R}^0_1,\vec{R}^0_2,\ldots,\vec{R}^0_N\right]$ is the RWG basis of level-0 mesh.

B. Nonsolenoidal basis

The nonsolenoidal basis is defined on the hierarchical generalized meshes. The nonsolenoidal basis functions of the highest level (level-L) are different from the nonsolenoidal basis functions of other levels (level-l, l = 1, …, L-1). Therefore, the nonsolenoidal basis functions of level-L are generated separately from the function of the other levels.

1). Nonsolenoidal Functions of Level-L

The generation of the nonsolenoidal functions of level-L is similar to that of the tree basis functions in the loop-tree basis. The only difference is that the cells of level-L are replaced by triangles. An easy procedure of constructing the nonsolenoidal functions of level-L is to connect the cells of level-L mesh in a tree, and each gRWG basis function on the branch of the tree is taken as a nonsolenoidal function. To demonstrate this procedure, the nonsolenoidal functions defined on the level-2 mesh (Fig. 1) are plotted. In this example, it is assumed that the level-2 mesh is of the highest level. As shown in Fig. 2 (a), each black line connecting a pair of cells represents a generated nonsolenoidal function. It is worth mentioning that the number of the nonsolenoidal functions of level-L equals the number of the cells of level-L minus one.

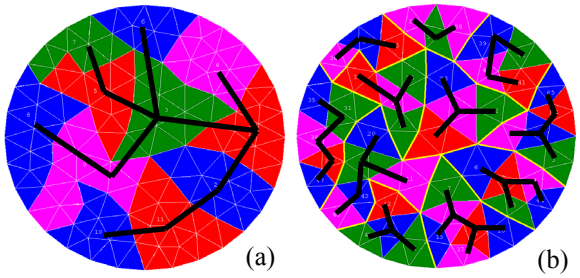

Fig. 2. The nonsolenoidal functions, which are depicted with black lines, on a circular plate. (a) Level-2 functions, (b) level-1 functions.

2). Nonsolenoidal Functions of Level- l (l = 1, …, L-1)

Let the nonsolenoidal functions of level-l belong to the cell C_k^{l+1} of level-(l+1) denoted with $\left\{\vec{f}^{\,l}_{k,i}, i=1,\cdots,N^l_{C_k^{l+1}}-1\right\}$, in which $N^l_{C_k^{l+1}}$ is the number of the cells of level-l belonging to the cell C_k^{l+1}, the nonsolenoidal functions of level-l can be expressed as the union of the nonsolenoidal functions that belong to all the cells of level-(l+1), i.e.

$$\left\{\vec{f}^{\,l}_{j,X}, j=1,\cdots,N^l_c-N^{l+1}_c\right\}=\bigcup_{k=1}^{N_c^{l+1}}\left\{\vec{f}^{\,l}_{k,i}, i=1,\cdots,N^l_{C_k^{l+1}}-1\right\}, \tag{13}$$

where N_c^l and N_c^{l+1} are the numbers of the cells of level-l and level-(l+1) respectively, and $N_c^l-N_c^{l+1}$ is the number of the nonsolenoidal functions of level-l. A simple way of generating the level-l nonsolenoidal functions in the cell C_k^{l+1} is to connect all the level-l cells which are completely included in the cell C_k^{l+1} in a tree and taking the gRWG basis functions on the branches of the tree as nonsolenoidal functions. An example of level-1 nonsolenoidal functions is shown in Fig. 2 (b). As can be observed from Fig. 2 (b), the level-2 cells are bounded with yellow lines and the level-1 nonsolenoidal functions are clustered in each level-2 cell shown with black lines.

The nonsolenoidal functions (13) can be written as linear combinations of the gRWG basis functions of level-l, i.e.

$$\left[\vec{f}_X^{\,l}\right]=\left[T'^{\,l}_{\ X}\right]^T\left[\vec{R}^{\,l}\right], \tag{14}$$

where $\left[\vec{f}_X^{\,l}\right]^T=\left[\vec{f}^{\,l}_{1,X},\vec{f}^{\,l}_{2,X},\ldots,\vec{f}^{\,l}_{N_c^l-N_c^{l+1},X}\right]$, $\left[T'^{\,l}_{\ X}\right]^T$ is the basis-changing matrix, and $\left[\vec{R}^{\,l}\right]^T=\left[\vec{R}^l_1,\vec{R}^l_2,\ldots,\vec{R}^l_{N^l}\right]$ is the gRWG basis of level-*l*. Applying the inter-mesh reconstruction relationship (2) recurrently, the nonsolenoidal functions of level-*l* can then be written as linear combinations of the RWG basis functions of level-0 mesh, i.e.,

$$\left[\vec{f}_X^{\,l}\right]=\left[T_X^l\right]^T\left[\vec{R}^0\right]. \tag{15}$$

Then, the nonsolenoidal functions of all levels can be written as

$$\left[\vec{f}_X\right]=\left[T_X\right]^T\left[\vec{R}^0\right], \tag{16}$$

where $\left[\vec{f}_X\right]^T=\left[\left[\vec{f}_X^{\,0}\right]^T,\left[\vec{f}_X^{\,1}\right]^T,\cdots,\left[\vec{f}_X^{\,L}\right]^T\right]$ and $\left[T_X\right]^T=\left[\left[T_X^0\right]^T,\left[T_X^1\right]^T,\cdots,\left[T_X^L\right]^T\right]$.

Finally, the MR basis functions can be expressed in terms of the RWG basis functions as follows

$$\left[\vec{f}_{MR}\right]=\left[T\right]^T\left[\vec{R}^0\right], \tag{17}$$

where $\left[T\right]=\left[\left[T_L\right],\left[T_X\right]\right]$.

IV. PHYSICAL INTERPRETATION OF MR BASES

Although the generation algorithm of the MR basis proposed in [18, 19] is clearly given, the physical meaning behind it is not clearly pointed out. Readers may also be confused about why the number of the MR basis functions equals the number of the RWG basis functions. Therefore, physic interpretations are tried to give in this section for both the present MR basis and the previous MR basis for better understanding of the MR bases.

A. The present MR basis

From the discussion given in Section III-B, the total number of the nonsolenoidal functions can be calculated as

$$\begin{aligned} N_X &= N_X^0+N_X^1+\cdots+N_X^L \\ &=(F-N_c^1)+(N_c^1-N_c^2)+\cdots+(N_c^L-1)\cdot \\ &=F-1 \end{aligned} \tag{18}$$

Therefore, the numbers of the nonsolenoidal functions of the MR basis also satisfy (10). Similar to the loop-tree/star basis, it can be easily proven that all the solenoidal and nonsolenoidal functions of the present MR basis are linear independent from each other. Therefore, the MR basis spans the same space as for the loop-star/tree basis.

B. The previous MR basis

The previous MR basis functions proposed in [18, 19] are constructed via SVD on charge matrices. After applying SVD on a charge matrix, the right singular vectors associated to non-zero and null singular values are assigned as the coefficients of the corresponding gRWG function to generate the solenoidal and nonsolenoidal MR functions, respectively. However, the reason is not explained. In the following, a physical explanation to the above mathematical operations is given. Assuming a charge matrix generated by projecting *n* level-*l* gRWG functions onto *m* level-*l* cells, then its SVD result can be written as

$$\begin{aligned} [Q]&=\left[\nabla\cdot R_1,\nabla\cdot R_2,\cdots,\nabla\cdot R_n\right]=[U]\cdot[\Sigma]\cdot[V]^T \\ &=\left[U_1,U_2,\cdots,U_m\right]\cdot diag(\sigma_1,\sigma_2,\cdots,\sigma_{m-1})\cdot \\ &\quad\left[V_1,V_2,\cdots,V_n\right]^T \end{aligned}, \tag{19}$$

where $\sigma_1\ge\sigma_2\ge\cdots\ge\sigma_{m-1}>0$, since the rank of [*Q*] is *m*-1. The expression (19) can be rewritten as

$$\begin{aligned} &\nabla\cdot\left[R_1,R_2,\cdots,R_n\right]\cdot\left[V_1,V_2,\cdots,V_n\right]= \\ &\left[\sigma_1U_1,\sigma_2U_2,\cdots,\sigma_{m-1}U_{m-1},0\cdot U_m,\cdots,0\cdot U_n\right] \end{aligned}. \tag{20}$$

It can be inferred from (20) that the gRWG functions multiplies the first *m*-1 columns of [*V*] generates *m*-1 linear independent functions which have surface charge and can be taken as the nonsolenoidal functions. Therefore, the number of the nonsolenoidal functions generated with the algorithm in [17, 18] can also be given by (18). Namely, the numbers of the MR nonsolenoidal functions in the present paper and in [17, 18] are equal. It can also be inferred from (20) that the gRWG functions multiplies the other *n*-*m* columns of [*V*] generates *n*-*m* linear independent functions which have no surface charge and can be taken as the solenoidal functions.

It can be inferred from the discussion at the beginning of section III that the number of the level-*l* solenoidal functions in a level-(*l*+1) cell (except the level-*L* cell of closed surfaces which has no boundary) equals the number of the interior vertexes shared by the *level-l* edges inside the level-(*l*+1) cell. Furthermore, the number of the

level-l solenoidal functions added by generating solenoidal functions across a pair of level-(l+1) cells equals the number of the interior vertexes which connecting the level-l edges that coincide with the common edge of the two level-(l+1) cells. Therefore, the total number of the MR basis functions generated in [18, 19] can be finally described by (21). It can be proven by theorem 1 that the number of the MR basis functions equals the number of the RWG basis functions of the input mesh.

Theorem 1 *The number of the RWG basis functions of the input mesh can be written as the sum of the following elements:*

$$N = \sum_{l=0}^{L} N_e^l + \sum_{l=1}^{L} \left(\sum_{n=1}^{N_e^l} N_{v,n}^l \right), \tag{21}$$

where N_e^l *(l=L) is the number of the level-L interior edges and* $N_e^l = \sum_{m=1}^{N_c^{l+1}} N_{e,m}^l$ *(0⩽l<L-1) is the total number of the level-l interior edges inside all level-(l+1) cells, in which* $N_{e,m}^l$ *is the number of the level-l edges inside the m-th level-(l+1) cell and* N_c^{l+1} *is the number of level-(l+1) cells, and* $N_{v,n}^l$ *is the number of the interior vertexes on the n-th level-l interior edges*.

Proof: The expression (21) can be interpreted by the changes of the interior edges of each level in the procedure of generating the hierarchical meshes. In the first step of the mesh generating procedure, the level-1 mesh is generated from the input mesh (level-0) and parts of the level-0 interior edges are grouped into the level-1 interior edges. Since the number of the level-0 interior edges grouped into one level-1 interior edge equals the number of the level-0 interior vertexes on the level-1 interior edge plus one, the total number of the grouped level-0 interior edges equals the total number of level-0 interior vertexes on the level-1 interior edges plus the number of the level-1 interior edges. Namely, the number of the level-0 interior edges can be decomposed as the sum of the total number of the level-0 interior edges inside all level-1 cells (i.e. the number of the left level-0 interior edges), the total number of level-0 interior vertexes on the level-1 interior edges, and the number of the level-1 interior edges. Similarly, the number of the level-l ($1 \leqslant l<L$-1) interior edges can be decomposed as the sum of the total number of the level-l interior edges inside all level-(l+1) cells, the total number of level-l interior vertexes on the level-(l+1) interior edges, and the number of the level-(l+1) interior edges. As a consequence, the number of the level-0 interior edges can be finally written as (21). Since each RWG basis function of the input mesh is corresponding to a level-0 interior edge, theorem 1 is proven.

It can be inferred from the above discussion that the number of the solenoidal and nonsolenoidal functions of the previous MR basis functions can also be given by equations (9)-(11). The level-L functions of the previous MR basis should be constructed independently if the cells are not finally grouped into one big cell. The level-L functions of the previous MR basis could be generated by applying SVD on the charge matrix generated by projecting the level-L gRWG functions on the level-L cells or simply taking the level-L gRWG basis functions as the level-L MR basis functions. It can also be inferred from Theorem 1 that the solenoidal part of the present MR basis can be constructed as a hierarchical basis in which each solenoidal function is generated as a linear combination of the gRWG functions of the same level which constitute a loop around an interior vertex.

V. COMPUTATIONAL COMPLEXITY

Since the computational complexity of the loop basis is known as $O(N)$ [28], only the computational complexity of the nonsolenoidal MR basis is needed to be analyzed. The computational complexity of the nonsolenoidal MR basis can be estimated by estimating the number of on-zero elements of the basis-changing matrix [T].

The number of non-zero elements of the basis-changing matrix [T] as the functions of the number of levels of a structure discretized with 19090 unknowns is investigated and shown in Fig. 3. It can be observed from Fig. 3 that the number of non-zero elements of matrix [T] increase linearly with the number of the levels of the MR basis. Therefore, the computational complexity of the nonsolenoidal MR basis is of $O(NL)$, where L is the number of levels. If we keep grouping the cells

of each level upwards until the cells are finally grouped into one single cell in the highest level mesh, the number of levels L will be equal to Log$N$ and the computational complexity will be of $O(N\text{Log}N)$. The number of non-zero elements and the generation time of matrix [T] as functions of the number of the unknowns for the previous MR basis and present MR basis when the cells are finally grouped into a single cell are investigated and shown in Fig. 4 (a) and (b), respectively. It can be observed from the figure that the computational complexity of both the previous and present MR basis is of $O(N\text{Log}N)$ and the computational complexity of the present MR basis has a smaller constant.

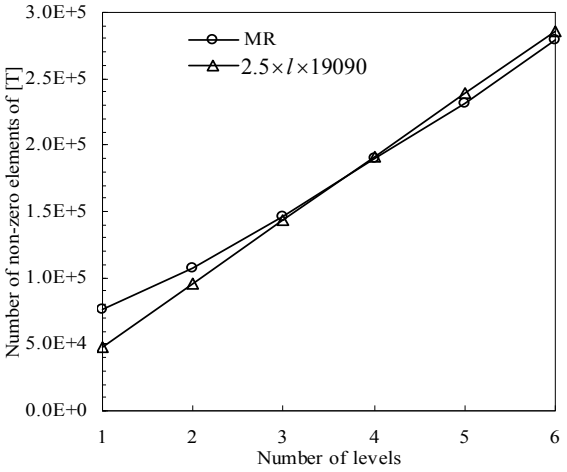

Fig. 3. The number of non-zero elements of the basis-changing matrix [T] versus the number of levels of a structure discretized with 19090 unknowns.

VI. NUMERICAL RESULTS

In this section, the MR basis is applied for the analysis of the EM scattering problems at low frequencies. In the following examples, the restarted GMRES(30) algorithm is used as an iterative method. All simulations were performed on a PC computer with Intel(R) Core(TM)2 1.86 GHz CPU and 2 GB RAM using single precision. Zero vector is taken as initial approximate solution and the iteration process is terminated when the relative backward error is reduced by 10^{-4}. And all the results with different bases were obtained after applying a diagonal preconditioning to the MoM matrix.

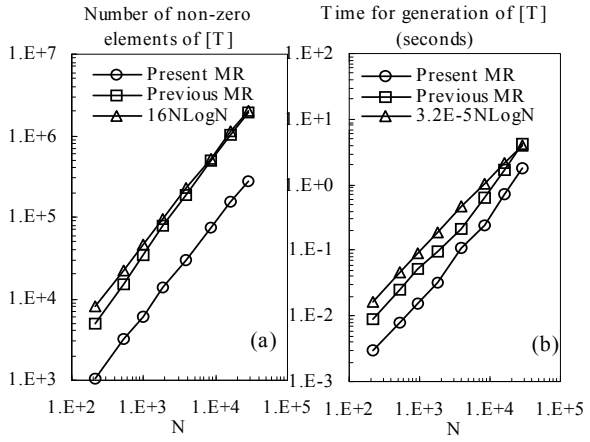

Fig. 4. (a) The number of non-zero elements of the basis-changing matrix [T], (b) the time for generation of matrix [T], versus the number of unknowns.

A. Offset bend rectangular cavity

The first example is a metallic offset bend rectangular cavity with 8.7 cm by 10 cm square cross section and offset angles 30°. As shown in Fig. 5, the offset bend rectangular cavity is discretized with 4317 unknowns. The mesh of the offset bend rectangular cavity could generate six levels hierarchical meshes and five levels MR basis at most. The EM scattering of the offset bend rectangular cavity is calculated with the EFIE using the RWG, loop-tree, the previous MR, and present MR bases. The 2-norm condition numbers and the convergence behavior of GMRES(30) for the offset bend rectangular cavity using the above bases over a frequency range of 0.1-200 MHz is shown in Fig. 5 and Fig. 6, respectively. The corresponding total time for applying the MR bases is depicted in Fig. 7.

With reference to the figures, the RWG basis performs worse than both the loop-tree basis and the MR bases in the low frequency range. It can be also found that the MR bases perform much better than the loop-tree basis in the low frequency range. The more levels of the present MR basis, the better it performs in the low frequency range. Comparing the previous MR basis with the present MR basis, it can be found that the present MR basis performs similar to the previous MR basis at low frequencies. However, the previous MR basis performs more stable as the frequency increases. The corresponding total time which includes the

time of the generation of the basis-changing matrix, the time of the generation of the diagonal preconditioning matrix, and the solution time of the GMRES(30) is depicted in Fig. 6. The result using the RWG basis is not given in Fig. 6 since the GMRES(30) solver cannot converge by using the RWG basis at some frequencies. It also clearly indicates that the MR bases have better performance than the loop-tree basis at the low-frequency range.

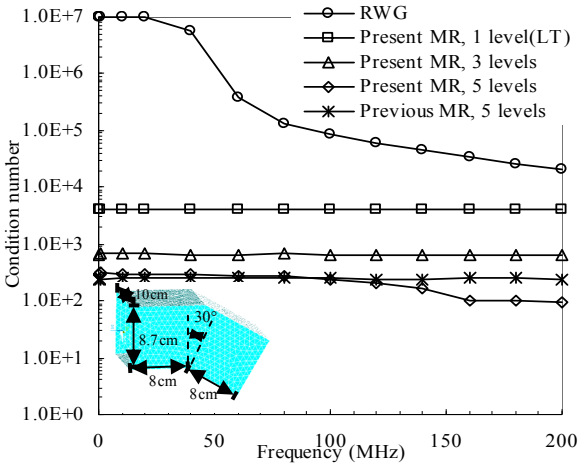

Fig. 5. The 2-norm condition number as a function of frequency for the offset bend rectangular cavity using the RWG, loop-tree, and MR bases.

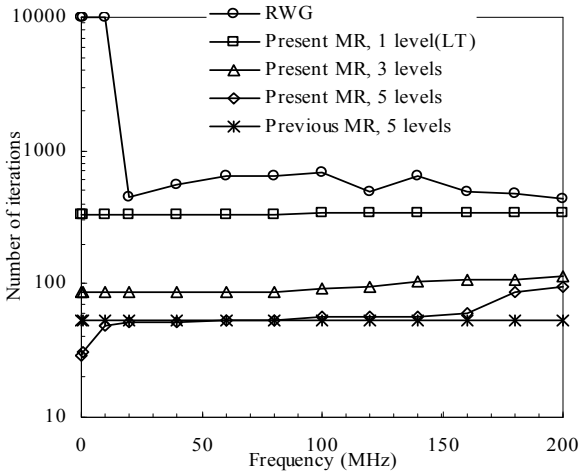

Fig. 6. The convergence behavior of GMRES(30) as a function of frequency for the offset bend rectangular cavity using the RWG, loop-tree, and MR bases.

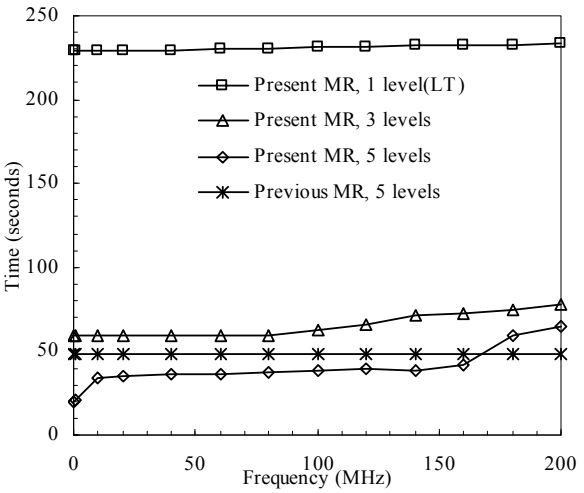

Fig. 7. The total time as a function of frequency for the offset bend rectangular cavity using the loop-tree and MR bases.

The impact of the discretization density to the performance of different bases is investigated. The 2-norm condition number of the MoM matrices using the RWG basis, loop-tree basis, and the present and previous MR bases for the offset bend rectangular cavity discretized with a different number of unknowns is shown in Fig. 8. It can be found from Fig. 8 that the MR bases perform more stable than the RWG basis and loop-tree basis as the discretization density increases and this result agrees with the results in [11].

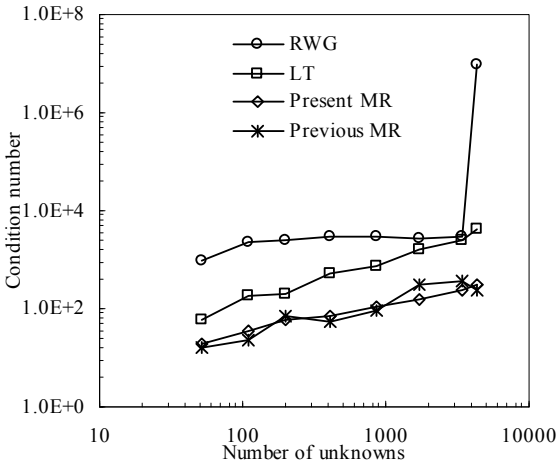

Fig. 8. The 2-norm condition number as a function of discretization density for the offset bend rectangular cavity using the RWG, loop-tree, and MR bases.

B. Tank model

As shown in Fig. 9, the second example is a tank model discretized with 8706 unknowns. The length, width, and height of the tank model are 10.3 m, 3.3 m, and 2.3 m, respectively. To describe the shape of the tank model efficiently, the parts varying rapidly in geometry are discretized with relatively small triangular patches and the other parts are with large patches.

The convergence curves of the GMRES(30) are compared in Fig. 9 at the low frequency 1.0 MHz using the RWG, loop-tree, and the MR bases. It can also be found from Fig. 9 that the convergence of the GMRES(30) using the MR bases which have higher levels is much faster than the others. The convergence behavior of GMRES(30) and the corresponding total time for applying the MR bases over a frequency range of 0.1-6 MHz is shown in Fig. 10 and Fig. 11, respectively. From Fig. 10 and Fig. 11, it can found that both the MR basis performs similar at lower frequencies and the previous MR performs more stable as the frequency increases.

VII. CONCLUSION

An alternative MR basis has been proposed for analyzing low-frequency problems using the MoM. Contrary to the previous MR basis which is generated based on mathematical operations, the present MR basis is generated based on geometrical operations. The present MR basis is an extension of the loop-tree basis to hierarchical basis, and the loop-tree can be treated as a special one-level MR basis. Therefore, the present MR basis is easier to construct and comprehend. Also, the computational complexity of the present MR basis is lower than that of the previous MR basis and the basis-changing matrix of the RWG basis to the present MR basis is sparser. As similar to the loop-tree basis, the present MR basis functions are combinations of RWG basis functions. Thus, the present MR basis can be easily applied to existing MoM codes. It has been demonstrated by the numerical results that the MR bases can be used to solve low-frequency EM scattering problems efficiently. Compared with the traditional loop-tree basis, the MR bases converge much faster at low frequencies for iterative solvers. Although the present MR basis performs similar to the previous MR basis at lower frequencies, it should be pointed out that the present MR basis suffers the same drawback as the loop-tree basis, i.e. it will be unstable as the frequency goes higher. Therefore, the previous MR basis is recommended at higher frequencies since it performs more stable as the frequency increases.

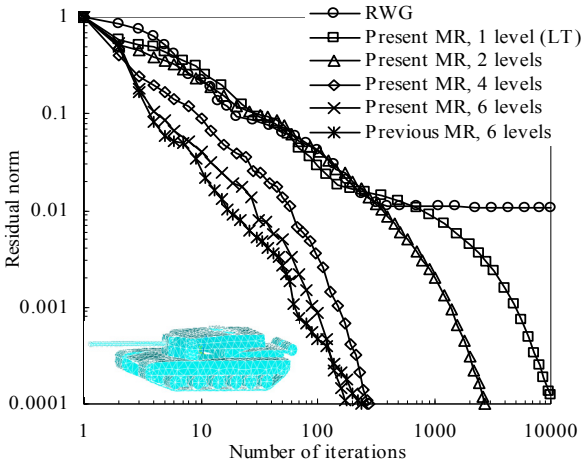

Fig. 9. The convergence history of the GMRES(30) for the tank model at 1.0 MHz using the RWG, loop-tree, and MR bases.

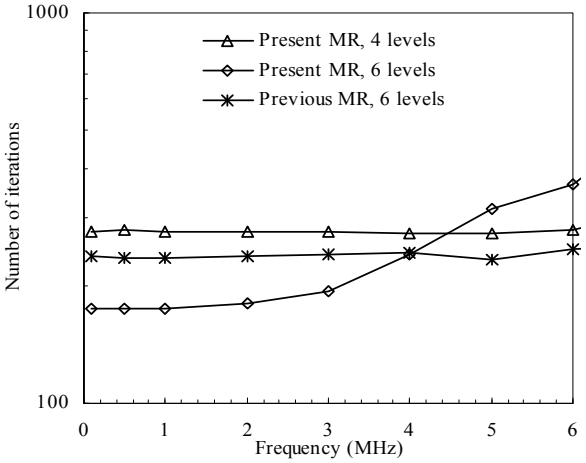

Fig. 10. The convergence behavior of GMRES(30) as a function of frequency for the tank model using the MR bases.

ACKNOWLEDGMENT

The authors would like to thank the assistance and support of Major State Basic Research Development Program of China (973 Program: 2009CB320201), Natural Science Foundation of

60871013, 60701004, and 60928002, and Jiangsu Natural Science Foundation of BK2008048.

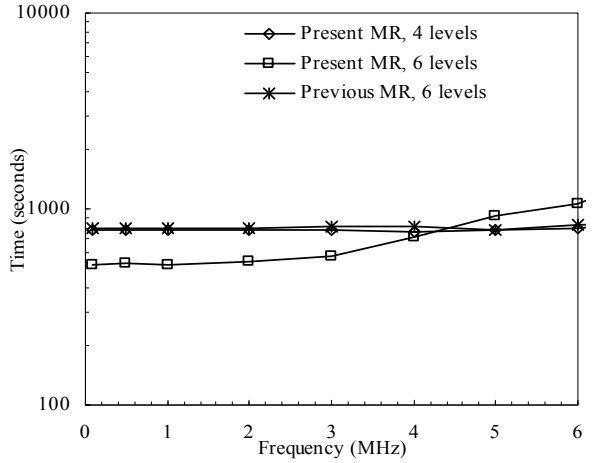

Fig. 11. The total time as a function of frequency for the tank model using the MR bases.

REFERENCES

[1] R. F. Harrington, *Field Computations by Moment Methods*, MacMillan, New York, 1968.

[2] S. M. Rao, D. R. Wilton, and A. W. Glisson, ''Electromagnetic Scattering by Surfaces of Arbitrary Shape,'' *IEEE Trans. Antennas Propagat.*, vol. AP-30, pp. 409-418, May 1982.

[3] D. R. Wilton and A. W. Glisson, "On Improving the Electric Field Integral Equation at Low Frequencies," in *Proc. URSI Radio Science Meeting Dig.*, Los Angeles, CA, p. 24, June 1981.

[4] J. Mautz and R. F. Harrington, "An E-Field Solution for a Conducting Surface Small or Comparable to the Wavelength," *IEEE Trans. Antennas Propagat.*, vol. AP-32, no. 4, pp. 330-339, April 1984.

[5] M. Burton and S. Kashyap, "A Study of a Recent Moment-Method Algorithm that is Accurate to Very Low Frequencies," *Applied Computational Electromagnetic Society (ACES) J.*, vol. 10, no. 3, pp. 58–68, Nov. 1995.

[6] W. L. Wu, A. Glisson, and D. Kajfez, "A Study of Two Numerical Solution Procedures for the Electric Field Integral Equation at Low Frequency," *Applied Computational Electromagnetic Society (ACES) J.*, vol. 10, no. 3, pp. 69–80, Nov. 1995.

[7] G. Vecchi, "Loop-Star Decomposition of Basis Functions in the Discretization of the EFIE," *IEEE Trans. Antennas Propagat.*, vol. 47, no. 2, pp. 339–346, Feb. 1999.

[8] J. S. Zhao and W. C. Chew, "Integral Equation Solution of Maxwell's Equations from Zero Frequency to Microwave Frequency," *IEEE Trans. Antennas Propagat.*, vol. 48, pp. 1635–1645, Oct. 2000.

[9] J. F. Lee, R. Lee, and R. J. Burkholder, "Loop Star Basis Functions and a Robust Precodnitioner for EFIE Scattering Problems," *IEEE Trans. Antennas Propagat.*, vol. 51, pp. 1855–1863, Aug. 2003.

[10] T. F. Eibert, "Iterative-Solver Convergence for Loop-Star and Loop-Tree Decomposition in Method-of-Moments Solutions of the Electric-Field Integral Equation," *IEEE Antennas Propag. Mag.*, vol. 46, pp. 80–85, Jun. 2004.

[11] F. P. Andriulli, A. Tabacco, and G. Vecchi, "Solving the EFIE at Low Frequencies With a Conditioning That Grows Only Logarithmically With the Number of Unknowns," *IEEE Trans. Antennas Propagat.*, vol. 58, no. 5, pp. 1614–1624, May 2010.

[12] F. Vipiana, P. Pirinoli, and G. Vecchi, "A Multiresolution Method of Moments for Triangular Meshes," *IEEE Trans. Antennas Propag.*, vol. 53, no. 7, pp. 2247–2258, Jul. 2005.

[13] F. Vipiana, G. Vecchi, and P. Pirinoli. "A Multiresolution System of Rao–Wilton–Glisson Functions", *IEEE Trans. Antennas Propagat.*, vol. 55, no. 3, pp. 924-930, Mar. 2007.

[14] F. Andriulli, A. Tabacco, and G. Vecchi, "A Multiresolution Approach to the Electric Field Integral Equation in Antenna Problems," *SIAM J. Sci. Comput.*, vol. 29, pp. 1–21, Jan. 2007.

[15] R. S. Chen, J. J. Ding, and D. Z. Ding et al, "A Multiresolution Curvilinear Rao-Wilton-Glisson Basis Function for Fast Analysis of Electromagnetic Scattering," *IEEE Trans. Antennas Propagat.*, vol. 57, no. 10, pp. 3179-3188, Oct. 2009.

[16] F. P. Andriulli, F. Vipiana, and G. Vecchi, "Enhanced Multiresolution Basis for the Mom Analysis of 3D Structures," in *Proc. IEEE Int. Symp. Antennas Propagat.*, Honolulu, HI, pp.

5612–5615, Jun. 2007.

[17] F. P. Andriulli, F. Vipiana, and G. Vecchi, "Hierarchical Bases for Non-Hierarchic 3-D Triangular Meshes," *IEEE Trans. Antennas Propagat.*, vol. 56, pp. 2288–2297, Aug. 2008.

[18] F. Vipiana, F. P. Andriulli, and G. Vecchi, "Two-Tier Non-Simplex Grid Hierarchic Basis for General 3D Meshes," *Waves in Random and Complex Media*, vol. 19, no. 1, pp.126–146, Feb. 2009.

[19] F. Vipiana, and G. Vecchi, "A Novel, Symmetrical Solenoidal Basis for the MoM Analysis of Closed Surfaces," *IEEE Trans. Antennas Propagat.*, vol. 57, no. 4, pp. 1294-1299, April 2009.

[20] F. Vipiana, P. Pirinoli, and G. Vecchi, "Regularization Effect of a Mutiresolution Basis on the EFIE-MoM Matrix," *IEEE Antennas and Propagation Society Int. Symp. Digest*, Washington, DC, vol. 3b, pp. 192–195, Jul. 2005.

[21] F. Vipiana, P. Pirinoli, and G. Vecchi, "Spectral Properties of the EFIE-MoM Matrix for Dense Meshes with Different Types of Bases," *IEEE Trans. Antennas Propagat.*, vol. 55, no. 11, pp. 3229–3238, Nov. 2007.

[22] J. J. Ding, J. Zhu, D. Z. Ding, and R. S. Chen, "Application of Perturbed Multiresolution Preconditioner Technique Combined with MLFMA for Scattering Problem," in *Proc. Int. Conf. on Microwave and Millimeter Wave Technology*, pp. 978-981, Apr. 2008.

[23] H. Chen, D. Z. Ding, R. S. Chen, D. X. Wang, and E. K. Yung, "Application of Multiresolution Preconditioner Technique for Scattering Problem in a Half Space," in *Proc. Int. Conf. on Microwave and Millimeter Wave Technology*, pp. 975–977, Apr. 2008.

[24] Y. Q. Hu, J. J. Ding, D. Z. Ding, and R.S. Chen, "Analysis of Electromagnetic Scattering from Dielectric Objects above a Lossy Half-Space by Multiresolution Preconditioned Multilevel Fast Multipole Algorithm," *IET Microw. Antennas Propag.*, vol. 4, no. 2, pp. 232–239, Feb. 2010.

[25] M. M. Li, J. J. Ding, D. Z. Ding, Z. H. Fan, and R.S. Chen, "Multiresolution Preconditioned Multilevel UV Method for Analysis of Planar Layered Finite Frequency Selective Surface," *Microwave and Optical Technology Letters*, vol. 52, no. 7, pp. 1530-1536, July 2010.

[26] F. Vipiana, M. A. Francavilla, and G. Vecchi, "A Multi-Resolution Stabilization of the Incomplete LU Preconditioner," in *Antennas and Propagation Society International Symposium*, Charleston, SC, pp. 1-4, June 2009.

[27] F. Vipiana, M. A. Francavilla, and G. Vecchi, "EFIE Modeling of High-Definition Multiscale Structures," *IEEE Trans. Antennas Propagat.*, vol. 58, no. 7, pp. 2362–2374, July 2010.

[28] F. Vipiana, G. Vecchi, and D. R. Wilton, "Automatic Loop-Tree Scheme for Arbitrary Conducting Wire-Surface Structures," *IEEE Trans. Antennas Propagat.*, vol. 57, no. 11, pp. 3564–3574, Nov. 2009.

Realistic Spatio-Temporal Channel Model for Broadband MIMO WLAN Systems Employing Uniform Circular Antenna Arrays

M. A. Mangoud and Z. Mahdi

Department of Electrical and Electronics Engineering,
University of Bahrain, P. O. Box 32038, Isa Town, Kingdom of Bahrain
Mangoud@ieee.org

Abstract ─ The development of realistic spatially and temporally clustered channel models is a prerequisite to the creation of successful architectures of the future MIMO wireless communication systems. IEEE 802.11*n* channel models are designed for indoor wireless local area networks for bandwidths of up to 100 MHz, at frequencies of 2 and 5 GHz. The channel models comprise a set of 6 realistic profiles, labeled A to F, which cover the scenarios of flat fading, residential, residential/small office, typical office, large office, and large space. Each channel scenario is represented by distinct path loss model, multipath delay profile, number of clusters and taps with predefined values for angular and power parameters. These realistic models have been applied widely for MIMO systems utilizing only uniform linear array (ULA). In this paper, modifications to the standard IEEE 802.11*n* channel model are applied to include uniform circular array (UCA) geometries. Characteristics of spatial fading corrections and the eigenvales distribution of subchannels for UCA-MIMO systems are investigated. The effect of the azimuth orientation and line of sight component existence on the system capacity for both ULA and UCA arrays are studied. Also, the water filling power allocation scheme is investigated under different realistic conditions. Furthermore, the link performance of Vertical Bell Laboratories Layered Space Time (VBLAST) that employs UCA at the receiver front is presented by utilizing the developed channel model.

I. INTRODUCTION

Multiple input multiple output (MIMO) technology offers a spatial diversity that can be utilized to achieve significant capacity gain as well as improve system performance [1]. Most of the studies for the design and performance evaluation of MIMO wireless communication systems use simplified statistical channel models that are idealized abstractions of temporal and spatial correlations [2-3]. The main limitation of these channel models is that realistic channel conditions are not included as they provide simple and intuitive relations to physical directions and propagation environments. Various measurements show that realistic MIMO channels provide different capacity values [4-5]. Therefore, developing accurate and realistic correlated channels is essential and of crucial importance to predict an accurate performance of MIMO systems. Some realistic models are proposed as standardized channel models were unified and agreed on by many scientific parties worldwide to be used in the development of modern MIMO systems. The most commonly used standard spatial channel models for system level simulations are the 3GPP/3GPP2 SCM (spatial channel model) [6] for outdoor cellular wide area scenarios and the Technical Group of IEEE 802.11 TGn channel model [7] for indoor WLAN short range scenarios. The two models assume that transmitter and receiver MIMO antennas are restricted to uniform linear arrays (ULAs). However, recently there has been increased interest in using uniform circular arrays (UCAs) [8-14], which is perhaps the next most common array geometries for future generation WLANs

due to their enhanced azimuth coverage. Therefore, in this paper, we extend our work in [14] and develop a more realistic spatially and temporally clustered channel model to be applied in the simulation of UCA-MIMO systems for WLANs. The proposed model accounts for six different actual propagation scenarios that are applied in IEEE802.11 TGn channel model. Numerical simulation examples are performed for different case studies to investigate system capacity and BER performance of the pre-set realistic scenarios. The rest of the paper is organized as follows. Section 2 describes the developed channel model and the modifications proposed to the existing IEEE802.11n standard model to include UCA configurations. Section 3 provides the temporal properties of the clustered MIMO channel models. In section 4 numerical results are discussed and a thorough discussion about the applicability of the developed model is presented. Finally, conclusions are given in section 5.

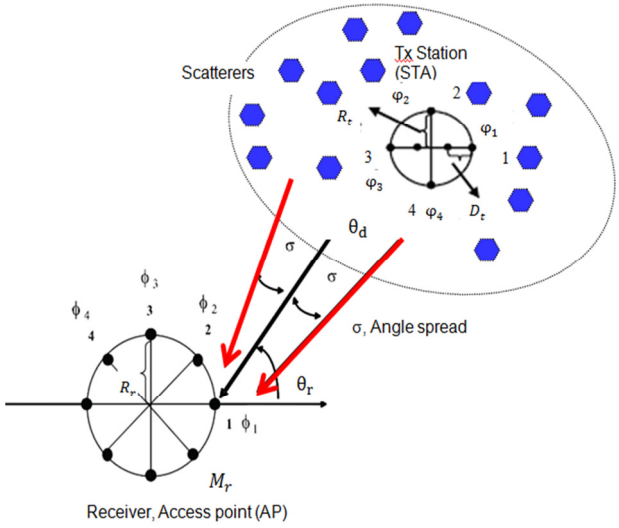

Fig. 1. MIMO communication system employing ($M_t \times M_r$) ULA / UCA configurations.

II. MODIFIED SPATIAL CHANNEL MODELS

Considering an uplink of IEEE802.11*n* MIMO WLAN communication system operating in an indoor environment, where the transmitter is a wireless station (STA) and the receiver is an access point (AP). Figure 1 shows ($M_t \times M_r$) MIMO WLAN system with M_t -element transmit-antenna array at STA and M_r -element receive-antenna array at AP end. We consider the arrays at STA and AP to be either ULA with inter-element spacing D_t and D_r or UCA of radius R_t and R_r , respectively. The figure also shows a graphical representation of the clustered channel model where the angle that each *i*-th element location makes with the horizontal axis is denoted as φ_i and ϕ_i for transmitter and the receiver. The central angle of departure (AoD) and the central angle of arrival (AoA) are θ_d and θ_r, respectively. Additionally, it is assumed that the channel is composed of several moving scatterers which are local to STA. Thus, the received signal is the sum of multiple plane waves with random phases. Under this assumption, the channel consists of multiple sample taps, which are associated with different clusters. The discrete-time impulse response of MIMO channel matrix can be written as in [7]:

$$\mathbf{H}(t) = \sum_{l=1}^{L-1} \mathbf{H}_l(t)\delta(\mathrm{t} - \tau_l)\,, \qquad (1)$$

where t denotes the discrete time index, L is the number of effectively nonzero channel taps (corresponding to the channel clusters), $\mathbf{H}_l(t)$ is the $M_t \times M_r$ channel matrix for the l-th tap, $\delta(\mathrm{t} - \tau_l)$ is the Kronecker delta function for τ_l delay at l-th tap. For simplicity, notation t will be omitted in the following equations. The l-th matrix tap $\mathbf{H}_l$ at one instance of time can be written as the sum of a constant line of sight (LOS) matrix and a variable Rayleigh non line of sight (NLOS) matrix

$$\mathbf{H}_l = \sqrt{\mathrm{p}_l}\left\{\sqrt{\frac{\mathrm{K}_l}{\mathrm{K}_l+1}}\left[\mathrm{e}^{\mathrm{j}2\pi\left(\frac{v_0}{\lambda}\right)t\cos\left(\frac{\pi}{4}\right)}.\mathbf{S}\right] + \sqrt{\frac{1}{\mathrm{K}_l+1}}\left(\mathbf{R}_{\mathbf{spatial}}.\mathbf{B}\right)\right\}, \qquad (2)$$

where the first term represents $\mathbf{H}_l^{LOS}$ and the second accounts for $\mathbf{H}_l^{NLOS}$, p_l is the total power of l-th channel tap that is the sum of the fixed LOS power and the variable NLOS power of the l-th tap defined in the power delay profiles, K_l is the Rician K-factor of l-th tap that represents the relative strength of the LOS component, $\mathbf{S}$ is the steering matrix, $\mathbf{R}_{spatial}$ is spatial fading correlation shaping matrix, $\mathbf{B}$ is a vector that is

obtained by passing $\mathbf{H}_{iid}$ independent complex Gaussian random samples with zero mean and unit variance through a filter that is shaped based on the Doppler model where the transmitter and receiver are stationary and the surrounding objects and people are moving, the exponential term is used to account for the phase change introduced in the LOS path due to the movement of scattering objects with velocity v_o that is assumed to be fixed at 1.2 kmph. The model is adopted to include UCA configurations at both STA and AP ends by defining the steering vector used in (2) as

$$\mathbf{S}=\begin{pmatrix} e^{j2\pi\left(\frac{R_t}{\lambda}\right)\sin(\zeta)\cos(\theta d-\varphi_1)} \\ \vdots \\ e^{j2\pi\left(\frac{R_t}{\lambda}\right)\sin(\zeta)\cos(\theta d-\varphi_{Mt})} \end{pmatrix}^{T} \cdot \begin{pmatrix} e^{j2\pi\left(\frac{R_r}{\lambda}\right)\sin(\zeta)\cos(\theta r-\phi_1)} \\ \vdots \\ e^{j2\pi\left(\frac{R_r}{\lambda}\right)\sin(\zeta)\cos(\theta r-\phi_{Mr})} \end{pmatrix}, \quad (3)$$

where λ is the signal wavelength, ζ is the elevation angle. For simplicity, only azimuth angles are considered in the propagation geometry (i.e., $\zeta = 90^o$), however the results can be generalized to three dimensions by changing the value of ζ. Note that, the extra distance that the signal has to travel from adjacent antenna elements at the transmitter end is $R_t\cos(\theta - \varphi_i)$ that results in a phase difference of $(2\pi\frac{R_t}{\lambda})\cos(\theta - \varphi_i)$. A similar phase shift term is included at the receiver. It should be noted that the AoA and AoD for the LOS path of the channel are assumed to be fixed at 45 degrees. According to [8] and [14], the correlation between *m*-th and *n*-th element in

$$R(m,n) = \int_{-\pi}^{\pi} e^{j(\varphi_m-\varphi_n)} P_\theta(\theta)\, d\theta, \quad (4)$$

where $P_\theta(\theta)$ is the power azimuth spectrum (PAS) distribution that has a truncated Laplacian shape, θ is either θ_d or θ_r the central random variable for AoD or AoA, where $R(m,n)$ is the complex correlation coefficients between the *m*-th and *n*-th antennas. Thus, the complex spatial correlation matrix $\boldsymbol{R}_{rx}$ at the receiver end with UCA configuration is obtained by numerically performing the integral in (4) as in [8]

$$Re\{R_{rx}(m,n)) = J_o(Z_c) + 2\sum_{k=1}^{\infty}\frac{a^2(1-e^{-a\pi})}{a^2+4k^2}J_{2k}(Z_c)\cos[2k(\theta_r+\alpha)], \quad (5)$$

$$Im\{R_{rx}(m,n)) = \frac{2a}{(1-e^{-a\pi})}\sum_{k=0}^{\infty}\frac{a(1-e^{-a\pi})}{a^2+(2k+1)^2}\cdot J_{2k+1}(Z_c)\sin[(2k+1)(\theta_r+\alpha)], \quad (6)$$

where a is a decay factor which is related to the angle spread, when a increases the angle spread decreases, α is the relative angle between the *m*-th and *n*-th antenna elements, Z_c is related to the antenna spacing and is defined as follows

$$Z_c = \sqrt{(2\pi\left(\frac{R_r}{\lambda}\right)\{[\cos\varphi_m - \cos\varphi_n]^2 + [\sin\varphi_m - \sin\varphi_n]^2\}}. \quad (7)$$

A similar expression can be obtained for $\boldsymbol{R}_{tx}$ coefficients as in (5) and (6) by replacing θ_r, R_r, φ_m, φ_n with θ_d, R_t, ϕ_m, ϕ_n respectively.

III. TEMPORAL PROPERTIES OF CHANNEL MODEL

In the temporal domain, the properties of the proposed MIMO channel models for systems employing UCA configurations are assumed to be similar to the clustered model that was first introduced by Saleh and Valenzuela in [2]. The model is based on assuming that the received signal comprises of multiple decayed rays (clusters) that were reflected from different groups of scatterers. The received signal is assumed to be a summation of different exponential functions in time. For the given assumptions, the impulse response of the channel can be expressed as:

$$h(t) = \sum_{l=0}^{\infty}\sum_{k=0}^{\infty} a_{kl}\delta(t - T_l - \tau_{kl}), \quad (8)$$

where T_l is the arrival time of the first ray of *l*-th cluster. τ_{kl} is the arrival time of the *k*–th ray within the *l*-th cluster. a_{kl} is the amplitude of each arriving ray, which is a Rayleigh distributed random variable with mean square value equal to

$$\overline{a_{kl}^2} = \overline{a^2(T_l,\tau_{kl})} = \overline{a^2(0,0)}\, e^{-T_l/\Gamma}\, e^{-\tau_{kl}/\gamma}, \quad (9)$$

where $a^2(0,0)$ is the average power of the first ray of the first cluster and depends on the distance between the transmitter and receiver, Γ is the cluster power decay time constant and γ is the ray

power decay time constant within a cluster. For the developed model, the clusters and taps exponential decays are not used, instead values for the power delay profiles that will be used throughout the paper are defined as in [7] for standard IEEE 802.11*n* channel models as shown in Table 1.

Table 1: IEEE802.11n TGn channel models [7]

Model	Environment	K (dB) LOS/NLOS	Delay (rms)	Clusters
A	Flat fading	0/-∞	0	1
B	Residential	0/-∞	15	2
C	Residential/ small office	0/-∞	30	2
D	Typical Office	3/-∞	50	3
E	Large Office	6/-∞	100	4
F	Large Space, In-/out-door	6/-∞	150	6

The system capacity is defined as the maximum possible transmission rate such that the probability of error is arbitrarily small. By applying the singular value decomposition (SVD) theorem, the ergodic capacity (C) in the case of the uniform power scheme is given by

$$C = E\left\{W\sum_{i=1}^{r}\log_2\left[1+\frac{P_i\lambda_i}{\sigma^2}\right]\right\}, \qquad (10)$$

where E{.} Is the expectation operator, r is the rank of the $M_t \times M_r$ channel matrix **H**, where W is the bandwidth of each sub-channel, P_i is the received signal power in the i-th sub-channel that is equal to P/M_t , P is the total power, λ_i is the eigenvalue of the sub-channels, $\sigma^2{}_n$ is the noise power. In this case, the power is equally divided among the transmit antennas. However, when applying the water-filling (WF) power scheme that is the optimal energy allocation algorithm [1]. The power values P_i are assigned on the basis that the better the sub-channel gets, the more power is injected into it and the ergodic capacity in this case will be

$$C = E\left\{W\sum_{i=1}^{r}\log_2\left[1+\frac{\lambda_i}{\sigma^2}(\mu-\frac{\sigma^2}{\lambda_i})^+\right]\right\}, \qquad (11)$$

where a^+ denotes max$(a, 0)$, $i = 1, 2, \ldots, r$ and μ is determined so that $\sum_{i=1}^{r} P_i = P$.

IV. NUMERICAL RESULTS AND ANALYSIS

In this section, we study and compare the channel capacity and system performance of UCA-MIMO WLAN systems using the numerically developed realistic channel model. Unless specified, the MIMO system (4×4) are considered, both ends utilize the UCA configuration with radius 0.5 or 0.75 wavelength spacing. 10000 channel realizations and NLOS scenario with SNR=10 dB are considered. If ULA configuration is being used then the inter-elements spacing is considered to be 0.5λ. The six standard *TGn* channel model profiles (A-F) defined in [7] are used here to realize realistic scenarios throughout the following simulation study cases. Figure 2 shows probability density function (*pdf*) of the AoA for model 'F' and shows how the power is distributed among the taps and the clusters. The model has 5 overlapping clusters with 18 taps. All taps *pdf* are considered as truncated laplacian functions [7].

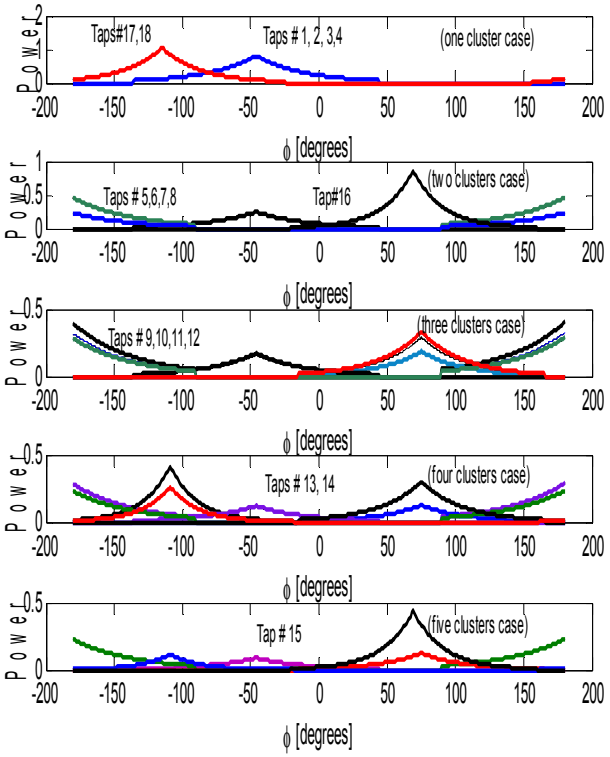

Fig. 2. *pdf* of the AoA for the taps in model 'F'.

Figure 3 illustrates the channel spatial correlation R_s (21, 11) between the links h_{11} and h_{21} for all taps of model 'F' versus the UCA radius

in the receiver. It is obvious that the spatial correlation decreases as UCA antenna radius increases. In addition, one can see that the spatial correlation differs for various taps depending on AoA and the angular spread (AS) of each tap. Figure 4 plots the cumulative distribution function (*cdf)* of the eigenvalues of channel models 'A', 'B', and 'F' for 4×4 MIMO UCA based system. It is known that the steeper slope the *cdf* curve has the less amplitude of the fluctuation in the signal, i.e., the fades due to the multipath are less deep, and therefore a higher degree of diversity is obtained.

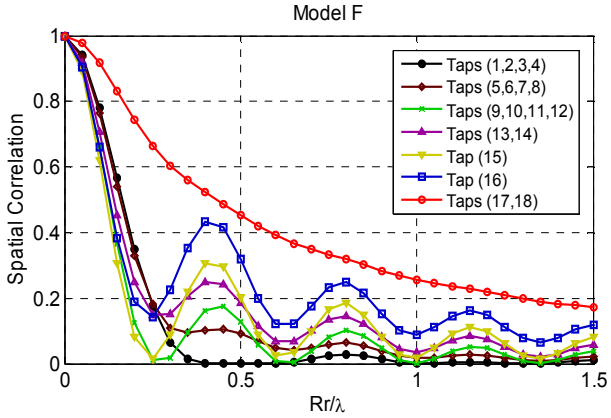

Fig. 3. $R_s(21,11)$ for different taps of model 'F' versus UCA radius in the receiver.

Figure 4 illustrates the impact of each sub-channel, identified in, upon the total capacity available for different channel models. As can be seen, the largest eigenvalue characteristic (λ_1) is nearly the same for most of the channel models. However, the difference increases between models 'A', 'B' and 'F' is more distinguished for 2nd, 3rd, and 4th eigenvalues, respectively. According to (10), the higher summation of eigenvalues the higher capacity, thus as shown in the Fig. model 'F' has the highest summation of eignvalues that leads to the highest capacity. This result was expected due to the high number of clusters and multi-paths components that are included in model 'F' compared to other models.

The capacity dependence on the azimuth rotating of the receiver configuration (orientation of AP) with respect to different channel models is studied. The rotation is measured by the orientation angle (θ_r) shown in Fig.1 with respect to a reference angle ϕ_1 that is used as a reference for the prescribed AoAs defined by the *TGn* models. Two cases are considered: case (1): 4×4 UCA×UCA based system radii R_t, R_r=0.75λ and case (2): 4×4 ULA×ULA Based system with inter-element distance d_t=0.5λ. To have fair comparison these dimensions are assumed to have identical largest array dimension equal to 1.5λ for both cases. The results are demonstrated in Fig. 5. The presented results reveal that the ergodic capacity in general is more affected by the orientation angle in the ULA unlike in the UCA. This effect gives a privilege to the use of the UCA receiver. Also, as can be observed that the mean capacity for different models (A, B, C, and F) and configurations (ULA and UCA) is compared to the mean 4x4 (i.i.d) MIMO capacity. The independent and identically distributed (i.i.d) case is considered for uncorrelated channel case where channel matrix elements is modeled as i.i.d. zero-mean unit-variance complex Gaussian random variables. Capacity for this case is found to be =10.823 b/s/Hz. As expected for Model 'A' ULA configuration, since the Model A has only one tap one cluster at AoA=45°, then by rotating the ULA by 45° the signal will impinge the array from the endfire direction. In this case the correlation will be highest and the capacity will be minimum. In contrary, if the ULA is rotated by 135° we get the maximum capacity because in this case signal arrives at the broadside of the array. Also it can be observed that the capacity of model F is almost constant and it has the highest values for both configurations. Model B for ULA has the lowest throughput values. UCA case the mean capacity is approximately between a minimum of 77% of the mean 4x4 i.i.d. MIMO capacity (for model C at angle 135°) and a maximum of 96% of the mean 4x4 i.i.d. MIMO capacity (for model F at angle 67.5°). However, the ULA case, the mean capacity is approximately between a minimum of 62% of the mean 4x4 i.i.d. MIMO capacity (for model B at angle 157.5°) and a maximum of 95% of the mean 4x4 i.i.d. MIMO capacity (for model F at angle 90). Here, it can be concluded that, the variations range of ergodic capacity for UCA-MIMO configuration over various orientations and different channel conditions is higher than that for ULA-MIMO configuration under the same orientations and channel conditions.

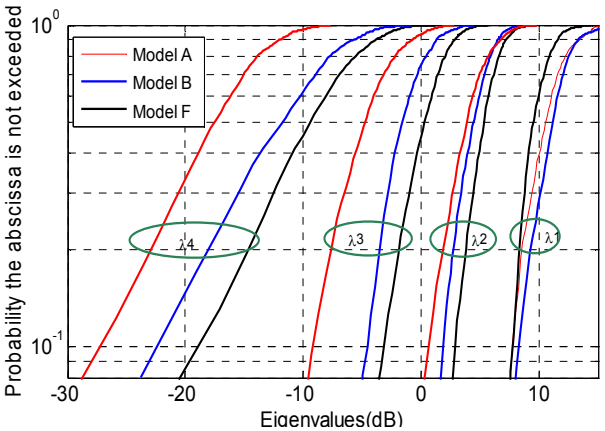

Fig. 4. Channel singular values CDFs of models A, B, and F for 4×4 MIMO UCA based system.

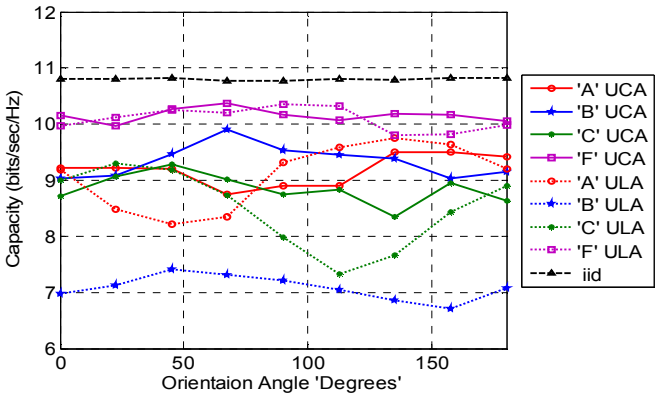

Fig. 5. Ergodic capacity versus azimuth orientation angle at receiver side cases 1 and 2, NLOS conditions.

Figure 6 presents the ergodic capacity versus UCA radius for channel models 'A', 'B', and 'F. For each model, the capacity is investigated at M_r = 2, 4, and 8. The capacity of model 'F' has the highest value for all cases because of the 18 taps and 6 clusters arriving to the UCA array from different AoAs. One tap, one cluster model 'A' found to be the lower bound for all cases. As can be seen, for 'A', 'B', and 'F' models, the values of mean capacity are, respectively, 5.4, 5.75, and 5.9 (for M_r = 2) and 12.14, 12.95, and 15.13 (for M_r= 8). These results show that as M_r increases, the capacity values are more affected by the model selection. This indicates that, the environment profiles should be carefully modeled and selected whenever capacity investigations are performed in particular for higher order MIMO.

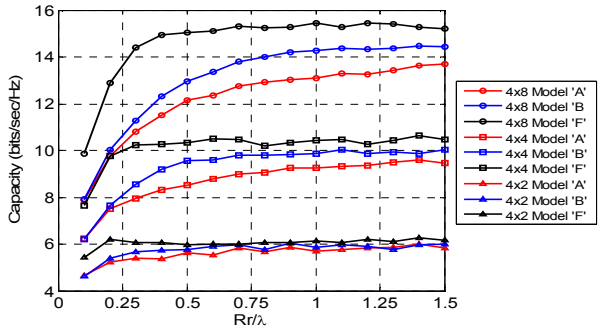

Fig. 6. Ergodic capacity versus radius of channel models 'A', 'B', and 'F' for M_t=4, M_r=2, 4, 8 and SNR=10 dB.

Next, LOS conditions for UCA based MIMO systems are examined by assuming that the LOS component will be included if the separation between the transmitter mobile unit and the receiver AP are within breakpoint distance. The LOS is configured by adding a standard K-factor reported in [7] to the first tap while all the other taps K-factor remain at -∞ dB as in IEEE802.11*n* model. The LOS component of the first tap is added on top of the NLOS component so that the total energy of the first tap for the LOS channels becomes higher than the value defined in the power delay profiles (PDP). Figure 7 shows the capacity CDFs for a 4x4 UCA based MIMO under A, B, and F channel scenarios for both LOS and NLOS cases. As noticed from the figure, the LOS component degrades the capacity of the system working in all channel scenarios. It is found that in NLOS conditions, capacity improves by 20% compared to the case where the LOS component included. The improvement is less pronounced for model F than other models due to its many multipath taps thus the effect of the 1st LOS tap will be less significant.

Capacity results for the UCA based MIMO systems that apply the water-filling (WF) scheme under different channel conditions are shown in Figs. 8 and 9. In the WF scheme, the power allocated to each sub-channel is optimized to maximize the system capacity. Figure 8 shows ergodic capacities versus SNR for channel models 'A', 'B', 'C', and 'F' for 4x4 UCA based MIMO system. Identical with the results of i.i.d uncorrelated channel model [1], the capacity delivered by the WF power allocation scheme is superior to the one achieved with uniform power specifically for low SNRs. As shown, the capacity

increase by applying the WF scheme is found to be in 'A' and 'C' models more than that for 'B' and 'F' models. Figure 9 shows the capacity versus the number of elements of the UCA (M_r) at the receiver for 4×M_r MIMO system both uniform and WF schemes values when varying the channel models. As seen, when the number of receiver elements is greater than 3 the capacity becomes more dependent on the environment profiles. It is noticed that in general as the number of received antennas increases the capacity increases for the uniform scheme. However, for models 'A' and 'C' the WF algorithm gets its best performance at M_r = 4 and in general when the numbers of antennas at the transmitter and at the receiver are equal, i.e. the channel matrix is full rank.

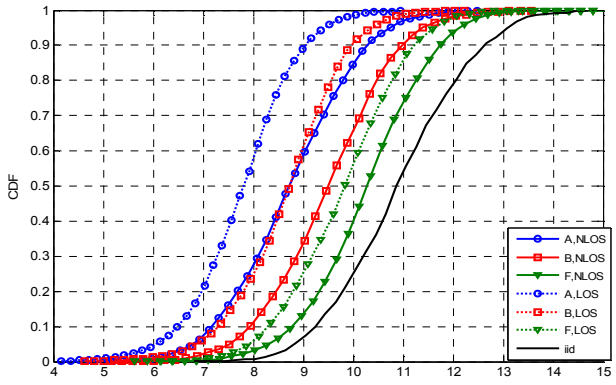

Fig. 7. Cumulative distribution functions (CDFs) of capacity for models 4x4 UCA based MIMO in 'A', 'B', and 'F' channel models with and LOS and NLOS conditions.

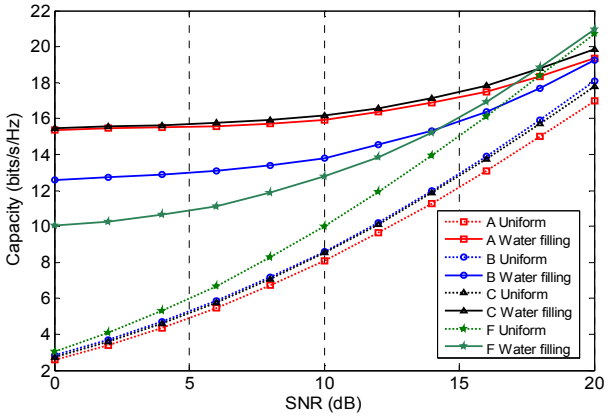

Fig. 8. Ergodic capacity versus SNR of channel models 'A', 'B', 'C', and 'F' for 4x4 UCA-MIMO.

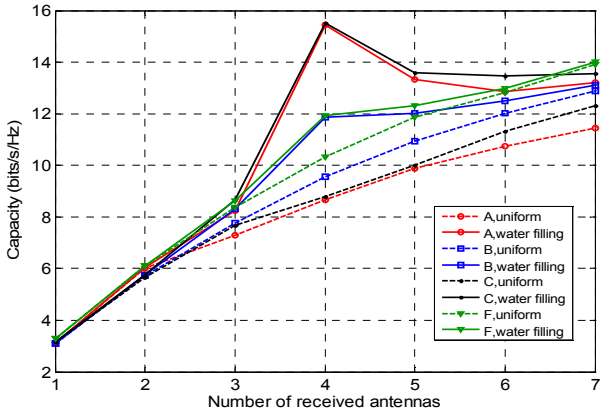

Fig. 9. Ergodic capacities of channels 'A', 'B', 'C', and 'F' versus the number of received antennas, for 4xM_r UCA based system with uniform and water-filling power schemes.

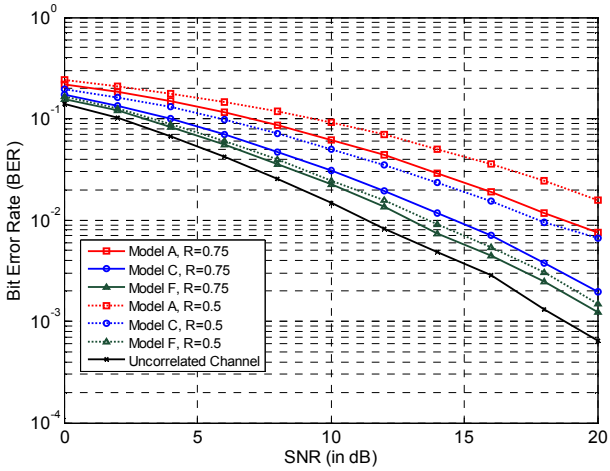

Fig. 10. BER performance of VBLAST MIMO system for three models 'A', 'C' and 'F' compared to uncorrelated channel model with BPSK and various 4x4 UCA radii.

Finally, the diversity gain measured by bit error rate (BER) performance is examined for WLAN 802.11*n* system utilizing minimum mean squares estimation- VBLAST (MMSE-VBLAST) system [15] with UCA configurations. Two radii R=0.5λ and 0.75λ are considered at the AP receiver. Figure 10 illustrates a comparison of BER performance curves under different *TGn* models. Corresponding BER of an i.i.d. channel (uncorrelated fading channel) is also included for comparison. As can be seen that the link has its best performance for Model 'F' conditions, in this case it is the nearest performance curve to the

uncorrelated fading channel '*i.i.d*' curve. Model 'F' performance curve is followed by model 'B' then model 'A' with the lowest performance. Also, as expected that the link performance improves as the radius of the UCA at the AP end increases from 0.5λ to 0.75λ. In general, the results show that the BER performance of uniform circular diversity array depends on the main AoA.

V. CONCLUSION

In this paper, a modification to IEEE 802.11*n* channel model has been proposed to consider the application of using the UCA configurations in MIMO WLAN systems. Realistic spatio-temporal channel model has been developed and includes spatial fading correlation for six different environment profiles. Each profile is distinguished by its predefined parameters such as number of clusters, number of taps within each cluster, power delay profile of the taps, and angle of incidence of each tap. The impact of the selection of realistic channel profile on the eignvalue of each sub-channel and the total system capacity values has been studied. The capacity dependence on the used ULA or UCA geometries and their orientations at both ends of the MIMO system has been studied and compared. It has been found that, the variation range of ergodic capacity for UCA-MIMO configuration over various orientations and different channel conditions is higher than that for ULA-MIMO configuration under the same orientations and channel conditions. The influence of the LOS component on the link performance was presented for UCA based systems and it is shown that LOS component existence is not preferable for MIMO systems. The improvement is less pronounced for large space model F environments. Both uniform and none uniform WF power allocation schemes have been simulated for UCA based systems and it can be said that the WF relocation power scheme is best applied for MIMO UCA based systems working in residential models A and C environments. Moreover, VBLAST system BER performance has been investigated under different channel scenarios and the results show that its best conditions for having the best UCA-MIMO system performance are model F conditions. Finally, the realistic channel model that is introduced in this paper could be effectively utilized to provide an accurate capacity and system performance analysis for the next generation WLANs.

REFERENCES

[1] M. Jankiraman, "Space-Time Codes and MIMO Systems", Artech House Publishers, Boston, London.

[2] A. Saleh and R. Valenzuela, "A Statistical Model for Indoor Multipath Propagation," *IEEE J. Sel. Areas Comm*., vol. 5, no. 2, pp.128–137, Feb. 1987.

[3] Q. Spencer, M. Rice, B. Jeffs, and M. Jensen, "A Statistical Model for Angle of Arrival in Indoor Multipath Propagation," *Proc. IEEE Veh. Technol. Conf.*, vol. 3, pp. 1415–1419, May 1997.

[4] L. Schumacher, K. I. Pedersen, and P. E. Mogensen, "From Antenna Spacings to Theoretical Capacities - Guidelines for simulating MIMO systems," *Proc. PIMRC Conf.*, vol. 2, pp. 587-592, Sep. 2002.

[5] J. P. Kermoal, L. Schmacher, P. Mogensen, and K. I. Pederson, "Experimental Investigation of Correlation Properties of MIMO Radio Channels for Indoor Picocell Scenarios*", in proc. IEEE Vehicular Technology conference*, Boston, USA, vol. 1, pp. 14-21, Sept. 2000.

[6] 3GPP, "Spatial Channel Model for MIMO Simulations," TR25.996 V6.1.0, Sep. 2003.

[7] IEEE P802.11 Wireless LANs, "TGn Channel Models," *IEEE* 802.11-03/940r4, 2004-05-10.

[8] J. Tsai, R. M. Buehrer, and B. D. Woerner, "Spatial Fading Correlation Function of Circular Antenna Arrays with Laplacian Energy Distribution," *IEEE Comms. Letters*, vol. 6, no. 5, pp.178-180, May 2002.

[9] L. Xin and Z.-P. Nie, "Spatial Fading Correlation of Circular Antenna Arrays with Laplacian PAS in MIMO Channels," *International Symposium of IEEE Antennas and Propagation Society*, vol. 4, pp. 3697–3700, 2004.

[10] A. Forenza, D. J. Love, and R. W. Heath, "Simplified Spatial Correlation Models for Clustered MIMO Channels with Different Array Configurations," *IEEE Transactions*

on Vehicular Technology, vol. 56, no. 4, pp. 1924-1934, July 2007.

[11] Dantona, V., Schwarz, R.T., Knopp, A., Lankl, B., "Uniform Circular Arrays: The Key to Optimum Channel Capacity in Mobile MIMO Satellite Links," *5th Advanced satellite multimedia systems conference*, pp. 421-428, 13-15 Sept. 2010.

[12] Suzuki, H., Hayman, D.B., Pathikulangara, J., Collings, I.B., Zhuo Chen, and Kendall, R., "Design Criteria of Uniform Circular Array for Multi-User MIMO in Rural Areas," *IEEE Wireless Communications and Networking Conference*, pp. 1-6, April 18-21 2010.

[13] Bu Hong Wang and Hon Tat Hui, "Investigation on the FFT-Based Antenna Selection for Compact Uniform Circular Arrays in Correlated MIMO Channels," *IEEE Transactions on Signal Processing*, vol. 59, no. 2, pp. 739-746, Feb. 2011.

[14] M. A. Mangoud "Capacity Investigations of MIMO Systems in Correlated Rician Fading Channel Using Statistical Multi-Clustered Modeling," *Applied Computational Electromagnetics Society (ACES) Journal*, vol. 25, no. 2, 2010.

[15] D. Chizhik, et. al., "Effect of Antenna Separation on the Capacity of BLAST in Correlated Channels," *IEEE Comm. Lett.*, vol. 4, pp. 337–339, Nov. 2000.

Local Residual Error Estimators for the Method of Moments Solution of Electromagnetic Integral Equations

Usman Saeed and Andrew F. Peterson

School of Electrical and Computer Engineering
Georgia Institute of Technology
Atlanta, GA, 30332-0250, USA
Email: usaeed@gatech.edu, peterson@ece.gatech.edu

Abstract ─ Several methods for estimating the local (cell-by-cell) error associated with a method of moments solution of the electric field integral equation are investigated. Three different residual error estimators are used with a variety of prototype structures. The global error estimates show reasonable correlation with the actual current density errors, and all three local error estimators correctly identify the high-error regions. Utility of the proposed error estimators is presented through a simple *h*-refinement technique.

Index Terms ─ Adaptive refinement, boundary element method, method of moments, residual error.

I. INTRODUCTION

Electromagnetic field problems often involve the prediction of fields in the presence of complicated structures, and the solution of these problems usually rests upon computational procedures. Integral equation formulations have been widespread, and are discussed in several texts [1-3]. The typical numerical solution process involves creating a subsectional mesh model for the surface of any structures, representing the equivalent surface currents on that surface by a piecewise-polynomial basis, and imposing boundary conditions on the fields to construct a large linear system of equations. The solution of that system produces the coefficients of those polynomial basis functions. That process is known as the *method of moments* or the *boundary element method*. Although the numerical treatment of integral equations has steadily advanced for decades, adaptive refinement procedures have lagged behind other developments. Adaptive refinement is an approach where either (a) the mesh density, or (b) the polynomial degree employed in certain regions of the mesh, is automatically modified as required to improve the accuracy of the approach, without user intervention. Such modification must be based on an estimate of the local error [4-11].

In the present study, we consider the transverse-electric (TE)-to-*z* electric field integral equation (EFIE) for two-dimensional conducting structures. The continuous equation being solved can be expressed as

$$\bar{L}\left\{\bar{J}\right\}_{\tan} = \bar{g}_{\tan}, \tag{1}$$

where $\bar{J}$, the electric current density, is the quantity of interest, and

$$\bar{L}\left\{\bar{J}\right\} = \frac{1}{j\omega\varepsilon}\left\{\nabla\nabla\bullet + k^2\right\} \int \bar{J}(t')\frac{1}{4j}H_0^{(2)}(k\left|\bar{r}-\bar{r}'\right|)dt', \tag{2}$$

$$\bar{g} = -\bar{E}^{inc}(\bar{r}), \tag{3}$$

where $\bar{E}^{inc}$ is the given excitation, $H_0^{(2)}$ is the zero-order Hankel function of the second kind, t and t' denote parametric variables along the contour of the structure, and $\bar{r}$ is the position vector from t' to t on the contour.

The numerical solution for the current density is obtained in terms of a representation in N basis functions

$$\bar{J}_N(t) = \sum_{n=1}^{N} J_n \bar{B}_n(t) . \quad (4)$$

The surface of the conducting scatterer is represented by flat facets, while the current density is represented by an expansion using piecewise-linear or "triangle" basis functions $\{\bar{B}_n(t)\}$ that are tangential to the surface. Each triangle function straddles two of the facets in the surface model. A weighted-residual approach is employed using piecewise-constant or pulse testing functions $\{\bar{T}_m(t)\}$, also tangential to the surface and partially straddling adjacent cells, to construct a system of equations that may be expressed in matrix form as

$$\mathrm{ZJ} = \mathrm{E} . \quad (5)$$

The entries of the N by N system matrix and the N by 1 excitation vector are given by

$$Z_{mn} = \int \bar{T}_m \bullet \bar{L} \left\{ \bar{B}_n \right\} dt , \quad (6)$$

$$E_m = \int \bar{T}_m \bullet \bar{g} \; dt . \quad (7)$$

Other details of the numerical solution procedure, including approximations that were used in the computation of Z_{mn}, are described in section 2.4 of [3].

Local error estimators are often based on residual error computations. Once the coefficients in (2) have been determined, the tangential residual associated with this numerical result can be written as

$$R_{\tan}(t) = \bar{L} \left\{ \bar{J}_N \right\}_{\tan} - \bar{g}_{\tan} . \quad (8)$$

The residual error is known to correlate with the actual error $\bar{e} = \bar{J} - \bar{J}_N$ [12], and has formed the basis for determining solution error in various integral equation formulations [13-14]. However, it is relatively expensive to compute, since it usually must be evaluated using an approach that is independent from that used to construct the original linear system.

In the following, we consider several different error estimators related to (8), and compare their performance and computational efficiency on a number of canonical scattering targets.

II. TANGENTIAL RESIDUAL ERROR ESTIMATOR

The TE EFIE imposes the tangential-field boundary condition

$$E^{tot}_{\tan} = 0 , \quad (9)$$

indirectly, by equating the average value of the residual in (8) over the domain of the testing function to zero. In other words, in the construction of the linear system in (5), equation (9) is imposed in an average sense by integrating it with a piecewise-constant testing function from the center of one cell to the center of the adjacent cell. In the preceding notation, this is equivalent to imposing

$$\int R_{\tan}(t) dt = 0 , \quad (10)$$

over the domain of each pulse testing function.

The residual in (10) provides a means to measure the error in a particular result, and is directly computable since it does not depend directly on the exact solution. However, if we compute the residual error in the same manner as was used to construct the linear system in (5), we do not obtain useful information since the equations are exactly satisfied. However, we could re-compute the residual error in a variety of ways to obtain an independent measure of the residual error.

Consider the use of weighting functions that are centered within each cell with their widths made relatively small (1/5 of the cell width in this case). In that case, the residual error at the center of cell i may be obtained as

$$R_t(t_i) = \int_{\textit{small domain at center of cell } i} R_{\tan}(t) dt , \quad (11)$$

where $R_{\tan}$ is computed from the previously-obtained numerical values for the current density, using essentially the same subroutines as used to compute the matrix entries Z_{mn}.

The normalized tangential residual error in the i^{th} cell may be defined as

$$TR_i^{loc} = \frac{|R_t(t_i)|}{|\bar{g}|_{\max}} , \quad (12)$$

to provide a local measure of the error. In (12), $|\bar{g}|_{\max}$ denotes the maximum magnitude of the excitation (3) used in the residual calculation of (11). For a global measure of the error, we employ the 2-norm error obtained by summing (12) over all the cells in the model:

$$TR_2^{glo} = \sqrt{\frac{1}{N} \sum_{i=1}^{N} (TR_i^{loc})^2} . \quad (13)$$

As a consequence of the definition of the residual in (11), these error measures are relatively independent of the system of equations that led to the specific numerical solution being evaluated.

III. NORMAL RESIDUAL ERROR ESTIMATOR

In the preceding section, a residual error estimator was constructed based on enforcing the tangential field boundary condition. An additional boundary condition should be satisfied by the normal component of the total electric field at the surface of a perfect conductor, namely

$$\hat{n} \bullet \bar{E}^{tot} = \frac{\rho_s}{\varepsilon}, \tag{14}$$

where ρ_S denotes the surface charge density at a point on the surface, ε denotes the permittivity of the exterior medium, and $\hat{n}$ is an outward-directed unit vector perpendicular to the surface. The boundary condition of (14) may be expressed in the form of an alternative residual

$$N(t) = \hat{n}(t) \bullet \left(\bar{L}\left\{ \bar{J}_N \right\} - \bar{g} \right) + \frac{1}{j\omega\varepsilon} \frac{d\{\hat{t}(t) \bullet \bar{J}_N\}}{dt}, \tag{15}$$

which uses

$$\rho_s = -\frac{\nabla_S \bullet \bar{J}_N}{j\omega} = -\frac{1}{j\omega} \frac{d\{\hat{t}(t) \bullet \bar{J}_N\}}{dt}. \tag{16}$$

For ease of computation and employing the same subroutines used to build the matrix in (5), we orient the testing functions so that they are now normal to the cells, at the cell center, and compute the normal residual in the i^{th} cell using

$$NR_i^{loc} = \frac{1}{|\bar{g}|_{\max}} \int_{perpendicular\ to\ cell\ i} N(t) dn, \tag{17}$$

where the testing domain is typically on the order of the cell size, and $|\bar{g}|_{\max}$ denotes the maximum magnitude of the excitation used in the residual calculation of (15). The global error NR_2^{glo} is obtained in the same manner as equation (13).

IV. ERROR ESTIMATION BASED ON AN OVER-DETERMINED SYSTEM OF EQUATIONS

A third way to compute a residual is to set up and solve an overdetermined system of equations representing (1), by employing more testing functions (over smaller domains) than basis functions when constructing equation (5) [13-15]. A least-squares approach can be used to obtain a solution that minimizes the error in the residual equations. Since the equations will not be exactly satisfied, the residual can be computed from the equations and used directly as a measure of the error in the numerical result [14].

We use an implementation where the cells are divided in half, each with a tangential testing function centrally located, to yield a $2N$ by N system

$$\mathbf{Z}_{2N\times N}\mathbf{J}_N = \mathbf{E}_{2N}. \tag{18}$$

Unlike [13], these equations are equally weighted. After the current coefficients are determined by a least-square solution, the residual function is computed as the matrix column vector

$$R_{OD}(t_i) = Z_{2N\times N} J_N - E_{2N}^{inc}. \tag{19}$$

The normalized tangential residual error at location i may be defined as

$$ODR_i^{loc} = \frac{|R_{OD}(t_i)|}{\left|E_{2N}^{inc}\right|_{\max}}. \tag{20}$$

A global function is obtained by summing over the 2N locations in accordance with (13). We note that one could alternatively mix tangential and normal testing functions.

V. SIMULATION RESULTS

In the following, we compare the performance of the preceding three error estimators on several geometries. We also estimate the actual error in each numerical result by comparison to a numerical result obtained with a finer discretization of the target. A local value for the normalized error in the i-th cell is obtained as

$$NE_i^{loc} = \frac{\left|\bar{J}_{ref}(t_i) - \bar{J}_N(t_i)\right|}{\max\left|\bar{J}_{ref}(t_i)\right|}, \tag{21}$$

with the global estimate obtained following (13).

Figure 1a shows the geometry of the first problem, which is a circular cylinder of 5λ circumference illuminated with two line sources placed (as shown) a distance of 0.1λ from the cylinder surface. For one of the line sources, the expression used for the incident E-field is given by

$$\overline{E^{inc}} = j\eta 2\pi H_1^{(2)}(k\rho)\left[\hat{x}\frac{y-y'}{\rho} - \hat{y}\frac{x-\hat{x}}{\rho}\right]. \tag{22}$$

The region of the cylinder that is nearer to the line sources (φ = 180°) is expected to have more error in a typical numerical result for current density than the regions far away, since the current is more rapidly varying there. This is also observed, for example, in antennas near their feed region (and often motivates a higher discretization density in that region). Figure 1b shows the performance of the three residual-based error estimators for cylinder of figure 1a modeled with 200 cells. The reference solution in this case is the result obtained with 400 cells, and all three estimators predict a similar error pattern as the reference. All the estimators correctly identify the highest error region near φ = 180°.

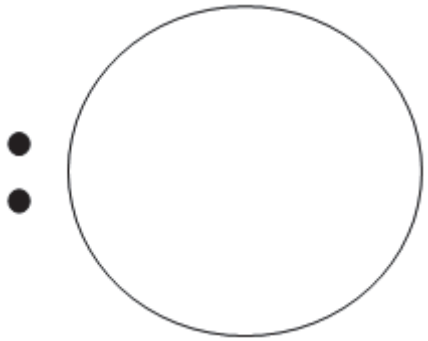

Fig. 1a. Geometry of the problem.

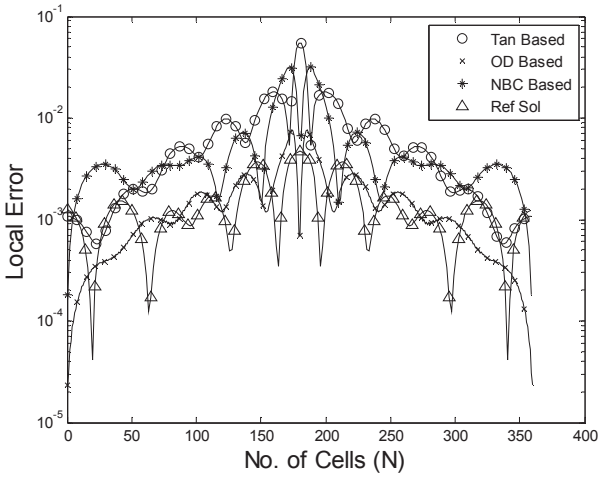

Fig. 1b. Local error for the problem of Figure 1a.

Figure 1c shows a plot of the global error produced by the same estimators, as a function of the number of unknowns or cells used in the computations. The global residual error levels decrease at approximately an O(*h*) rate as the cylinder model is refined. As discussed below, this is different from the rate at which the actual current density error decreases. These rates agree with those observed in [14–15] for the TE EFIE and linear basis functions.

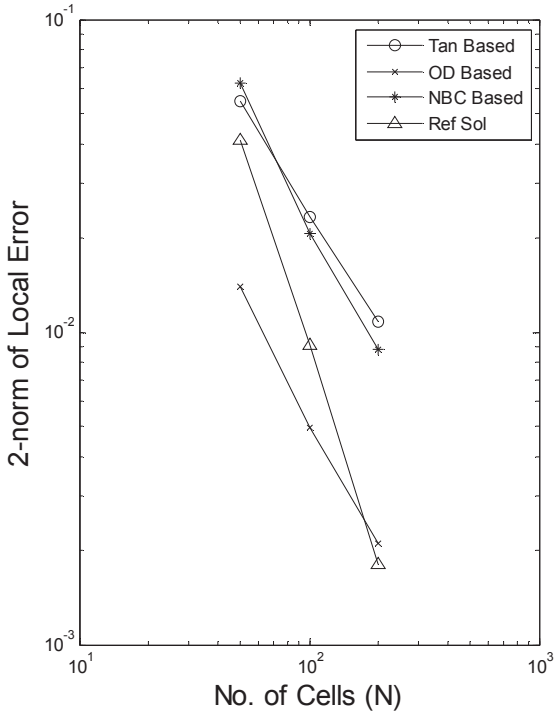

Fig. 1c. Global error for the problem of Figure 1a.

Figure 2a shows a keyhole-shaped cylinder, consisting of sections of two circular cylinders connected by a region with parallel walls. Figure 2b compares the performance of the three residual-based error estimators for a keyhole-shaped cylinder of 4.15λ total perimeter, modeled with 300 cells, for the same double line source excitation used in Figure 1. The larger end of the target has a radius of 0.32λ, while the smaller end has a radius of 0.14λ. The circular segments have centers separated by 1.32λ. The reference solution is obtained using 600 cells. There is a relatively large error level near the junction where the large circle meets the planar region (at 90° and 270°), and a larger error where the smaller circle meets the planar region (near 10° and 350°). The expected higher-error region at φ = 180° is correctly identified by the three estimators. Figure 2c shows a plot of the global error, as the number of unknowns used in the computations is varied. The global residual error levels decrease at approximately an O(*h*) rate as the cylinder model is refined.

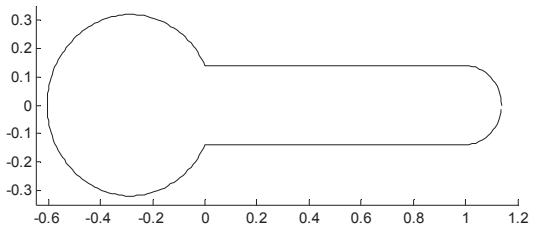

Fig. 2a. Geometry of the problem.

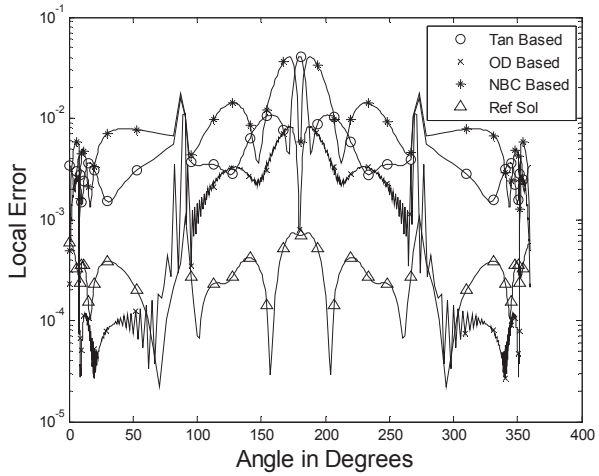

Fig. 2b. Local error for the problem of Figure 2a.

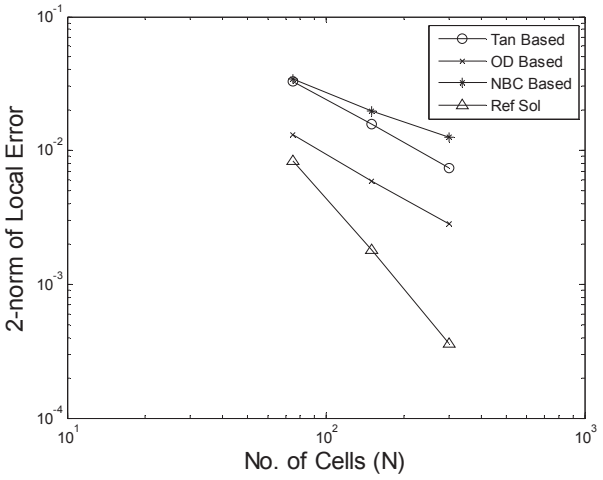

Fig. 2c. Global error for the problem of Figure 2a.

Figure 3 shows the local error computed by the three estimators for the same keyhole-shaped cylinder as shown previously in Figure 2a, but with a uniform plane wave excitation instead of line sources. The plane wave impinges symmetrically upon the larger end of the scatterer. It is expected that the error will be uniform except near discontinuities in the surface, as is confirmed by Figure 3. Error peaks near 10° and 90° angles correspond to curvature discontinuities where the circular regions meet the planar region of the surface. The higher spike corresponds to the sharper corner. Another interesting observation is that the error level gradually rolls off with increasing distance from the corner cells. The global error behavior is similar to that shown in Figure 2c and is not repeated here.

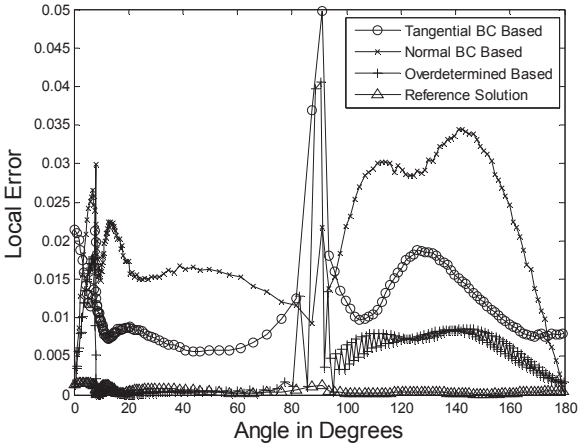

Fig. 3. Local error for the problem of Figure 2a for plane wave illumination.

VI. *h*-REFINEMENT

In this section, we demonstrate the utility of the tangential residual estimator presented in Section II to carry out adaptive *h*-refinement. This approach requires the cell size to be adaptively adjusted to control the error. The details of our *h*-refinement scheme are as follows. First, an initial coarse solution for the current density J is computed. That solution is used to compute the local error using the tangential residual error estimator. Once the local error values have been computed, they are sorted in descending order to identify the cells with the largest error levels. The 20% of those cells with the largest error are each divided into 3 cells, while each of the next 20% are divided into two cells. The remaining cells are left at their original size. After re-meshing, the problem is solved again to obtain a new solution for J, and a new local error estimate is obtained from the residual error. If the local error is still high or does not meet the user's criteria, the above procedure may be repeated recursively.

We implemented one iteration of the above procedure for a 5λ circumference cylinder illuminated with a pair of line sources as shown in

Figure 1a. The initial coarse solution was calculated for 100 cells and local error was computed. Based on the estimated local error values, a new mesh was created according to above scheme and is shown in Figure 4. The local error estimate computed before and after the adaptive refinement step is shown in Figure 5.

The tangential residual estimator identified the region of largest error to be that near the line source excitation, as expected, and the *h*-refinement step results in a large reduction of the tangential residual error in the refined region of the problem. Figure 6 shows the actual error in *J*, both before and after the adaptive refinement step, using (21) with a 600-cell solution for *J* as a reference.

Figure 6 shows that the error in *J* is reduced by a factor of more than 3 in the refined regions. After only one step of adaptive refinement, the combination of the tangential residual estimator and the *h*-refinement procedure produces a more uniform error level across the problem domain than originally obtained with a uniform mesh.

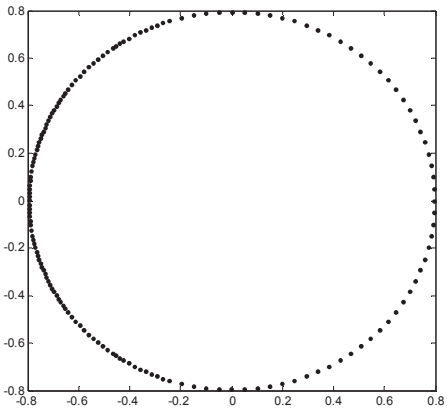

Fig. 4. Mesh density after the refinement.

VII. COMMENT ON THE GLOBAL ERROR RATES

In practice, the error in moment method results is usually dominated by the ability of the basis functions to represent the actual current density. For a piecewise-linear representation of a smoother function, this error should decrease at an $O(h^2)$ rate, where h is the nominal mesh size [3]. The reference solution error plotted in Figures 1c and 2c appears to decrease at approximately that rate. It has been observed in [14-15], and in Figures 1c and 2c, that for the TE EFIE operator, the residual error decreases at a rate that is one order less, an $O(h)$ rate. This is apparently due to the TE EFIE operator, which contains one integral and two derivatives. We note that for the transverse-magnetic (TM) polarization, where the operator involves one integration and no derivatives, the EFIE residual error appears to decrease at a rate that is one degree faster than the current error. It appears that each integral increases the rate by one order while each derivative decreases the rate by one order, relative to that of the current density. It has been observed that the residual error associated with the magnetic field integral equation (MFIE) decreases at the same rate as the current density error [14-15], while error in far field quantities may decrease at different rates from the current density for all these integral operators [14].

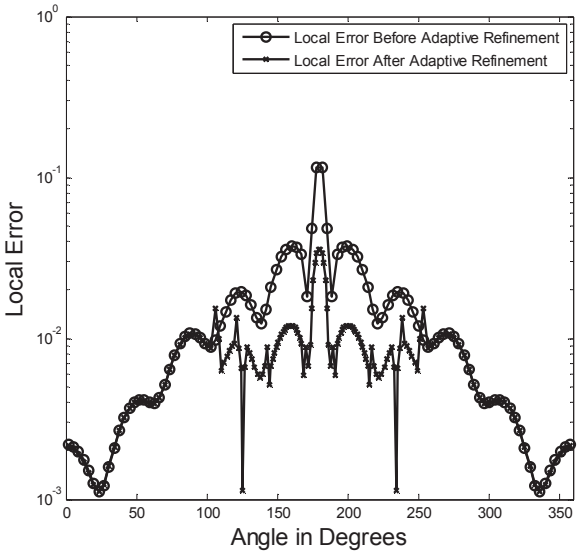

Fig. 5: Local error estimate before and after *h*-refinement.

The different error rates may limit our ability to use residual error estimators to determine the absolute global level of current density error in a particular result. Additional research is needed to address that issue. Despite this limitation, the residual estimators appear to be able to provide a local error distribution suitable for an adaptive refinement algorithm.

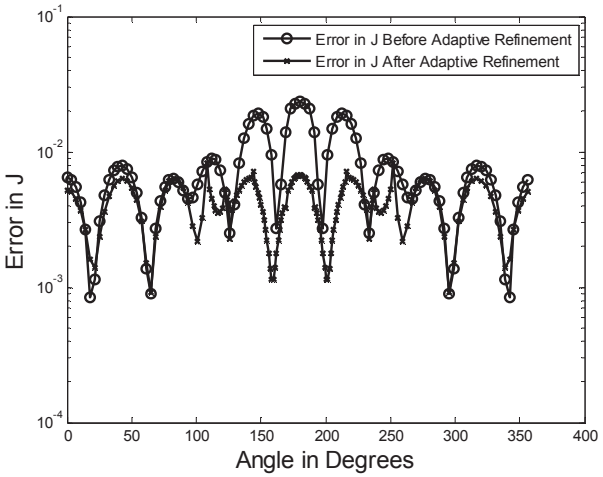

Fig. 6. Error in *J* before and after *h*-refinement.

VIII. COMPUTATIONAL COST OF ESTIMATORS

The relative computational cost of the estimators can be estimated as follows. The baseline cost without error estimation is

$$C_0 \cong \alpha N^2 + \beta N^3, \tag{23}$$

where α and β are the constants associated with matrix fill and solve times, respectively. The tangential and normal estimators add an approximate cost of

$$C_t \cong C_n \cong \alpha N^2, \tag{24}$$

since the residual computation in each case is comparable to an additional matrix fill.

The overdetermined error estimator has an approximate cost of

$$C_{over} \cong 2\alpha N^2 + 5\beta N^3, \tag{25}$$

since the matrix has twice as many entries, and since the least-square solution of a 2:1 rectangular system is reported to require about 5 times the operations of the LU factorization of a square system [16].

Thus, all three estimators add a cost of αN^2 operations, but the overdetermined estimator requires an additional $4\beta N^3$ operations beyond that. Thus, the overdetermined estimator is more expensive than the others, especially for large *N*.

IX. CONCLUSION

Three residual-based error estimators were considered for providing a local error estimate in conjunction with the method of moments solution of electromagnetic integral equations. All three estimators successfully located higher-error regions in test problems. All appear to be suitable for use in adaptive refinement schemes. The tangential residual and normal residual estimators have comparable cost and generally gave comparable results. The overdetermined estimator also gave similar results, but requires additional computation compared to the others. An example employing *h*-refinement was presented for illustration.

It was noted that for the EFIE the residual error decreases at a different rate than the current density error as a function of the nominal cell size. At the present time, this limits the use of simple residual error estimators for predicting the absolute error associated with a particular result. Additional research is warranted to better understand the behavior of the various errors and determine more cost-effective ways of estimating those errors.

REFERENCES

[1] R. F. Harrington, *Field Computation by Moment Methods*. New York: IEEE Press, 1993.

[2] J. J. H. Wang, *Generalized Moment Methods in Electromagnetics – Formulation and Solution of Integral Equations*. New York: Wiley, 1991.

[3] A. F. Peterson, S. L. Ray, and R. Mittra, *Computational Methods for Electromagnetics*. New York: IEEE Press, 1998.

[4] F. J. C. Meyer and D. B. Davidson, "A Posteriori Error Estimates for Two-Dimensional Electromagnetic Field Computations: Boundary Elements and Finite Elements," *Applied Computational Electromagnetic Society (ACES) Journal*, vol. 11, pp. 40-54, July 1996.

[5] J. Wang and J. P. Webb, "Hierarchal Vector Boundary Elements and Adaption for 3-D Electromagnetic Scattering," *IEEE Trans. Antennas Propagat.*, vol. 45, pp. 1869-1879, December 1997.

[6] M. Ainsworth and J. T. Oden, *A Posteriori Error Estimation in Finite Element Analysis*. New York: Wiley, 2000.

[7] E. Kita and N. Kamiya, "Error Estimation and Adaptive Mesh Refinement in Boundary Element Method, an Overview," *Engineering*

Analysis with Boundary Elements, vol. 25, pp. 479-495, 2001.

[8] X. Wang, M. M. Botha, and J.-M. Jin, "An Error Estimator for the Moment Method in Electromagnetic Scattering," *Microwave and Optical Technology Letters*, vol. 44, pp. 320-326, February 2005.

[9] M. M. Botha and D. B. Davidson, "An Explicit a Posteriori Error Indicator for Electromagnetic, Finite Element-Boundary Integral Analysis," *IEEE Trans. Antennas Propagat*., vol. 53, pp. 3717-3725, November 2005.

[10] M. M. Botha and D. B. Davidson, "Investigation of an Explicit, Residual-Based, A Posteriori Error Indicator for the Adaptive Finite Element Analysis of Waveguide Structures," *Applied Computational Electromagnetic Society (ACES) Journal*, vol. 21, no. 1, pp. 63-71, March 2006.

[11] A. P. C. Fourie, D. C. Nitch, and A. R. Clark, "Predicting MoM Error Currents by Inverse Application of Residual E-Fields," *Applied Computational Electromagnetic Society (ACES) Journal*, vol. 14, no. 3, pp. 72-75, November 1999.

[12] G. C. Hsiao and R. E. Kleinman, "Error Control in Numerical Solution of Boundary Integral Equations," *Applied Computational Electromagnetics Society (ACES) Journal*, vol. 11, pp. 32-36, 1996.

[13] K. J. Bunch and R. W. Grow, "The Boundary Residual Method for Three-Dimensional Homogeneous Field Problems with Boundaries of Arbitrary Geometries," *International Journal of Infrared and Millimeter Waves*, vol. 10, pp. 1007-1032, 1989.

[14] M. M. Bibby and A. F. Peterson, "On the Use of Over-Determined Systems in the Adaptive Numerical Solution of Integral Equations," *IEEE Trans. Antennas Propagat.,* vol. 53, pp. 2267-2273, July 2005.

[15] M. M. Bibby, A. F. Peterson, and C. M. Coldwell, "High Order Representations for Singular Currents at Corners," *IEEE Trans. Antennas Propagat*., vol. 56, pp. 2277-2287, August 2008.

[16] G. H. Golub and C. F. Van Loan, *Matrix Computations*. Baltimore: Johns Hopkins University Press, 1989.

Usman Saeed received the B.Sc. and M.Sc. degrees in Electrical Engineering from the University of Engineering & Technology, Lahore, in 2004 and 2006, respectively. From 2004 through 2006, he was a Lecturer with the Department of Electrical Engineering at the University of Engineering & Technology, Lahore. In 2006, he joined the Georgia Institute of Technology, Atlanta, GA as a Fulbright Fellow for M.S. studies. In 2008, he received the M.S. degree in Electrical and Computer Engineering from the Georgia Institute of Technology where he is currently working towards the Ph.D. degree.

Andrew F. Peterson received the B.S., M.S., and Ph.D. degrees in Electrical Engineering from the University of Illinois, Urbana-Champaign in 1982, 1983, and 1986 respectively. Since 1989, he has been a member of the faculty of the School of Electrical and Computer Engineering at the Georgia Institute of Technology, where he is now Professor and Associate Chair for Faculty Development. Within ACES, he served for six years as a member of the Board of Directors, and has been the Finance Committee Chair and the Publications Committee Chair. He was elevated to ACES Fellow in 2008. He served as a technical co-chair for the 25th Annual Review of Progress in Applied Computational Electromagnetics (ACES 2009) and is currently the ACES President.

An Adaptive Preconditioning Technique using Fuzzy Controller for Efficient Solution of Electric Field Integral Equations

Zhiwei Liu [1], Jiaqi Chen [1], and Rushan Chen [1,2]

[1] Department of Communication Engineering
Nanjing University of Science & Technology, Nanjing, 210094, China
zwliu1982@hotmail.com, cjq19840130@163.com, eechenrs@mail.njust.edu.cn

[2] Science and Technology on Space Microwave Laboratory, Xi'an, 710000, China
eechenrs@mail.njust.edu.cn

Abstract ― For efficiently solving large dense complex linear systems that arise in the electric field integral equation (EFIE) formulation of electromagnetic scattering problems, a new adaptive preconditioning technique using fuzzy controller (FC) is introduced and used in the context of the generalized minimal residual iterative method (GMRES) accelerated with the multilevel fast multipole method (MLFMM). The key idea is to control the choice of the preconditioner to be used in an iterative solver by using fuzzy controller. This approach allows the expert knowledge to be taken into account on the controller design and utilizes feedback to tune the cores of the fuzzy set. Numerical results show that the best preconditioner can be selected while maintaining low cost for adaptive procedures.

Index Terms ― Adaptive preconditioning technique, electric field integral equation, fuzzy controller, multilevel fast multipole method.

I. INTRODUCTION

In electromagnetic wave scattering calculations, a classic problem is to compute the induced currents on the surface of an object illuminated by a given incident plane wave. Such calculations, relying on Maxwell's equations, are crucial to the simulations of many industrial processes ranging from electromagnetic compatibility, antenna design, calculation of radar cross section (RCS), and so on. All of these simulations are very demanding in terms of computer resources, and require fast and efficient numerical methods, and approximate solution of Maxwell's equations. Using the equivalence principle, Maxwell's equations can be recast in the form of integral equations that relate the electric and magnetic fields to the equivalent electric and magnetic currents on the surface of the object.

The integral formulation considered in this paper is electric integral equation (EFIE) [1]. It is widely used for electromagnetic wave scattering problems as it can handle the most general geometries without any assumption. However, the matrix associated with the resulting linear systems is large and dense for electrically large targets in electromagnetic scattering. It is basically impractical to solve EFIE matrix equations using direct methods because they have a memory requirement of $O(N^2)$ and computational complexity of $O(N^3)$, where N refers to the number of unknowns. This difficulty can be circumvented by using Krylov iterative methods, and the required matrix-vector product operation can be efficiently evaluated by multilevel fast multipole mehthod (MLFMM) [2]. The use of MLFMM accelerated Krylov methods reduce the memory requirement to $O(N)$ and the computational complexity to $O(N\log N)$.

It is well-known that EFIE provides a first-kind integral equation which is ill-conditioned and gives rise to linear systems that are challenging to solve by Krylov methods. Therefore, a variety of preconditioning techniques have been used to improve the conditioning of the system before the iterative solution. Simple preconditioners like the

diagonal or diagonal blocks of the coefficient matrix can be effective only when the matrix has some degree of diagonal dominance [3]. The symmetric successive over-relaxation (SSOR) preconditioner shows good performance in the conjugate gradient (CG) iterative method [4], but becomes poor for nonsysmmetric systems. Incomplete LU (ILU) decomposed preconditioners have been successfully used on nonsysmmetric dense systems in [5], but the factors of the ILU preconditioner may become very ill-conditioned. Approximate inverse methods are generally less prone to instabilities on indefinite systems [6], and several preconditioners of this type have been proposed in electromagnetism. It has been shown in [7] that this technique outperforms more classical approaches like incomplete factorizations.

In this paper, we consider the performance of different predonditioners used in different problems. The choice of preconditioning methods suitable for one problem may not be the best for another one [13, 14]. Arbitrary selection in some cases lead to numerical problems like loss of convergence due to those initial choices. As an attempt for a possible remedy, a good choice of the preconditioner is made adaptively by a fuzzy controller after several iterations while maintaining low requirement for computer resource [8]. As a result, the idea of this work is to develop a general framework to dynamically change the parameters by taking into account the modeler knowledge. And the choices related to those preconditioning methods are considered as a control problem.

This paper is organized as follows. Section II gives a brief introduction to the EFIE formulation and MLFMM. Section III describes the construction and implementation of the fuzzy controller in more details. Numerical experiments with a few electromagnetic scattering problems are presented to show the efficiency of the adaptive preconditioner by FC in Section IV. Section V gives some conclusions.

II. EFIE Formulation and MLFMM

The EFIE formulation of electromagnetic wave scattering problems using planar Rao-Wilton-Glisson (RWG) basis functions for surface modeling is presented in [1]. The resulting linear systems from EFIE formulation after Galerkin's testing are briefly outlined as follows:

$$\sum_{n=1}^{N} Z_{mn} a_n = V_m, \qquad \mathrm{m} = 1, 2, ..., N \quad (1)$$

where

$$Z_{mn} = jk \int_s \mathbf{f}_m(\mathbf{r}) \bullet \int_{s'} (\bar{\mathbf{I}} + \frac{1}{k^2} \nabla\nabla\bullet)[G(\mathbf{r}, \mathbf{r}')\mathbf{f}_n(\mathbf{r}')] ds ds'$$

$$V_m = \frac{1}{\eta} \int_s \mathbf{f}_m(\mathbf{r}) \bullet \mathbf{E}^i(\mathbf{r}) ds.$$

Here, $G(\mathbf{r}, \mathbf{r}')$ refers to the Green's function in free space and $\{\alpha_n\}$ is the column vector containing the unknown coefficients of the surface current expansion with RWG basis functions. Also, as usual, $\mathbf{r}$ and $\mathbf{r}'$denote the observation and source point locations. $\mathbf{E}^i(\mathbf{r})$ is the incident excitation plane wave, and η and k denote the free space impendence and wave number, respectively. Once the matrix equation (1) is solved by numerical matrix equation solvers, the expansion coefficients $\{\alpha_n\}$ can be used to calculate the scattered field and RCS. In the following, we use $\mathbf{A}$ to denote the coefficient matrix in equation (1), $\mathbf{x} = \{\alpha_n\}$, and $\mathbf{b} = \{V_m\}$ for simplicity. Then, the EFIE matrix equation (1) can be symbolically rewritten as:

$$\mathbf{Ax = b.} \quad (2)$$

To solve the above matrix equation by an iterative method, the matrix-vector products are needed at each iteration. Physically, a matrix-vector product corresponds to one cycle of iteractions between the basis functions. The basic idea of the fast multipole method (FMM) is to convert the interaction of element-to-element to the interaction of group-to-group. Here a group includes the elements residing in a spatial box. The mathematical foundation of the FMM is the addition theorem for the scalar Green's function in free space. Using the FMM, the matrix-vector product $\mathbf{Ax}$ can be written as:

$$\mathbf{Ax} = \mathbf{A}_N\mathbf{x} + \mathbf{A}_F\mathbf{x}. \quad (3)$$

Here, $\mathbf{A}_N$ is the near part of $\mathbf{A}$ and $\mathbf{A}_F$ is the far part of $\mathbf{A}$.

In the FMM, the calculation of matrix elements in $\mathbf{A}_N$ remains the same as in the MoM procedure. However, those elements in $\mathbf{A}_F$ are not explicitly computed and stored. Hence, they are not numerically available in the FMM. It has been shown that the operation complexity of FMM to

perform **Ax** is $0(N^{1.5})$. If the FMM is implemented in multilevel, the total cost can be reduced further to $0(N\log N)$ [2].

III. ADAPTIVE PRECONDITIONER USING FUZZY CONTROLLER

In this section, we show how fuzzy logic provides a methodology for representing and implementing the expert knowledge about how to control the process. In particular, we apply this methodology to control the process of preconditioner of an iterative solver. We first underline the main components and characteristic mechanisms of a FC. Afterwards, we present how to control the choice of the preconditioner using FC.

First of all, the "early steps" is defined as the first several steps of the iterative solver. If the convergence rate of the iterative solver can be evaluated approximately by the early steps. Using this information, we could decide which preconditioner is the most suitable one to accelerate solution of the linear system. The key problem is how to evaluate the convergence rate from the early steps. In this paper, the residual of the iterative solver and the difference of the residual between two steps are used to evaluate this information.

Generally, a preconditioner corresponding to the smallest residual at the first step can be considered as the best preconditioner. However, the largest difference of the residual between first two steps can be considered as the best precondioner. High order difference can also be used to describe the property of a preconditioner. Therefore, a fuzzy controller is used and shown in Figure 1. The *process* block is the object to be controlled. $\boldsymbol{u}(t)$ is the process input and $\boldsymbol{y}(t)$ is the process output. $\boldsymbol{r}(t)$ represents the desired target for the output of the process. The *controller* block is for changing the value of $\boldsymbol{u}(t)$ based on the controller input $\boldsymbol{y}(t)$ and the target $\boldsymbol{r}(t)$. The error as well as the rate of change-in-error defined as

$$\boldsymbol{e}(t) = \boldsymbol{r}(t) - \boldsymbol{y}(t), \tag{4}$$

$$\frac{\partial}{\partial t}\boldsymbol{e}(t) = \frac{\boldsymbol{e}(t) - \boldsymbol{e}(t-\Delta t)}{\Delta t}, \tag{5}$$

where Δt is the time between two consecutive data captured by the controller. In particular, Δt is set equal to one in an iterative solver.

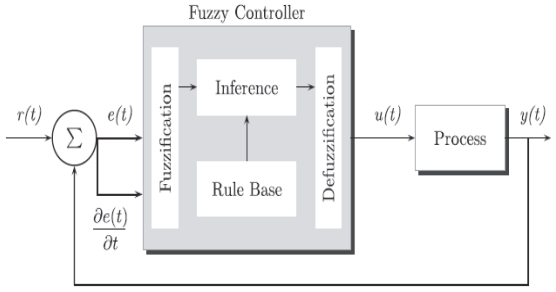

Fig. 1. Block diagram of a feedback fuzzy control.

As a controller for the choice of the preconditioner when solving equation (2), the feedback fuzzy control system takes advantage of residual at each iterative step. $\boldsymbol{u}(t)$ is the preconditioner selected by controller, $\boldsymbol{y}(t)$ is the approximate solution and $\boldsymbol{r}(t)$ represents the right-hand-side of the equation (2). As a result, $\boldsymbol{e}(t)$ is the residual defined by

$$\boldsymbol{e}(t) = \boldsymbol{b} - \boldsymbol{A}\boldsymbol{x}(t). \tag{6}$$

Therefore, $\partial \boldsymbol{e}(t)/\partial t$ is the rate of change-in-residual which means the difference of residual between two iterative steps.

This fuzzy-logic-based approach allows expert knowledge to be taken into account on the controller design. A preconditioning method is selected by controller with the principle that the best preconditioner performs highest convergence rate for a given problem. After several iterations, the approximate convergence rate can be defined by using the high order difference of residual which shown as

$$\boldsymbol{rate} = \boldsymbol{e} + \partial \boldsymbol{e}/\partial t + \frac{1}{2}\partial^2 \boldsymbol{e}/\partial t^2 + \cdots \tag{7}$$

Obviously, if the order equal to the total number of iterations, the rate can describe the convergence exactly. Due to the finite computer resource, we often use two or three iterative steps to compute the approximate rate. The formulations can be defined by

$$\boldsymbol{rate} = \boldsymbol{e} + \partial \boldsymbol{e}/\partial t, \tag{8}$$

$$\boldsymbol{rate} = \boldsymbol{e} + \partial \boldsymbol{e}/\partial t + \frac{1}{2}\partial^2 \boldsymbol{e}/\partial t^2. \tag{9}$$

As a result, we choose the preconditoner with the largest convergence rate as a suitable preconditioning method.

Assume that three preconditioning methods are available ranging from Jacobi, SSOR, and SAI (sparse approximate inverse). The main steps of

this preconditioning method are described as follows:

Step 1: Construct the preconditioners by those three methods separately.

Step 2: Do several iterations by Krylov iterative methods and note the residual and change-in-residual at each step. In this paper, the number of iterations is set to be 3.

Step 3: Apply the FC to choose the best preconditioner.

Step 4: Use the best preconditonier to complete the iteration.

IV. NUMERICAL RESULTS

In this section, we show some numerical results that illustrate the effectiveness of the proposed adaptive preconditioning method for the solution of large dense linear systems arising from the discretization of the EFIE formulation in electromagnetic scattering problems. In our experiments, the restarted version of GMRES(m) [9] algorithm is used as an iterative method, where m is the dimension size of Krylov subspace for GMRES. Additional details and comments on the implementation are given below:

(1) Zero vector is taken as initial approximate solution for all examples.

(2) The maximum number of iterations is limited to be 2000.

(3) The iteration process is terminated when the normwise backward error is reduced by 10^{-3} for all examples.

We investigate the performance of the adaptive preconditioner using a fuzzy controller on four examples, which is shown in Figs. 2-5. They consist of an almond with 1815 unknowns at 3GHz, a double ogive with 2574 unknowns at 5GHz, a cube with 3366 unknowns at 350MHz, and a sphere with 3972 at 200MHz. The first two geometries come from [10], the side length of the cube is 1m and the radius of the sphere is also 1m. The numerical results of bistatic RCS for horizontal polarization are also displayed in Figs. 2-5 for these four geometries. All experiments are performed on a Pentium 4 with 2.66 GHz CPU and 960MB RAM in single precision.

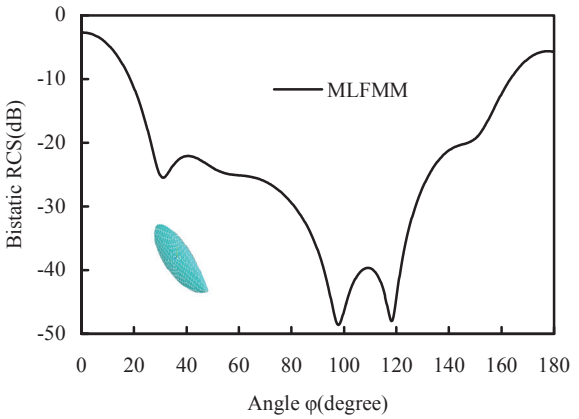

Fig. 2. Bistatic RCS for horizontal polarization at 3GHz for NASA Almond.

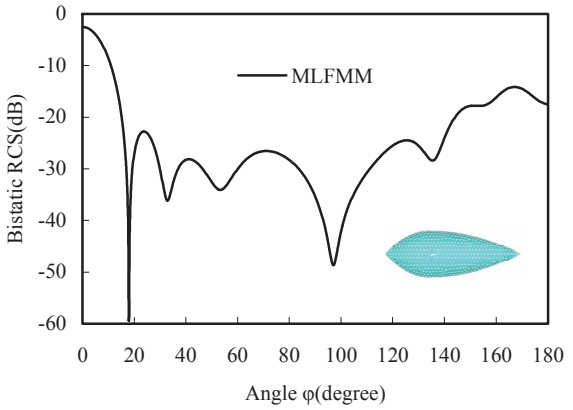

Fig. 3. Bistatic RCS for horizontal polarization at 5GHz for double-ogive.

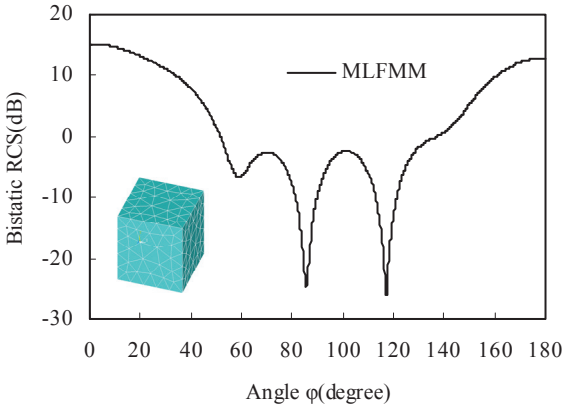

Fig. 4. Bistatic RCS for horizontal polarization at 350MHz for PEC cube.

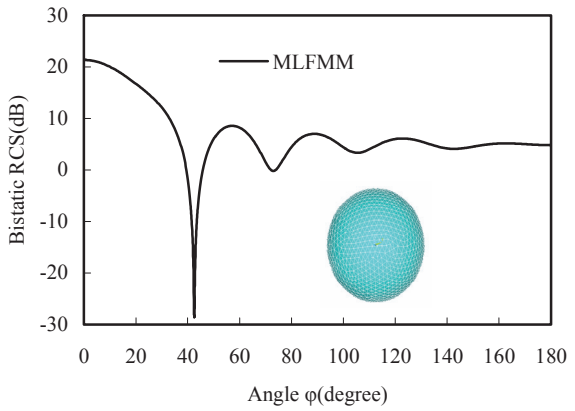

Fig. 5. Bistatic RCS for horizontal polarization at 200MHz for PEC sphere.

Figures 6-9 show convergence history of GMRES(*m*) algorithms with different preconditioners for all examples. It can be observed that the adaptive preconditioned GMRES has almost the same convergence history as that of the optimal preconditioner.

Since a good preconditioner depends not only on its effect on convergence but also on its construction and implementation time. Tables 1-4 list the construction time and total solution time of GMRES algorithms with different preconditioners on all examples. According to these results, we can easily find that the proposed adaptive preconditioning method using FC requires more construction time than other preconditioners. As a control method for the choice of preconditioners, the adaptive preconditioner has to prepare all of the preconditioners for choice. Therefore, large time costs during the process of construction of all the preconditioners. However, the new method shows its efficiency on convergence in these examples. Furthermore, the initial time of an adaptive preconditioner is negligible when compared with the total CPU time cost in monostatic RCS computation. Therefore, this proposed method is suitable for analysis of monostatic scattering.

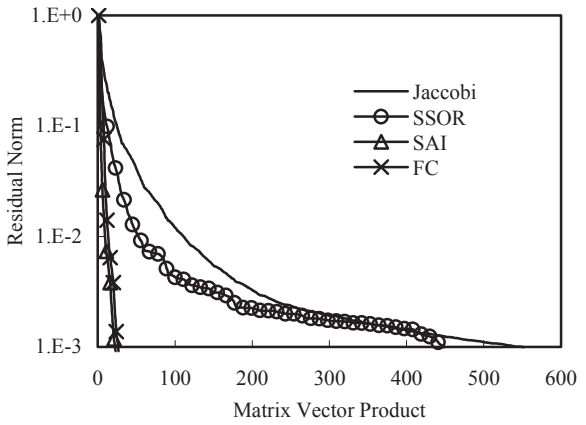

Fig. 6. Convergence history of GMRES algorithms with different preconditioners on the almond example.

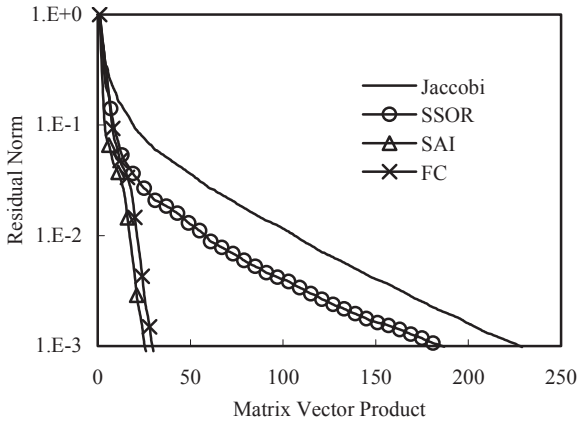

Fig. 7. Convergence history of GMRES algorithms with different preconditioners on the double-ogive example.

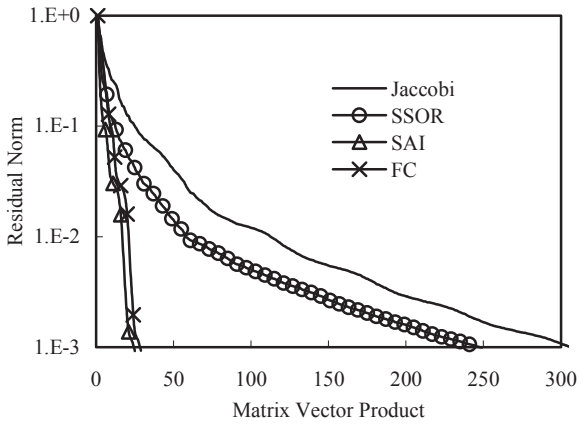

Fig. 8. Convergence history of GMRES algorithms with different preconditioners on the cube example.

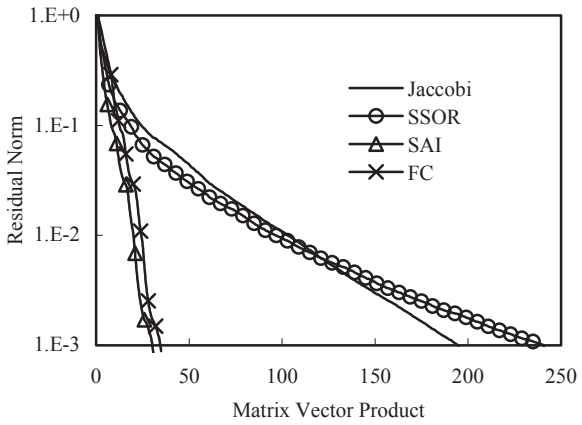

Fig. 9. Convergence history of GMRES algorithms with different preconditioners on the sphere example.

Table 1: Comparison of the cost and performance of different preconditioners on the almond example (Time: Second)

Almond	Construc-time	Number of Iterations	Sol-time	Total-time
Jacobi	/	552	31.73	31.73
SSOR	/	449	28.25	28.25
SAI	18.42	23	1.61	20.03
FC-AP	25.45	27	1.77	27.32

Table 2: Comparison of the cost and performance of different preconditioners on the double-ogive example (Time: Second)

Double ogive	Construc-time	Number of Iterations	Sol-time	Total-time
Jacobi	/	229	22.94	22.94
SSOR	/	187	20.56	20.56
SAI	11.61	26	2.86	14.47
FC-AP	16.77	30	3.19	19.96

Table 3: Comparison of the cost and performance of different preconditioners on the cube example (Time: Second)

Cube	Construc-time	Number of Iterations	Sol-time	Total-time
Jacobi	/	308	33.38	33.38
SSOR	/	249	29.91	29.91
SAI	23.02	31	3.17	26.19
FC-AP	33.45	35	3.48	36.93

Table 4: Comparison of the cost and performance of different preconditioners on the sphere example (Time: Second)

Sphere	Construc-time	Number of Iterations	Sol-time	Total-time
Jacobi	/	195	31.44	31.44
SSOR	/	241	42.02	42.02
SAI	17.33	31	5.48	22.81
FC-AP	24.72	35	5.98	30.70

V. CONCLUSIONS AND COMMENTS

In this paper, a fuzzy controller is presented and used for building robust adaptive preconditioning method for efficiently solving large dense linear systems that arise in EFIE formulation of electromagnetic scattering problems. The main idea is to make a choice of preconditioners which performs the highest convergence rate. Numerical experiments on several examples are preformed and comparison with general preconditioners are made, which shows the new method is more efficient.

ACKNOWLEDGMENT

The authors would like to thank the assistance and support by National Key Laboratory Foundation of China (No. 9140C5305021006).

REFERENCES

[1] S. M. Rao, D. R. Wilton, and A. W. Glisson, "Electromagnetic Scattering by Surfaces of Arbitrary Shape," *IEEE Transactions on Antennas and Propagation*, vol. 30, no. 3, pp. 409-418, 1982.

[2] W. C. Chew, J. M. Jin, E. Midielssen, and J. M. Song, *Fast and Efficient Algorithms in Computational Electromagnetics*. Artech House, Boston, 2001.

[3] J. M. Song, C. C. Lu, and W. C. Chew, "Multilevel Fast Multipole Algorithm for Electromagnetic Scattering by Large Complex Objects," *IEEE Transactions on Antennas and Propagation*, vol. 45, no. 10, pp. 1488-1493, 1997.

[4] Eisenstat SC. "Efficient Implementation of a Class of Preconditioned Conjugate Gradient Methods," *SIAM Journal on Scientific and Statistical Computing*, vol. 2, pp. 1-4, 1981.

[5] K. Sertel and J. L. Volakis, "Incomplete LU Preconditioner for FMM Implementation," *Microwave and Optical Technology Letters*, vol. 26, no. 7, pp. 265-267, 2000.
[6] B. Carpentieri, I. S. Duff, L. Griud, and G. Alleon, "Combing Fast Multipole Techniques and an Approximate Inverse Preconditioner for Large Electromagnetism Calculations," *SIAM Journal on Scientific Computing,* vol. 27, no. 3, pp. 774-792, 2005.
[7] B. Carpentieri, I. S. Duff, and L. Griud, "Sparse Pattern Selection Strategies for Robust Frobenius-Norm Minimization Preconditioners in Electromagnetism," *Numerical Linear Algebra Applications,* vol. 7, no. 7-8, pp. 667-685, 2000.
[8] R. S. Silva and R. C. Almeida, "Using Fuzzy Controller as Adaptive Procedures in the Finite Element Method," *Communications in numerical methods in engineering*, vol. 24, no. 6, pp. 449-465, June 2008.
[9] R. B. Lehoucq, D. C. Sorensen, and C. Yang, *ARPACK User's guide: Solution of large-scale problem with implicitly restarted Arnoldi methods*, SIAM, Philadelphia, 1998.
[10] A. C. Woo, H. T. G. Wang, M. J. Schuh, and M. L. Sanders, "EM Programmer's Notebook-Benchmark Radar Targets for the Validation of Computational Electromagnetics Programs," *IEEE Antennas and Propagation Magazine*, vol. 35, no. 1, pp. 84-89, Feb., 1993.
[11] B. Carpentieri, "An Adaptive Approximate Inverse-Based Preconditioner Combined with the Fast Multipole Method for Solving Dense Linear Systems in Electromagnetic Scattering," *Applied Computational Electromagnetic Society (ACES) Journal*, vol. 24, no. 5, pp. 504-510, October 2009.
[12] J. Lee, J. Zhang, and C. Lu, "Performance of Preconditioned Krylov Iterative Methods for Solving Hybrid Integral Equations in Electromagnetics," *Applied Computational Electromagnetic Society (ACES) Journal*, vol. 18, no. 3, pp. 54-61, November 2003.
[13] D. Loqhin, D. Ruiz, and A. Touhami, "Adaptive Preconditioner for Nonlinear Systems of Equations," *Journal of Computational and Applied Mathematics*, vol. 189, no. 1-2, May 2006.
[14] M. M. Gourary, S. G. Rusakov, S. L. Ulyanov, M. M. Zharov, K. K. Gullapalli, and B. J. Mulvaney, "Adaptive Preconditioners for the Simulation of Extremely Nonlinear Circuits using Harmonic Balance," *Microwave Symposium Digest, 1999 IEEE MTT-S International*, vol. 2, pp. 779-782, 1999.

Zhiwei Liu was born in Jiangxi Province, P. R. China in 1982. He received B.S. degree in Computer Science from Nanjing Univ. of Sci. & Tech. in 2003, M.S. degree in Nanjing Institute of Electro. & Tech. in 2006, and is currently working toward the Ph.D. degree at Nanjing Univ. of Sci. & Tech. His research interests focus on theory of electromagnetic scattering and inverse scattering.

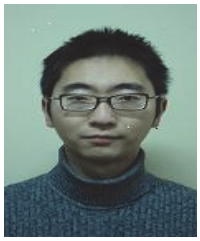

Jiaqi Chen was born in Gansu Province, P. R. China. He received the B.S. degree in Communication Engineering from Nanjing Univ. of Sci. and Tech., China, in 2005, and is currently working toward the Ph.D. degree at Nanjing Univ. of Sci. and Tech. His current research interests include computational electromagnetics, electromagnetic scattering and propagation and synthetic aperture radar imaging.

Rushan Chen (M'01) was born in Jiangsu, P. R. China. He received his B.S. and M.S. degrees from the Dept. of Radio Eng., Southeast University, in 1987 and in 1990, respectively, and his Ph.D. from the Dept. ofElectronic Engineering, City University of Hong Kong in 2001. He joined the Dept. of Electrical Engineering, Nanjing Univ. of Sci. & Tech., where he became a Teaching Assistant in 1990 and a Lecturer in 1992. His research interests mainly include microwave/millimeter-wave systems, measurements, antenna, RF-integrated circuits, and computational electromagnetics.

Augmented MLFMM for Analysis of Scattering from PEC Object with Fine Structures

Ming Chen[1], Ru Shan Chen[1, 2], and Xiao Qing Hu[1]

[1]Department of Communication Engineering
Nanjing University of Science and Technology, China

[2]Science and Technology on Space Microwave Technology, China
eechenrs@mail.njust.edu.cn

Abstract ― In this paper, a multilevel Green's function interpolation method (MLGFIM) combined with multilevel fast multipole method (MLFMM) is presented for solving the electromagnetic scattering from the objects with fine structures. In the conventional MLFMM, the size of the finest cube must be larger than a definite value, which is typically 0.2 λ; it often generates a large number of unknowns in each finest cube especially for objects with fine structures. Accordingly, it requires a lot of memory to store the near-field impedance matrix in MLFMM. In order to decrease the memory requirement of the near-field matrix in the MLFMM, the MLGFIM is introduced to calculate the near-field interactions. The number of unknowns in each cube can be less than a required number regardless of the size of the cube in the MLGFIM. To further reduce the computational complexity, many recompressed techniques, such as the adaptive cross approximation (ACA), QR factorization, and singular value decomposition (SVD), are applied to compress the low rank Green's function matrix for speeding up the matrix-vector multiplication. Numerical results are given to demonstrate the accuracy and efficiency of the proposed method.

Index Terms **-** Multilevel fast multipole method (MLFMM), multilevel Green's function interpolation method(MLGFIM), QR factorization.

I. INTRODUCTION

The method of moment (MoM) [1-2] has found wide-spread application in a variety of electromagnetic radiation and scattering problems, When the number of unknowns is small, the resultant matrix equations in MoM can be solved directly with computational complexity of $O(N^3)$, where N is the number of unknowns. For moderate scale problems, the matrix equations are often solved by iterative solvers, such as the conjugate gradient method (CG), and the biconjugate gradient method (BiCG), with $O(N^2)$ operation for each matrix-vector product (MVP). The memory requirement is $O(N^2)$ for both the direct and the iterative solvers. The complexity of the direct or iterative solvers mentioned above blocks their application to the analysis of scattering from electrically large objects, the MoM can only be used for small scale problems. In recent years, the fast multipole method (FMM) [3-5] has been developed to accelerate the MVP with complexity of $O(N^{1.5})$. With the multilevel fast multipole algorithm (MLFMM) [6-10], the complexity is further reduced to $O(N\log N)$; this represents an impressive improvement as compared with conventional $O(N^3)$ or $O(N^2)$ techniques. By using the MLFMM, a common PC can solve problems which only can be solved by supercomputer in the past.

The MLFMM can be applied to almost all electromagnetic problems, such as microwave circuits, antennas, scattering targets, etc. However, it is still very challenging to apply the method to objects with fine structures. Accurate

discretization produces a large number of unknowns in each of the finest cubes. Accordingly, the near-field interaction matrices grow rapidly with the surface discretization density. The time used to calculate the near-field impedance matrix is also very long. Therefore, for the objects with fine structures, the MLFMM still challenged by the CPU time and memory requirement. It is necessary to further improve the efficiency of the MLFMM.

In order to overcome the bottleneck of conventional MLFMM in the near-field for the objects with fine structure, a multilevel Green's function interpolation method (MLGFIM) [11-16] combined with the MLFMM (MLGFIM-MLFMM) is proposed in this paper. The MLGFIM enables a highly compact representation and efficient numerical computation of the dense matrices when the source and observation cubes are well separated. The complexity of storage requirements and the MVP of the MLGFIM is approximately $O(C_1 N)$ as shown in [16] while the complexity is $O(C_2 N \log(N))$ for the MLFMM as shown in [6]. By comparing the numerical results of [6] and [16], the coefficient of C_1 is much larger than C_2. This is because when applying the MLGFIM into a full wave electromagnetic problem, the number of interpolation points must be enlarged to keep the accuracy of the Green's function when the cube size increases. A large number of interpolation points drastically reduce the efficiency of the MLGFIM. However, the MLGFIM has its own merit. Compared with MLFMM, the octree in MLGFIM can be split until the number of unknowns in each cube is less than a required number regardless of the cube size. The octree structure is the same as in the low-frequency fast multipole method (LF-FMM) [17]. In this paper, the MLGFIM is used to calculate part of the near-field interaction for reducing the memory requirement of the near-field while the MLFMM is used to calculate the far-field interaction. In contrast to the conventional MLFMM, the augmented MLFMM make the near-field memory requirement reduce greatly, this idea makes the objects with fine structure problems solvable by MLGFIM-MLFMM.

The remainder of this paper is organized as follows. Section II gives a brief introduction to the electric field integral equation (EFIE) and the Lagrange interpolation in MLGFIM. The ACA technique, QR factorization, and SVD factorization is employed to compress the low rank Green's function matrix to accelerate the MVP. Section III presents the numerical results that demonstrate the accuracy and efficiency of the proposed method. Finally, some conclusions are given in section IV.

II. THEORY

Consider a three-dimensional electromagnetic problem; the object is illuminated by an incident wave $\vec{E_i}$ that induces current $\vec{J}_s$ on the conducting surface. The current satisfies the following electric-field integral equation:

$$\vec{E_i}\,|_{\tan} = \iint_s [\, j\omega\mu \vec{J_s}(\vec{r}')g(\vec{r},\vec{r}') - \frac{j}{\omega\varepsilon}(\nabla' \vec{J_s}(\vec{r}'))\nabla' g(\vec{r},\vec{r}')]_{\tan} ds' \quad (1)$$

In which Green's function $g(\vec{r},\vec{r}') = \dfrac{e^{-jk|\vec{r}-\vec{r}'|}}{4\pi|\vec{r}-\vec{r}'|}$, ω is the angular frequency, and k is the wave number which is $\omega\sqrt{\mu\varepsilon}$. μ , ε are the free space permeability and permittivity, respectively. The second "tan" denotes the component that is tangential to the conducting surface S . By expanding the unknown surface current density $\vec{J_s}$ using Rao-Wilton-Glisson (RWG) basis functions and applying Galerkin's method on (1) gives a MoM equation:

$$\bar{\bar{Z}}\bar{x} = \bar{V} \quad (2)$$

where

$$Z_{mn} = \iint_{s_m} ds \iint_{s_n} ds' [\, j\omega\mu \vec{J_m}(\vec{r})\vec{J_n}(\vec{r}') - \frac{j}{\omega\mu}(\nabla\cdot\vec{J_m}(\vec{r}))(\nabla'\cdot\vec{J_m}(\vec{r}'))]g(\vec{r},\vec{r}') \quad (3)$$

and

$$V_m = \iint_{s_m} \vec{J_m}(\vec{r})\vec{E_i}(\vec{r})ds \quad (4)$$

Here, $\bar{\bar{Z}}$ is the impedance matrix, $\bar{x}$ are the coefficients of the induced current expanded in RWG basis functions, and $\bar{V}$ is the vector of incident field. The dimension of $\bar{\bar{Z}}$ is often as high as millions for electrically large EM scattering problems. This blocks the MoM application to the analysis of scattering from electrically large objects. The FMM and its multilevel version, MLFMM has been developed to accelerate the

MVP, lower the memory requirement to $O(N^{1.5})$ and $O(N\log N)$. The process of the MVP in MLFMM is splitted in two parts as

$$\overline{\overline{Z}}\,\bar{x} = \overline{\overline{Z}}_{NF}\,\bar{x} + \overline{\overline{Z}}_{FF}\,\bar{x}. \tag{5}$$

Here, the first term $\overline{\overline{Z}}_{NF}$ is the interactions from the nearby cubes, and is calculated directly by MoM. While the second term $\overline{\overline{Z}}_{FF}$ is the interactions from the well-separated cubes which are computed in a group-by-group manner by MLFMM. The computation of $\overline{\overline{Z}}_{NF}\,\bar{x}$ is done directly, while the computation of $\overline{\overline{Z}}_{FF}\,\bar{x}$ is done in three stages called the aggregation phase, the translation phase, and the disaggregation phase which are contributions from far-field interaction computation. These steps are now well documented and we refer the reader to consult the literature [6-8] for more details.

For the objects with fine structures, a straightforward MoM for computing the near-field $\overline{\overline{Z}}_{NF}$ is very expensive. Our approach is to approximate part of $\overline{\overline{Z}}_{NF}$ by a matrix which can be stored in a data-sparse format; The MLGFIM is introduced in MLFMM to descript part of the near-field matrix by a sparse matrix format leading to a significant reduction in the near-field memory requirement.

A. Data-sparse representation of the low-rank matrix

Here, the free space Green function $g(\vec{r},\vec{r}') = e^{-jk|\vec{r}-\vec{r}'|}/4\pi|\vec{r}-\vec{r}'|$ is considered. $\vec{r}$ means the field point located in cube m and $\vec{r}'$ means the source point located in cube n. If cube m and cube n are two well-separated cubes, the Green function $G(\vec{r},\vec{r}') = e^{-jk|\vec{r}-\vec{r}'|}/|\vec{r}-\vec{r}'|$ can be interpolated using Lagrange interpolation technique, it can be written as

$$G(\vec{r},\vec{r}') = \sum_{p=1}^{K}\sum_{q=1}^{K}\omega_{m,p}(\vec{r})\omega_{n,q}(\vec{r}')G(r_{G_m,p}, r'_{G_n,q}) \tag{6}$$

where $\omega_{m,p}(\vec{r})$ and $\omega_{n,q}(\vec{r}')$ are the *pth* Lagrange interpolation points in cube m and *qth* Lagrange interpolation points in cube n, $r_{m,p}$ denotes the Lagrange interpolation in cube m. K is the number of interpolation points in cube m or n, $G(r_{m,p}, r'_{n,q})$ is the Green's function matrix generated from interpolation point $r'_{n,q}$ in cube n to interpolation point $r_{m,p}$ in cube m, substituting (6) into (3) gives :

$$Z_{mn} = \frac{j\omega\mu}{4\pi}\sum_{p=1}^{k}\sum_{q=1}^{k}G(r_{m,p}, r'_{n,q})\iint_{s_m}\overrightarrow{J_m}(\vec{r})\omega_{m,p}(\vec{r})ds\iint_{s_n}\overrightarrow{J_n}(\vec{r}')\omega_{n,q}(\vec{r}')ds' - \frac{j}{4\pi\omega\mu}\sum_{p=1}^{k}\sum_{q=1}^{k}G(r_{m,p}, r'_{n,q})\iint_{s_m}\nabla\cdot\overrightarrow{J_m}(\vec{r})\omega_{m,p}(\vec{r})ds\iint_{s_n}\nabla'\overrightarrow{J_n}(\vec{r}')\omega_{n,q}(\vec{r}')ds' \tag{7}$$

The submatrix Z_{mn} can be represented in a factorized form

$$\overline{\overline{Z}}^{t,s} = W^t G^{t,s} W^{s^T} \tag{8}$$

where $W^t = \left[W_1^t \;\; W_2^t\right]$, $W^s = \left[W_1^s \;\; W_2^s\right]$

$$G^{t,s} = \begin{bmatrix} \overline{\overline{G}}_1^{t,s} & 0 \\ 0 & \overline{\overline{G}}_2^{t,s} \end{bmatrix} \tag{9}$$

$W_1^t, W_2^t \in \mathbb{C}^{M_m\times K}$ $\quad W_1^s \;\; W_2^s \in \mathbb{C}^{M_n\times K}$

$\overline{\overline{G}}_1^{t,s}, \overline{\overline{G}}_2^{t,s} \in \mathbb{C}^{K\times K}$

And

$$\overline{\overline{W}}_{1mp}^{t} = \iint_{s_m}\overrightarrow{J_m}(\vec{r})\omega_{m,p}(\vec{r})ds$$

$$\overline{\overline{W}}_{2mp}^{t} = \iint_{s_m}\nabla\cdot\overrightarrow{J_m}(\vec{r})\omega_{m,p}(\vec{r})ds$$

$$\overline{\overline{W}}_{1nq}^{s} = \iint_{s_n}\overrightarrow{J_n}(\vec{r}')\omega_{n,q}(\vec{r}')ds'$$

$$\overline{\overline{W}}_{2nq}^{s} = \iint_{s_n}\nabla'\overrightarrow{J_n}(\vec{r}')\omega_{n,q}(\vec{r}')ds'$$

$$\overline{\overline{G}}_{1pq}^{t,s} = \frac{j\omega\mu}{4\pi}G(r_{m,p}, r'_{n,q})$$

$$\overline{\overline{G}}_{2pq}^{t,s} = \frac{-j}{4\pi\omega\mu}G(r_{m,p}, r'_{n,q}) \tag{10}$$

where M_m and M_n denote the number of unknowns in cube m and n. p is the number of interpolation points along each direction, in which $d = 1,2,3$, for 1-, 2-, and 3-D problems, respectively. Clearly, the rank of matrix $\overline{\overline{Z}}^{t,s}$ is at most $2\times$K regardless of the cardinality of t and s, it is obvious that if $K << \min(M_m, M_n)$, the computing of $\overline{\overline{W}}_m$, $\overline{\overline{W}}_n$ and $\overline{\overline{G}}_{mn}$ will be significantly faster than that of $\overline{\overline{Z}}_{mn}$. Both the memory requirement and the matrix filling time are greatly reduced.

From above, we know that the MLGFIM is a rank-based method; it is realized by using the Lagrange interpolation technique in Green's function when the source and observation cubes are well separated. Applying the MLGFIM to the

low-ranked impedance matrix will result in significant memory reduction and computational time savings. For this, a cube tree is first needed to construct. We first enclose the entire object in a large cube, and then the cube is partitioned into eight smaller cubes. Each subcube is recursively subdivided into eight smaller cubes until the finest cubes satisfy the termination criterion. For MLFMM, the finest cube size is about half a wavelength. After constructing a tree, numerical operations can be performed on it. Two cubes are well separated if the ratio of the cube-center-distance to the cube size is greater than or equal 2. The impedance matrix between them is low-ranked. Otherwise, they are near each other, share at least one edge point, and the impedance matrix is full-ranked. This will cost a lot of CPU time and memory for the near-field computation if the number of unknowns contained in every cube is large. By the MLGFIM technique in the near-field computation, we can continue to subdivide the cube tree until the number of unknowns in each cube is less than or equal to a given number which is a parameter to control the tree depth. Therefore, the number of basis functions contained in every cube is reduced a lot, the MoM for the near-field computation is reduced; part of the near-field in MLFMM now can be computed by MLGFIM. In order to explain the implementation of the MLGFIM in the near-field computation in the MLFMM clearly, a brief description of its workflow is presented in the following.

As a simple example, a PEC plate is considered as shown in Fig. 1; it is a 1 λ wide square plate. With MLFMM, a 2-level division is used. The finest cube size is 0.25 λ, the line-filled cubes are the neighbors of cube 5, and the interaction between them is computed by MoM and stored in memory. The other cubes are the far-field of cube 5, the interaction between them is computed by the MLFMM. With the MLGFIM in the near-field computation, the cubes at level-2 are subdivided into cubes at level-3. Therefore the number of basis functions contained in every cube at level-3 reduced to about one-fourth of the original compared with the cube at level-2. Cube 5 at level-2 is the parent of cube 6 at level-3, with the MLFMM all the line-filled and the darkened cubes at level-3 are the near-field of cube 5 at level-2. While with MLGFIM at level-3, the interaction between the Cube 6, and the darkened cubes are computed by MoM; the interaction between the Cube 6 and the line-filled cubes are computed by MLGFIM. Therefore, the total near-field computation in the MLFMM is decomposed into two parts by using MLGFIM. One part of the near-field is computed directly by the MoM, the other is computed by MLGFIM. From above, we know that the MLGFIM is a rank-based method; applying the MLGFIM to the low-ranked impedance matrix will result in significant memory reduction and saves computing time. Therefore, the total near-field memory requirement is reduced in MLFMM.

B. Lagrange interpolation technique in the Green's function

The rank-deficiency of the proposed method is realized by the interpolation of the Green's function technique. Therefore, the accuracy analysis of the Green function interpolation technique is very important. From [11], it can be seen that for static problems or problems having small electric sizes, the number of interpolation points K in every cube keeping constant at all levels can keep the accuracy across all levels of a cluster tree. However, for full-wave problems, the use of constant rank cannot keep the accuracy to the same order when the size of the cube increases. This can be analyzed as below.

In MLFMM, we known that the lower the tree is, the larger the cube size is. The phase of the Green's function oscillates rapidly when the separation between the cubes increases. Obviously to accurately compute the Green's function between two points in two well separated cubes, the number of interpolation points should be increased when the frequency increases or when the sizes of the cubes increase. Consequently, to employ the MLGFIM to the full-wave problem, K should be replaced by K_l, in which subscript l denotes the level index. K_l means the number of interpolation points in every cube at level l. Since increasing frequency is equivalent to increasing the tree depth, in order to keep the same order of the accuracy across all tree levels, the interpolation points K_l should be increased when the size of the cubes increase. From paper [12], we observe that when the electric sizes of the cubes are smaller than 0.2λ, for each variable, only 3 points are used as the interpolation points, a total of 27 interpolation points in a cube are sufficient to get a higher accuracy. While the size of the cube

increases to 2 λ, to constrain the error to 0.0135, 1000 interpolation points should be used, a large number that will drastically reduce the efficiency of the MLGFIM. Hence in this paper, the Green's function interpolation technique is just used in the near-field computation where the electric size of the cube is small. Few interpolation points can get a higher accuracy and efficiency. The accuracy and efficiency retains the same in a wide range when the electric size of the cube is smaller than 0.2 λ;

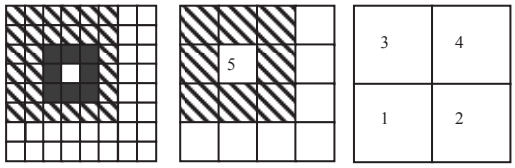

Fig. 1. A three level octree structure.

C. Lower-to-upper level interpolation

The MLGFIM is used in this paper to calculate part of the near-field defined in equation (5). Therefore, the near-field part in (5) can be written as the following form:

$$\bar{\bar{Z}}_{NF}\bar{x}=\sum_{l=L}^{1}\bar{\pi}_l+\bar{\bar{Z}}_{NF_L}\bar{x} \tag{11}$$

In (11), the term $\bar{\bar{Z}}_{NF}$ denotes the total near-field in the MLFMM which are calculated by MoM. The first term $\bar{\bar{Z}}_{NF_L}$ denotes part of the near-field in MLFMM which is calculated by MoM at the finest level of the MLFMM-MLGFIM, the second term $\sum_{l=L}^{1}\bar{\pi}_l$ is part of the near-field which is calculated by the MLGFIM. These two terms combined together form the total near-field in MLFMM. L is the number of levels which the MLGFIM technique is used for computing the near-field , The core in MLGFIM is to calculate the second term defined in equation (11). According to the tree structure used in MLFMM-MLGFIM, the near-field $\bar{\bar{Z}}_{NF_L}$ in (11) can be expressed as

$$\bar{\bar{Z}}_{NF_L}=\sum_{\substack{G_{n_L,L}\in \\ Neighbors \\ \text{of } G_{m_L,L}}}(\bar{\bar{Z}}_{m_L,L;n_L,L}\cdot\bar{x}_{n_L,L}) \tag{12-a}$$

$$\bar{\pi}_l=\sum_{\substack{G_{n_l,l}\in \\ \text{Interaction List} \\ \text{of } G_{m_l,l}}}\ \sum_{\substack{G_{n_{l+1},l+1}\subset \\ G_{n_l,l}}}\cdots\sum_{\substack{G_{n_L,L}\subset \\ G_{n_{L-1},L-1}}}\bar{\bar{A}}_{m_L,L;n_L,L}\cdot\bar{x}_{n_L,L} \tag{12-b}$$

The term $\bar{\bar{A}}_{m_L,L;n_L,L}$ in (12-b) can be written as the following for

$$\bar{\bar{A}}_{m_L,L;n_L,L}=\bar{\bar{W}}_{m_L,L}\cdot\bar{\bar{G}}_{m_L,L;n_L,L}\cdot\bar{\bar{W}}^{T}_{n_L,L} \tag{13}$$

For two well-separated cubes $G_{m_{L-1},L-1}$ and $G_{n_{L-1},L-1}$ at level $L-1$, cube $G_{m_L,L}$ is the child of cube $G_{m_{L-1},L-1}$ and cube $G_{n_L,L}$ is the child of cube $G_{n_{L-1},L-1}$, the Green's function matrix $\bar{\bar{G}}_{m_L,L;n_L,L}$ can be interpolated using the interpolation matrix $\bar{\bar{G}}_{m_{L-1},L-1;n_{L-1},L-1}$.

$$\bar{\bar{G}}_{m_L,L;n_L,L}=\bar{\bar{C}}^{T}_{m_{L-1},L-1;m_L,L}\cdot\bar{\bar{G}}_{m_{L-1},L-1;n_{L-1},L-1}\cdot\bar{\bar{C}}_{n_{L-1},L-1;n_L,L} \tag{14}$$

$\bar{\bar{C}}_{n_{L-1},L-1;n_L,L}$ is the lower-to-upper interpolation matrix defined in [11], performing the Green's function interpolation recursively, (14) becomes

$$\bar{\bar{G}}_{m_L,L;n_L,L}=\bar{\bar{C}}^{T}_{m_{L-1},L-1;m_L,L}\cdots\bar{\bar{C}}^{T}_{m_l,l;m_{l+1},l+1}\cdot\bar{\bar{G}}_{m_l,l;n_l,l}\cdot\bar{\bar{C}}_{n_l,l;n_{l+1},l}\cdots\bar{\bar{C}}_{n_{L-1},L-1;n_L,L} \tag{15}$$

Substituting (15) and (13) into (12-b) gives (16)

Let

$$\bar{S}_{n_L,L}=\bar{\bar{W}}^{T}_{n_L,L}\cdot\bar{x}_{n_L,L}\quad\text{and}$$

$$\bar{S}_{n_l,l}=\sum_{G_{n_{l+1},l+1}\subset G_{n_l,l}}\bar{\bar{C}}_{n_l,l;n_{l+1},l}\cdot\bar{S}_{n_{l+1},l+1} \tag{17}$$

$\bar{S}_{n_l,l}$ here is just a symbol for recurrence without any means, Hence (16) can be rewritten as

$$\bar{\pi}_l=\bar{\bar{W}}_{m_L,L}\cdot\bar{\bar{C}}^{T}_{m_{L-1},L-1;m_L,L}\cdots\bar{\bar{C}}^{T}_{m_l,l;m_{l+1},l+1}\cdot\sum_{\substack{G_{n_l,l}\in\text{Interaction} \\ \text{List of } G_{m_l,l}}}\bar{\bar{G}}_{m_l,l;n_l,l}\cdot\bar{S}_{n_l,l} \tag{18}$$

Let

$$\bar{\alpha}_{m_l,l}=\sum_{\substack{G_{n_l,l}\in\text{Interaction} \\ \text{List of } G_{m_l,l}}}\bar{\bar{G}}_{m_l,l;n_l,l}\cdot\bar{S}_{n_l,l} \tag{19}$$

Hence

$$\bar{\pi}_l=\bar{\bar{W}}_{m_L,L}\cdot\bar{\bar{C}}^{T}_{m_{L-1},L-1;m_L,L}\cdots\bar{\bar{C}}^{T}_{m_l,l;m_{l+1},l+1}\cdot\bar{\alpha}_{m_l,l} \tag{20}$$

Substituting (20) into (11) and let

$$\bar{B}_{m_l,l} = \bar{\alpha}_{m_l,l} + \bar{\bar{C}}^{T}_{m_{l-1},l-1;m_l,l} \cdot \bar{B}_{m_{l-1},l-1} \ , \ \bar{B}_{m_1,1} = \bar{\alpha}_{m_1,1} \quad (21)$$

Substituting (21) into (20) recursively gives (22).

Hence the formula for MLGFIM algorithm is derived, what we want is to compute $\bar{B}_{m_L,L}$, which can be obtained using recurrence (22) from the top level to the finest level of the cluster tree. At the top level of the MLGFIM $\bar{B}_{m_1,1} = \bar{\alpha}_{m_1,1}$ is obtained using (22) from the finest level to the top level of the tree. Thus the procedure of the MVP of MLGFIM is similar to the MVP of MLFMM. (17) Is similar to the procedure in upward pass of MLFMM, (19) is similar to the procedure of shifting phase of MLFMM and (22) is similar to the procedure in downward pass of MLFMM. The difference is that our method uses Green's function interpolation instead of multipole expansion in each step. Equation (15) indicates that the Lagrange interpolation matrix of a cube can be interpolated using the Lagrange interpolation matrix of its child. For any other non-leaf cluster, we can directly use the contribution from its eight sons to obtain the result of MVP without any additional operations. This property is an important factor that enables us to reduce the complexity of MLGFIM.

$$\begin{aligned}
\bar{\Pi} &= \bar{\bar{W}}_{m_L,L} \cdot (\bar{\alpha}_{m_L,L} + \bar{\bar{C}}^{T}_{m_{L-1},L-1;m_L,L} \cdot (\bar{\alpha}_{m_{L-1},L-1} + \cdots + \bar{\bar{C}}^{T}_{m_l,l;m_{l+1},l+1} \cdot \\
&(\bar{\alpha}_{m_{l+1},l+1} + \bar{\bar{C}}^{T}_{m_l,l;m_l+1,l+1} \cdot (\bar{\alpha}_{m_l,l} \cdots + \bar{\bar{C}}^{T}_{m_2,2;m_3,3} \cdot (\bar{\alpha}_{m_2,2} + \bar{\bar{C}}^{T}_{ml,1;m2,2} \cdot \bar{\alpha}_{m_1,1}))))) \\
&= \bar{\bar{W}}_{m_L,L} \cdot (\bar{\alpha}_{m_L,L} + \bar{\bar{C}}^{T}_{m_{L-1},L-1;m_L,L} \cdot (\bar{\alpha}_{m_{L-1},L-1} + \cdots + \bar{\bar{C}}^{T}_{m_l,l;m_{l+1},l+1} \cdot \\
&(\bar{\alpha}_{m_{l+1},l+1} + \bar{\bar{C}}^{T}_{m_l,l;m_l+1,l+1} \cdot (\bar{\alpha}_{m_l,l} \cdots + \bar{\bar{C}}^{T}_{m_2,2;m_3,3} \cdot (\bar{\alpha}_{m_2,2} + \bar{\bar{C}}^{T}_{ml,1;m2,2} \cdot \bar{B}_{m_1,1}))))) \\
&= \bar{\bar{W}}_{m_L,L} \cdot (\bar{\alpha}_{m_L,L} + \bar{\bar{C}}^{T}_{m_{L-1},L-1;m_L,L} \cdot (\bar{\alpha}_{m_{L-1},L-1} + \cdots + \bar{\bar{C}}^{T}_{m_l,l;m_{l+1},l+1} \cdot \\
&(\bar{\alpha}_{m_{l+1},l+1} + \bar{\bar{C}}^{T}_{m_l,l;m_l+1,l+1} \cdot (\bar{\alpha}_{m_l,l} \cdots + \bar{\bar{C}}^{T}_{m_2,2;m_3,3} \cdot \bar{B}_{m_2,2})))) \\
&\cdots \\
&= \bar{\bar{W}}_{m_L,L} \cdot \bar{B}_{m_L,L}
\end{aligned} \quad (22)$$

D. Compression of the Green's function matrices using ACA, QR factorization, SVD

For any two well-separated cubes *m* and *n* at the same level, the Green's function matrix $G(r_m, r_n)$ is a $K \times K$ full matrix. Since, the Green's function matrix represents interactions between the interpolation points of two well-separated cubes, it is low rank. In order to reduce the computational complexity of MLGFIM, the ACA [13-14], QR factorization [15-16], and SVD, are used to compress the Green's function matrix as data sparse representation, which brings a great advantage in the MVP operation $\bar{\bar{G}}_{m_l,l;n_l,l} \cdot \bar{S}_{n_l,l}$.

Let the $K \times K$ rectangular matrix $G(r_m, r_n)$ represent the interactions between the interpolation points of two well-separated cubes m and n, the ACA allows the low rank Green's function matrix $G(r_m, r_n)$ to be represented by only a few rows and columns of $G(r_m, r_n)$ to obtain the numerical representation from namely,

$$\tilde{G}^{K\times K} = A^{K\times r}(B^{K\times r})^{H} \quad (23)$$

where the number of terms r is much less than K, $A^{K\times r}$ and $B^{K\times r}$ are two dense rectangular matrices. The goal of the ACA is to achieve $\left\|R^{K\times K}\right\| = \left\|G^{K\times K} - \tilde{G}^{K\times K}\right\| \le \varepsilon \left\|G^{K\times K}\right\|$ for a given tolerance ε, where R is termed as the error matrix. $\|.\|$ refer to the matrix Frobenus norm. If $r \ll \min(m,n)$, then a significant reduction in MVP can be accomplished. For the matrix U and V, we can continue to use QR decomposition technique to compress it

$$A^{K\times r} = Q_1^{K\times r} R_1^{r\times r} \quad (24\text{-}1)$$

$$B^{K\times r} = Q_2^{K\times r} R_2^{r\times r} \quad (24\text{-}2)$$

Then, the matrix $\tilde{G}^{K\times K}$ can be expressed as the following form

$$\begin{aligned}
\tilde{G}^{K\times K} &= A^{K\times r}(B^{r\times r})^{H} = Q_1^{K\times r} R_1^{r\times r} (Q_2^{K\times r} R_2^{r\times r})^{H} \\
&= Q_1^{K\times r} R_1^{r\times r} (R_2^{r\times r})^{H} (Q_2^{K\times r})^{H}
\end{aligned} \quad (25)$$

Here, we let $W^{r\times r} = R_1^{r\times r}(R_2^{r\times r})^{H}$, using singular value decomposition (SVD),

$$W^{r\times r} = U^{r\times r} S^{r\times r} V^{r\times r} \quad (26)$$

where U and V are orthonormal matrices, and S is the diagonal matrix whose elements are the nonnegligible singular values of $W^{r\times r}$, it can be written as $S = diag(\sigma_1, \sigma_2, \sigma_3 \ldots, \sigma_r)$. We discard those normalized values which fall below the threshold; typically chosen threshold to be 10^{-3}, the columns of U and V corresponding to negligible singular values of S are discarded. Then, the matrix $\tilde{G}^{K\times K}$ can be written as the following

$$\begin{aligned}
\tilde{G}^{K\times K} &= Q_1^{K\times r} R_1^{r\times r} (R_2^{r\times r})^{H} (Q_2^{K\times r})^{H} \\
&\cong Q_1^{K\times r} U^{r\times r1} S^{r1\times r1} V^{r1\times r} (Q_2^{K\times r})^{H}
\end{aligned} \quad (27)$$

Let

$$A^{K\times r1} = Q_1^{K\times r} R_1^{r\times r1} S^{r1\times r1} \text{ and } B^{r1\times K} = V^{r1\times r}(Q_2^{K\times r})^H$$

then

$$\widetilde{G}^{K\times K} = A^{K\times r1} \times B^{r1\times K} \tag{28}$$

Usually the compressed matrices rank $r1$ is much smaller than the number of interpolation points K. This brings a great advantage in the MVP because

$$\overline{\overline{G}}^{K\times K} \cdot \overline{S}^K = A^{K\times r1} \times B^{r1\times K} \cdot \overline{S}^K \tag{29}$$

When $r1 << K$, to calculate $A^{K\times r1} \times B^{r1\times K} \cdot \overline{S}^K$ is much faster than to calculate $\overline{\overline{G}}^{K\times K} \cdot \overline{S^K}$. Table 1 lists the corresponding average numerical ranks of Green's function matrices with different sizes of the cube. We can see that the corresponding numerical ranks are very small. Thus, a high compression of the Green's function matrices is obtained.

III. NUMERICAL RESULTS

In this section, three examples are presented to demonstrate the benefits of the proposed method. All the simulations are performed on a computer with 2.8GHz CPU and 2 GB RAM. The terminating tolerances of the ACA and SVD are set as $\varepsilon = 0.001$ and $\sigma = 0.001$, respectively. The resulting linear systems are solved iteratively by the GMRES (30) solver with a relative residual of 10^{-3}.

First, the proposed method is used to analyse scattering from a PEC sphere of radius 0.5 λ, its surface is discretized with 6312, 11649, and 25944 unknowns, respectively. The finest cube size is 0.25 λ in MLFMM, two-level MLGFIM are added to calculate part of the near-field of the MLFMM. The finest cube size is 0.0625 λ in MLFMM-MLGFIM. Figure 2 shows the bistatic radar cross-section (RCS) results obtained from the MIE series and the MLFMM-MLGFIM. It can be seen from Fig. 2, that the result from the MLFMM-MLGFIM has good agreement with the MIE series. Table II lists the near-field memory requirement, the matrix filling time and MVP time of MLFMM and MLFMM-MLGFIM for different discretizations. The time and memory requirement in computing the near-field impedance matrix in MLFMM-MLGFIM includes two parts. The first part denotes the time and memory requirement in computing the part of the near-field matrix by MoM, while the second part denotes the time and memory requirement in computing part of the near-field matrix by MLGFIM. It can be seen from Table 2 that the memory requirement and filling time of the near-field matrix in MLFMM-MLGFIM is significantly reduced as the number of unknowns increases compared with MLFMM.

The second example is a PEC ogive, whose length and maximum radius is 2λ and 0.5 λ. The ogive is discretized with 11874 and 18876 unknowns, respectively. 1-level MLGFIM is added to calculate part of the near-field interaction when the number of unknowns is 11874, the finest cube size is 0.125 λ. 2-level MLGFIM is added to calculate part of the near-field interaction when the number of unknowns is 18876, the finest cube size is 0.0625 λ. Figure 3 is the bistatic RCS of the ogive computed by MLFMM and MLFMM-MLGFIM. It can be seen from Fig. 3 that the proposed method agrees well with the MLFMM results. Table 3 lists the near-field memory requirement, the near-filed impedance matrix filling time, and the MVP time needed by MLFMM-MLGFIM and MLFMM for different discretizations. It can be seen from Table 3 that the memory requirement by the MLFMM-MLGFIM can be saved by a factor of 4.1 with one-level MLGFIM when the number of unknowns is 11874. The flaw for the MLFMM-MLGFIM is that the MVP time is 1.9 while the MLFMM is 1.07s. The near-filed matrix filling time and memory requirement can be saved by a factor of 16.8 and 14.2 with two-level MLGFIM when the number of unknowns is 18876. Again, it can be seen that the MLFMM-MLGFIM can greatly reduce the near-filed memory requirement and the matrix filling time compared with MLFMM.

The last example is a VIAS structure as shown in Fig.4, the electric size of the VIAS structure is $1.2\lambda \times 1\lambda \times 1\lambda$, it is discretized with 10609 and 15305 unknowns, respectively. For MLFMM, a 2-level division is used since the finest cube size is 0.30 λ. For MLFMM-MLGFIM, a 4-level division is used. The finest cube size is 0.075 λ. A 2-level MLGFIM is added to calculate part of the near-field interaction. Good agreement is achieved as shown in Fig. 4. Table 4 lists the comparison of the near-field memory requirement, the near-filed matrix filling time, and the MVP time between the MLFMM-MLGFIM and MLFMM for the two above discretizations. It can be found that the MLGFIM can extremely decrease the near-filed

matrix filling time when compared with MLFMM, MLFMM-MLGFIM can save much of the memory requirement by a factor of 9.9 with 10609 unknowns and 10.3 with 15305 unknowns for the near-field. When the number of unknowns is 15305, the MVP time in each iteration step in the MLFMM-MLGFIM is less than that in MLFMM. This is because the number of elements in the near-field impendence matrix is greatly reduced by the MLGFIM. The result of Table 4 indicates again that the matrix filing time and memory requirement can be greatly reduced with the MLGFIM in MLFMM in the near-field computation.

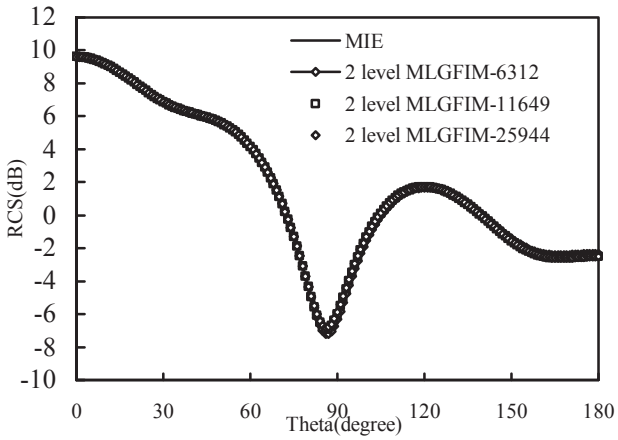

Fig. 2. RCS of a PEC sphere obtained from the MIE series and the MLFMM-MLGFIM.

IV. CONCLUSIONS

In this paper, the MLGFIM is introduced in MLFMM to solve electromagnetic scattering problems of the objects with fine structures. It is found that with MLGFIM we can continue to subdivide the cube until the number of unknowns in each cube is less or equal to a required number regardless of the cube size. Several examples have demonstrated that with MLGFIM the near-field memory requirement is greatly reduced in MLFMM-MLGFIM compared with MLFMM without compromising the accuracy. Moreover, the ACA, QR factorization, SVD are applied to compress the low rank Green's function matrix for speeding up the MVP in MLFMM-MLGFIM. Therefore, the MLGFIM is an efficient augment for MLFMM.

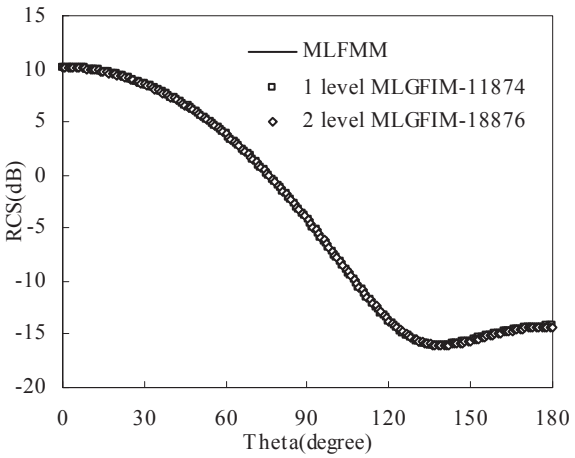

Fig. 3. The bistatic RCS from MLFMM and MLFMM-MLGFIM for the PEC ogive example.

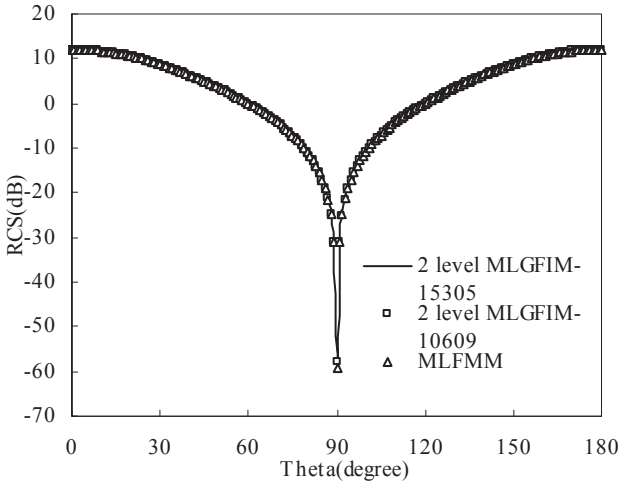

Fig. 4. RCS of a VIAS structure obtained from MLFMM and MLFMM-MLGFIM.

ACKNOWLEDGMENT

The authors would like to thank the support of National Key Laboratory Foundation of China (No: 9140C5305021006).

$$\begin{aligned}\overline{\overline{\pi}}_l &= \sum_{\substack{G_{n_l,l}\in\text{Interaction}\\ \text{List of } G_{m_l,l}}} \sum_{\substack{G_{n_{l+1},l+1}\\ \subset G_{n_l,l}}} \cdots \sum_{\substack{G_{n_L,L}\\ \subset G_{n_{L-1},L-1}}} \overline{\overline{W}}_{m_L,L}\cdot\overline{\overline{G}}_{m_L,L;n_L,L}\cdot\overline{\overline{W}}^T_{n_L,L}\cdot\overline{x}_{n_L,L} \\ &= \sum_{\substack{G_{n_l,l}\in\text{Interaction}\\ \text{List of } G_{m_l,l}}} \sum_{\substack{G_{n_{l+1},l+1}\\ \subset G_{n_l,l}}} \cdots \sum_{\substack{G_{n_L,L}\\ \subset G_{n_{L-1},L-1}}} \overline{\overline{W}}_{m_L,L}\cdot\overline{\overline{C}}^T_{m_{L-1},L-1;m_L,L}\cdots\overline{\overline{C}}^T_{m_l,l;m_{l+1},l+1}\cdot\overline{\overline{G}}_{m_l,l;n_l,l}\cdot\overline{\overline{C}}_{n_l,l;n_{l+1},l}\cdots\overline{\overline{C}}_{n_{L-1},L-1;n_L,L}\cdot\overline{\overline{W}}^T_{n_L,L}\cdot\overline{x}_{n_L,L} \\ &= \overline{\overline{W}}_{m_L,L}\cdot\overline{\overline{C}}^T_{m_{L-1},L-1;m_L,L}\cdots\overline{\overline{C}}^T_{m_l,l;m_{l+1},l+1}\cdot\sum_{\substack{G_{n_l,l}\in\text{Interaction}\\ \text{List of } G_{m_l,l}}}\overline{\overline{G}}_{m_l,l;n_l,l}\cdot\sum_{\substack{G_{n_{l+1},l+1}\\ \subset G_{n_l,l}}}\overline{\overline{C}}_{n_l,l;n_{l+1},l}\cdots\sum_{\substack{G_{n_L,L}\\ \subset G_{n_{L-1},L-1}}}\overline{\overline{C}}_{n_{L-1},L-1;n_L,L}\cdot\overline{\overline{W}}^T_{n_L,L}\cdot\overline{x}_{n_L,L}\end{aligned} \tag{16}$$

Table 1: Corresponding rank of the Green's function with different size of the cube

Cube size		d=1.0	d=0.5	d=0.25	d=0.125
Interpolation points		8×8×8	6×6×6	4×4×4	3×3×3
# of entries in G		262144	47524	4096	729
Threshold $\varepsilon = 0.01$ $\sigma = 0.01$	Numerical rank	11	6	5	4
	# of entries in Q and R	11264	2616	640	216
Threshold $\varepsilon = 0.01$ $\sigma = 0.001$	Numerical rank	17	11	9	8
	# of entries in Q and R	17408	4752	1152	432
Threshold $\varepsilon = 0.001$ $\sigma = 0.01$	Numerical rank	11	8	5	4
	# of entries in Q and R	11264	3456	640	216
Threshold $\varepsilon = 0.001$ $\sigma = 0.001$	Numerical rank	17	12	9	8
	# of entries in Q and R	17408	5184	1152	432

Table 2: The near-field memory, the matrix filling time and one MVP time of MLFMM、MLFMM-MLGFIM for different numbers of unknowns

Unknowns	Methods	CPU time for Matrix filling	CPU time for each MVP	Memory
6312	MLFMM	35.2 s	0.22 s	70 Mb
	MLFMM-MLGFIM	2.1 s+0.57 s	3.65 s	4.1 Mb+ 2.5 Mb
11649	MLFMM	124.3 s	0.81 s	240 Mb
	MLFMM-MLGFIM	6.9 s+0.96 s	3.9 s	14 Mb+ 4.7 Mb
25944	MLFMM	641.1 s	3.1 s	1191 Mb
	MLFMM-MLGFIM	32.5s+2.0 s	4.4 s	69 Mb+ 10 Mb

Table 3: The near-field memory, the matrix filling time and one MVP time of MLFMA、MLFMM-MLGFIM for different numbers of unknowns

Unknowns	level	Methods	CPU time for Matrix filling	CPU time for each MVP	Memory
11874	3	MLFMM	206.9s	1.07s	404Mb
	4	MLFMM-MLGFIM	46.5s+0.32s	1.9s	89Mb + 9Mb
18876	3	MLFMM	533.5s	2.5s	1019 Mb
	5	MLFMM-MLGFIM	31.2s+0.56s	2.9s	56 Mb + 15.5 Mb

Table 4: The near-field memory, the matrix filling time and one MVP time of MLFMA, MLFMM-MLGFIM for different numbers of unknowns

Unknowns	level	Methods	CPU time for Matrix filling	CPU time for each MVP	Memory
10609	2	MLFMM	214.2s	1s	388Mb
	4	MLFMM-MLGFIM	20.9s+0.33s	1.48s	35Mb + 4 Mb
15305	2	MLFMM	451.4s	2.04s	805Mb
	4	MLFMM-MLGFIM	42s+0.43s	1.59s	72Mb+6Mb

REFERENCES

[1] S. M. Rao, D. R. Wilton, and A. W. Glisson, "Electromagnetic Scattering by Surfaces of Arbitrary Shape," *IEEE Trans. Antennas and Propag*., vol. 30, no. 3, pp. 409-418, May. 1982.

[2] B. J. Fasenfest, F. Capolino, and D. R. Wilton, "Preconditioned GIFFT: A Fast MoM Solver for Large Arrays of Printed Antennas,"*ACES Journal*, vol.21, no.3, pp. 276-283, November. 2006.

[3] J. M. Song and W. C. Chew, "Fast Multipole Method Solution using Parametric Geometry," *Microwave and Optical Technology Letters*, vol. 7, no. 16, pp. 760-765,1994.

[4] C. Guo and T. H. Hubing, "Development and Application of a Fast Multipole Method in a Hybrid FEM/MoM Field Solver," *Applied Computational Electromagnetic Society (ACES) Journal*, vol. 19, no. 3, pp. 126- 134, November 2004.

[5] R. Coifman, V. Rokhlin, and S. M. Wandzura, "The Fast Multipole Method for the Wave Equation: A Pedestrian Prescription," *IEEE Trans. Antennas and Propag., Mag*, vol. 35, no. 3, pp. 7–12, Jun. 1993.

[6] J. M. Song, C. C. Lu., and W .C. Chew, "Multilevel Fast Multipole Algorithm for Electromagnetic Scattering by Large Complex Objects," *IEEE Trans. Antennas and Propag.*, 45(10), pp. 1488-1493, 1997.

[7] C. C. Lu and W. C. Chew, "A Multilevel Algorithm for Solving Boundary Integral Equations of Wave Scattering," *Microwave and Optical Technology Letters*, vol. 7, pp. 466-470, July 1994.

[8] J. M. Song, and W. C. Chew, "Multilevel Fast-Multipole Algorithm for Solving Combined Field Integral Equation of Electromagnetic Scattering," *Microwave and Optical Technology Letters*, vol. 10, pp. 14-19, Sept. 1995.

[9] H. Zhao, J. Hu, and Z. Nie, "Parallelization of MLFMA with Composite Load Partition Criteria and Asynchronous Communication," *Applied Computational Electromagnetic Society (ACES) Journal*, vol. 25, no. 2, pp. 167-173, February 2010.

[10] H. Fangjing, N. Zaiping, and H. Jun, "An Efficient Parallel Multilevel Fast Multipole Algorithm for Large-scale Scattering Problems," *Applied Computational Electromagnetic Society (ACES) Journal*, vol. 25, no. 4, pp. 381-387, April 2010.

[11] H. G. Wang, C. H. Chan, and L. Tsang, "A New Multilevel Green's Function Interpolation Method for Large-Scale Low-Frequency EM Simulations," *IEEE Trans. On Computer-Aided Design of Integrated Circuits and Systems*, vol. 24, no. 9, pp. 1427-1443, Sept. 2005.

[12] H. G. Wang and C. H. Chan, "The Implementation of Multilevel Green's Function Interpolation Method for Full-Wave Electromagnetic Problems," *IEEE Trans. Antennas and Propag.*, vol. 55, no. 5, pp. 1348-1358, May 2007.

[13] L. Li, H. G. Wang, and C. H. Chan, "An Improved Multilevel Green's Function Interpolation Method with Adaptive Phase Compensation," *IEEE Trans. Antennas and Propag.*, vol. 56, no. 5, pp. 1381-1393, May 2008.

[14] Y. Shi, H. G. Wang, L. Li, and C. H. Chan, "Multilevel Green's Function Interpolation Method for Scattering from Composite Metallic and Dielectric Objects," *J. Opt. Soc. Am. A*, vol. 25, no. 10, pp. 2535-2548, October 2008.

[15] W. Chai and D. Jiao, "An H2-Matrix-Based Integral-Equation Solver of Linear-Complexity for Large-Scale Electromagnetic Analysis," *2008 Asia Pacific Microwave Conference*, 4 pages, Dec. 2008.

[16] W. Chai and D. Jiao, "An H2-Matrix-Based Integral-Equation Solver of Reduced Complexity and Controlled Accuracy for Solving Electrodynamic Problems," *IEEE Trans. Antennas and Propag.*, vol. 57, no. 5, pp. 3147-3159, Oct. 2009.

[17] L. J. Jiang, W. C. Chew, "A Mixed-Form Fast Multipole Algorithm," *IEEE Trans. Antennas and Propag.*, vol. 53, no. 12, pp. 4145-4156, Dec. 2005.

[18] K. Zhao, M. N. Vouvakis, and J.-F. Lee, "Application of the Multilevel Adaptive Cross-Approximation on Ground Plane Designs," *IEEE Int. Symp. Electromagnetic Compatibility*, Santa Clara, CA, pp. 124–127, 2004.

[19] J. W. Daniel, W. B. Gragg, L. Kaufman, and G. W. Stewart, "Reorthogonalization and

Stable Algorithms for Updating the Gram-Schmidt QR Factorization," *Math. Comp*, vol. 30, pp. 772–795, 1976.

Ming Chen was born in Anhui, China. He received the B.S. degree in Physics from Anhui University in 2006, and is currently working toward the Ph.D. degree at Nanjing University of Science and Technology (NJUST), Nanjing, China. His current research interests include computational electromagnetics, antennas, and electromagnetic scattering and propagation.

Ru-Shan Chen was born in Jiangsu, P. R. China. He received his B.Sc. and M.Sc. degrees from the Dept. of Radio Engineering, Southeast University, in 1987 and in 1990, respectively, and his Ph.D. from the Dept. of Electronic Engineering, City University of Hong Kong in 2001. He became a Teaching Assistant in 1990 and a Lecturer in 1992. Since September 1996, he has been a Visiting Scholar with the Department of Electronic Engineering, City University of Hong Kong, first as Research Associate, then as a Senior Research Associate in July 1997, a Research Fellow in April 1998, and a Senior Research Fellow in 1999. From June to September 1999, he was also a Visiting Scholar at Montreal University, Canada. In September 1999, he was promoted to Full Professor and Associate Director of the Microwave & Communication Research Center in NJUST and in 2007, he was appointed Head of the Dept of Communication Engineering, Nanjing University of Science & Technology. His research interests include microwave and millimeter-wave systems, measurements, antenna, RF-integrated circuits, and computational electromagnetics. He is a Senior Member of the Chinese Institute of Electronics (CIE). He received the 1992 third-class science and technology advance prize given by the National Military Industry Department of China, the 1993 third class science and technology advance prize given by the National Education Committee of China, the 1996 second-class science and technology advance prize given by the National Education Committee of China, and the 1999 first-class science and technology advance prize given by JiangSu Province as well as the 2001 second-class science and technology advance prize. At NUST, he was awarded the Excellent Honor Prize for academic achievement in 1994, 1996, 1997, 1999, 2000, 2001, 2002, and 2003. He has authored or co-authored more than 200 papers, including over 140 papers in international journals. He is the recipient of the Foundation for China Distinguished Young Investigators presented by the National Science Foundation (NSF) of China in 2003. In 2008, he became a Chang-Jiang Professor under the Cheung Kong Scholar Program awarded by the Ministry of Education, China.

Xiaoqing Hu was born in Hubei, China, in June 1981. He received the B.S. degree and M.S. degree in Applied Mathematics from Jilin University, Jilin, China, in 2004 and 2007, respectively. He is currently working toward the Ph.D. degree at Nanjing University of Science and Technology, Jiangsu, China. His research interests include integral equation and its fast methods.

Transient Analysis of Electromagnetic Scattering using Marching-on-in-Order Time-Domain Integral Equation Method with Curvilinear RWG Basis Functions

Quan-quan Wang, Chao Yan, Yi-fei Shi, Da-zhi Ding, and Ru-shan Chen

Department of Communication Engineering
Nanjing University of Science and Technology, Nanjing 210094, Jiangsu, China
eeqqwang@gmail.com, eechenrs@mail.njust.edu.cn

Abstract ─ In this paper, a modified marching-on-in-order time-domain integral equation method is utilized to analyze transient electromagnetic scattering from arbitrarily shaped objects. The spatial and temporal testing procedures are separate, and both of them are performed with the Galerkin's method. The curvilinear RWG basis functions are used as spatial basis functions with curved triangular patch modeling. It gives a remarkable reduction to the number of unknowns, also the memory requirement and CPU time, without sacrificing the accuracy. The use of the weighted Laguerre polynomials as temporal basis functions ensures an absolutely stable solution even in late time. Several numerical results, including the single ogive and NASA almond, are given to demonstrate the accuracy and efficiency of the proposed method.

Index Terms ─ Curvilinear RWG basis functions, Laguerre polynomials, marching-on-in-order time-domain integral equation, transient scattering.

I. INTRODUCTION

Accurate and efficient transient simulation has drawn great interest in the past decades for its important applications in the ultra wide band (UWB) technology, electromagnetic compatibility (EMC), radar imaging, etc. Numerical techniques in time domain falls mainly within the scope of the finite difference time-domain (FDTD) [1], the time-domain finite element method (TD-FEM) [2], and the time-domain integral equation (TDIE) [3], which can overcome the drawbacks encountered in the partial differential equation (PDE) methods. The most popular method to solve TDIE is the marching-on-in-time (MOT) procedure [4], but it may suffer from late-time oscillation and inaccuracy. Some progresses seem to eliminate the drawback [5, 6].

In the realm of the integral equation method, the RWG basis function defined over the planar triangular patches was proposed to model the behavior of the induced surface current [7, 8]. Afterwards, the curvilinear counterpart with curved triangular patch modeling was developed, and much less unknowns are required without a loss of accuracy [9, 10].

References [11-13] used the curvilinear RWG (CRWG) basis functions and other techniques to analyze transient scattering based on the time-domain magnetic field integral equation (TD-MFIE) with MOT procedure. For closed bodies, because using the time-domain electric field integral equation (TD-EFIE) or TD-MFIE alone would lead to wrong results near the resonant frequencies, the time-domain combined field integral equation (TD-CFIE) is preferred [14].

Recently, the marching-on-in-order (MOO) TDIE solver with weighted Laguerre polynomials as temporal basis functions was introduced, which can obtain unconditionally stable solution [15-18]. In this scheme, accurate results near the resonant frequencies can be ensured with only TD-EFIE or TD-MFIE [18]. However, the conventional MOO TDIE method is not efficient in terms of RAM and CPU time. To circumvent the bottleneck, in this paper CRWG basis functions are utilized with MOO TD-EFIE to analyze the electromagnetic scattering from conducting objects.

This paper is organized as follows. Section II presents the formulation of MOO TD-EFIE and the CRWG basis functions. This is followed, in Section III, by giving several numerical results to demonstrate the accuracy and efficiency of the proposed method. The conclusion is drawn in Section IV.

II. FORMULATION

A. MOO TD-EFIE

With the boundary condition on the surface of the conducting scatterers, the time-domain electric field equation (TD-EFIE) is

$$\mathbf{E}^i(\mathbf{r},t)|_{\tan} = \frac{1}{4\pi}\left[\mu_0 \int \frac{\dot{\mathbf{J}}(\mathbf{r}',t-\Delta t_R)}{R} dS' - \frac{\nabla}{\varepsilon_0}\int_0^{t-\Delta t_R}\int \frac{\nabla'\cdot\mathbf{J}(\mathbf{r}',\tau)}{R} d\tau dS'\right]|_{\tan}, \quad (1)$$

where $\mathbf{E}^i(\mathbf{r},t)$ is the incident electric field, $R = |\mathbf{r}-\mathbf{r}'|$ is the distance between the observation point $\mathbf{r}$ and source point $\mathbf{r}'$, $\Delta t_R = R/c$, $\dot{\mathbf{J}}$ is the first derivative of the electric surface current density $\mathbf{J}$ with respect to time t, c, μ_0, and ε_0 are light speed, permeability, and permittivity in free space, respectively.

$\mathbf{J}$ can be expanded using N spatial basis functions and M temporal basis functions as

$$\mathbf{J}(\mathbf{r},t) = \sum_{n=1}^{N}\left(\sum_{j=0}^{M-1} J_{n,j}\varphi_j(\bar{t})\right)\mathbf{f_n}(\mathbf{r}), \quad (2)$$

and $\mathbf{f_n}(\mathbf{r})$ is the spatial basis function and specifically the CRWG in this paper. $\varphi_j(\bar{t})$ is the temporal basis function, i.e. the weighted Laguerre polynomial, defined as

$$\varphi_j(\bar{t}) \triangleq e^{-st/2} L_j(st), \quad (3)$$

where s is a temporal scaling factor and L_j is the j-th order Laguerre polynomial with the form

$$L_j(t) = \frac{e^t}{j!}\frac{d^j}{dt^j}\left(t^j e^{-t}\right),\ 0 \le t < \infty. \quad (4)$$

The temporal derivative and integration terms in (1) are given as [17]

$$\dot{J}_n(t) = s\sum_{j=0}^{\infty}\left(0.5J_{n,j} + \sum_{k=0}^{j-1} J_{n,k}\right)\varphi_j(\bar{t}) \triangleq s\sum_{j=0}^{\infty} J^D_{n,j}\varphi_j(\bar{t}), \quad (5)$$

$$\int_0^t J_n(\tau)d\tau = \frac{2}{s}\sum_{j=0}^{\infty}\left(J_{n,j} + 2\sum_{k=0}^{j-1} J_{n,k}(-1)^{j+k}\right)\varphi_j(\bar{t}) \triangleq \frac{2}{s}\sum_{j=0}^{\infty} J^I_{n,j}\varphi_j(\bar{t}), \quad (6)$$

After the spatial and temporal testing procedure with the Galerkin's method, for the i-th order case we obtain

$$\left(sA_{mn}0.5J_{n,i} + \frac{2}{s}\Psi_{mn}J_{n,i}\right)e^{\frac{-s\Delta t_R}{2}} = \int_0^{\infty} V_m(t)\varphi_i(\bar{t})dt - \sum_{j=0}^{i-1}\left\{sA_{mn}J^D_{n,j} + \frac{2}{s}\Psi_{mn}J^I_{n,j}\right\}\varphi_{i,j}(s\Delta t_R) - \left[sA_{mn}\sum_{k=0}^{i-1}J_{n,k} + \frac{2}{s}\Psi_{mn}\cdot 2\sum_{k=0}^{i-1}J_{n,k}(-1)^{k+i}\right]e^{\frac{-s\Delta t_R}{2}}, \quad (7)$$

where

$$\varphi_{i,j}(s\Delta t_R) = \varphi_{i-j}(s\Delta t_R) - \varphi_{i-j-1}(s\Delta t_R), \quad (8)$$

$$A_{mn} = \frac{\mu_0}{4\pi}\int \mathbf{f_m}(\mathbf{r})\cdot\int\frac{\mathbf{f_n}(\mathbf{r}')}{R}dS'dS, \quad (9)$$

$$\Psi_{mn} = \frac{1}{4\pi\varepsilon_0}\int\nabla\cdot\mathbf{f_m}(\mathbf{r})\int\frac{\nabla'\cdot\mathbf{f_n}(\mathbf{r}')}{R}dS'dS, \quad (10)$$

$$V_m(t) = \int \mathbf{f_m}(\mathbf{r})\cdot\mathbf{E}^i(\mathbf{r},t)dS. \quad (11)$$

Rewrite (7) into a matrix equation

$$\left[\mathbf{Z}^E{}_{mn}\right]\left[\mathbf{J}_{n,i}\right] = \left[\mathbf{V}^E{}_{m,i}\right] - \left[\mathbf{V}'^E{}_{m,i}\right], \quad (12)$$

where

$$\mathbf{Z}^E{}_{mn} = \left(sA_{mn}0.5 + \frac{2}{s}\Psi_{mn}\right)e^{\frac{-s\Delta t_R}{2}}, \quad (13)$$

$$\mathbf{V}^E{}_{m,i} = \int_0^{\infty} V_m(t)\varphi_i(\bar{t})dt, \quad (14)$$

$$\mathbf{V}'^E{}_{m,i} = \sum_{j=0}^{i-1}\left\{sA_{mn}J^D_{n,j} + \frac{2}{s}\Psi_{mn}J^I_{n,j}\right\}\varphi_{i,j}(s\Delta t_R) + \left[sA_{mn}\sum_{k=0}^{i-1}J_{n,k} + \frac{2}{s}\Psi_{mn}\cdot 2\sum_{k=0}^{i-1}J_{n,k}(-1)^{k+i}\right]e^{\frac{-s\Delta t_R}{2}}. \quad (15)$$

We can solve the matrix equation recursively to get the temporal coefficients order by order. Then the surface current density can be obtained from (2).

B. CRWG basis function

The CRWG basis functions are defined over curved triangular patches. Compared with planar triangular patches, the curved ones give a significant reduction to the mesh density, and hence the number of spatial unknowns, without a loss of the accuracy of the geometry modeling and the numerical solution.

As shown in Fig. 1, a curved triangular patch is defined by six nodes, and a position in the (ξ_1,ξ_2) parameter space is described by

$$r(\xi_1,\xi_2)=\sum_{j=1}^{6}\varphi_j(\xi_1,\xi_2)\, r_j\,, \tag{16}$$

where r_j is the Cartesian coordinate, $\varphi_j(\xi_1,\xi_2)$ is the shape function with the form

$$\varphi_j(\xi_1,\xi_2)=\begin{cases}2\xi_j(\xi_j-1/2), & j=1,2,3\\ 4\xi_{j-3}\xi_{j-5}, & j=4,5,6\end{cases}, \tag{17}$$

and

$$\xi_1+\xi_2+\xi_3=1\,. \tag{18}$$

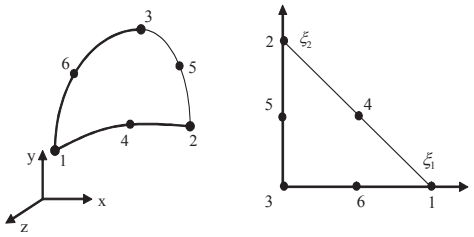

(a) **(b)**

Fig. 1. (a) A curved triangular patch with six nodes in the Cartesian coordinate system, (b) The triangular patch in the (ξ_1,ξ_2) parametric space.

The CRWG basis function is defined as

$$\begin{cases}\mathbf{f}_1(\mathbf{r})=\dfrac{\pm1}{J}[\xi_2\mathbf{I}_3-(1-\xi_1-\xi_2)\mathbf{I}_2]\\ \mathbf{f}_2(\mathbf{r})=\dfrac{\pm1}{J}\left((1-\xi_1-\xi_2)\mathbf{I}_1-\xi_1\mathbf{I}_3\right),\\ \mathbf{f}_3(\mathbf{r})=\dfrac{\pm1}{J}\left(\xi_1\mathbf{I}_2-\xi_2\mathbf{I}_1\right)\end{cases} \tag{19}$$

where

$$\mathbf{I}_1=-\frac{\partial\mathbf{r}}{\partial\xi_2},\ \mathbf{I}_2=\frac{\partial\mathbf{r}}{\partial\xi_1},\ \mathbf{I}_3=\frac{\partial\mathbf{r}}{\partial\xi_2}-\frac{\partial\mathbf{r}}{\partial\xi_1}, \tag{20}$$

and J is the Jacobi factor

$$J(\xi_1,\xi_2)=\left|\frac{\partial\mathbf{r}}{\partial\xi_1}\times\frac{\partial\mathbf{r}}{\partial\xi_2}\right|. \tag{21}$$

The surface divergence of the CRWG basis function is

$$\nabla_s\bullet\mathbf{f}_\beta(\mathbf{r})=\frac{\pm2}{\sqrt{J}}\quad(\beta=1,2,3)\,. \tag{22}$$

The differential tangent vector and normal surface element are given below, respectively,

$$d\mathbf{r}=\frac{\partial\mathbf{r}}{\partial\xi_1}d\xi_1+\frac{\partial\mathbf{r}}{\partial\xi_2}d\xi_2\,, \tag{23}$$

$$d\mathbf{S}=\frac{\partial\mathbf{r}}{\partial\xi_1}\times\frac{\partial\mathbf{r}}{\partial\xi_2}d\xi_1d\xi_2\,. \tag{24}$$

The surface normal unit vector is

$$\hat{\boldsymbol{n}}(\xi_1,\xi_2)=\frac{1}{\sqrt{g}}\frac{\partial\mathbf{r}}{\partial\xi_1}\times\frac{\partial\mathbf{r}}{\partial\xi_2}, \tag{25}$$

where

$$g=g_{11}g_{22}-g^2{}_{12}\,, \tag{26}$$

$$g_{ij}=\frac{\partial\mathbf{r}}{\partial\xi_1}\cdot\frac{\partial\mathbf{r}}{\partial\xi_2}. \tag{27}$$

III. NUMERICAL EXAMPLES

This section gives several numerical results obtained using an implementation described above to validate the proposed method. All CPU times are taken on a 3.0GHz processor.

A. Sphere

As the first example, we consider a metallic sphere centered at the origin with a radius of 0.5 meter. The problem is discretized into 219 CRWG basis functions and 50 temporal basis functions (i.e., the weighted Laguerre polynomials). The incident Gaussian pulse is with the form of

$$\mathbf{E}^i(\mathbf{r},t)=\hat{\boldsymbol{x}}\frac{4}{\sqrt{\pi}T}\boldsymbol{e}^{-\gamma^2}, \tag{28}$$

$$\gamma=\frac{4}{T}\left(t-t_0-\mathbf{r}\cdot\hat{\boldsymbol{k}}/c\right), \tag{29}$$

where $\hat{\boldsymbol{k}}$ is the unit vector in the direction of the wave propagation and is along $-\hat{z}$ direction in this example. t_0 = 12 lm represents a time delay of the pulse peak from the time origin, and T = 8 lm is the pulse width. In this work, we use lm as time unit, which is the short form of light meter. One light meter is the time taken by the electromagnetic wave to travel one meter in free space. This pulse has a frequency spectrum of 125 MHz. The scaling factor s is with the value of 1.0×10^9.

The θ component of the backward far field response ($\theta = 0°$, $\phi = 0°$) from the sphere is shown in Fig. 2 (labeled C 219). For the sake of comparison, results obtained in Reference [18] (labeled Ref) and that via 795 conventional planar RWG (PRWG) basis functions (labeled P 795) are also shown. Good agreement can be observed.

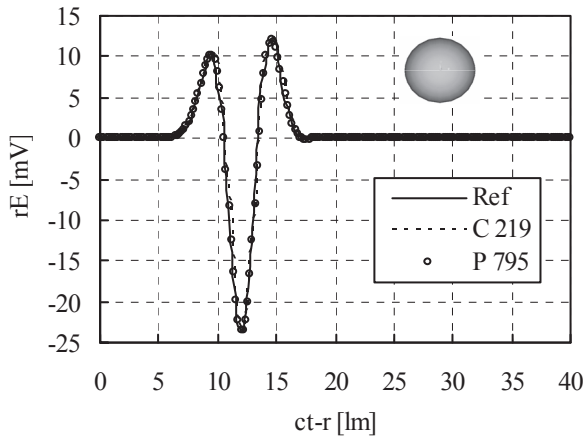

Fig. 2. θ component of transient backward far field response from a sphere.

B. Single ogive

Another example is a metallic single ogive. The analytical expression for this target is as follows:

for –1.27 m < x < 1.27 m and –π < φ < π, define

$$f(x) = \sqrt{1-(\frac{x}{5})^2 \sin^2 22.62^\circ} - \cos 22.62^\circ$$

$$y = \frac{f(x)\cos\varphi}{1-\cos 22.62^\circ} \quad . \quad (30)$$

$$z = \frac{f(x)\sin\varphi}{1-\cos 22.62^\circ}$$

The incident wave used in this example is a modulated Gaussian pulse given by

$$\mathbf{E}^i(\mathbf{r},t) = \hat{\boldsymbol{x}}\cos\left(2\pi f_0 \tau\right)\exp\left(-\frac{\left(\tau - t_p\right)^2}{2\sigma^2}\right), \quad (31)$$

where the central frequency f_0 is 160 MHz, $\tau = t - \mathbf{r}\cdot\hat{\boldsymbol{k}}/c$, $\hat{\boldsymbol{k}}$ is along $-\hat{z}$ direction, $\sigma = 6/\left(2\pi f_{bw}\right)$, $t_p = 4.5\sigma$, the bandwidth f_{bw} of the signal is 320MHz.

The problem is discretized into 444 CRWG basis functions and 100 temporal basis functions. The scaling factor s is with the value of 1.5×10^9.

After the solution procedure in time domain, the far-field signals are Fourier transformed into the frequency domain and then the bistatic radar cross section (RCS) in $\varphi = 0^\circ$ plane at several representative frequencies are calculated. These frequencies are chosen near the lowest, the middle and the highest frequency of the frequency band, and in this example they are 20 MHz, 160 MHz and 300 MHz. The results (labeled CRWG 444 DFT) are compared with those obtained via frequency domain MoM using 444 CRWGs (labeled C 444) and TD-EFIE using 648 PRWGs (labeled P 648 DFT) in Fig. 3. The results are in good agreement with each other. It's worth mentioning that 648 is the minimum number of PRWGs through exhaustive numerical experiments with increasing spatial unknowns.

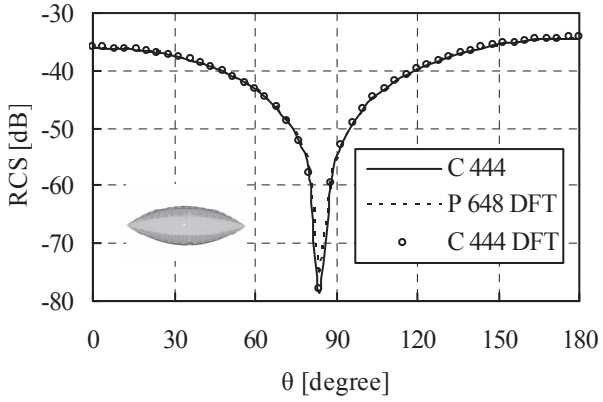

(a)

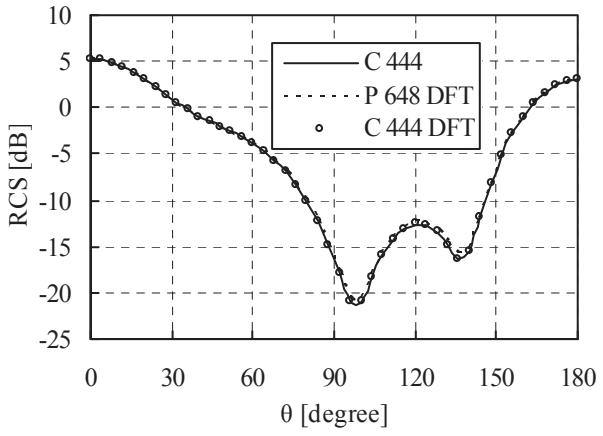

(b)

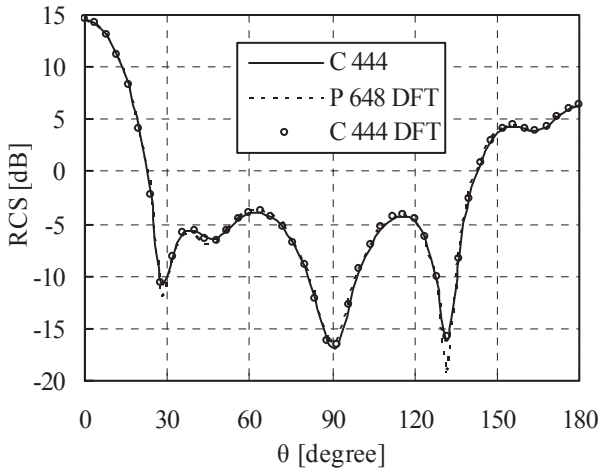

(c)

Fig. 3. Bistatic RCS of the single ogive: (a) 20 MHz, (b) 160 MHz, and (c) 300 MHz.

C. NASA almond

A metallic NASA almond is referred to as the last structure. The mathematical description used for this target is as follows:

for $-0.41667 < l < 0$ and $-\pi < \varphi < \pi$, define

$$x = dl \text{ m}$$

$$y = 0.193333d\sqrt{1-\left(\frac{l}{0.416667}\right)^2}\cos\varphi, \quad (32)$$

$$z = 0.064444d\sqrt{1-\left(\frac{l}{0.416667}\right)^2}\sin\varphi$$

for $0 < l < 0.58333$ and $-\pi < \varphi < \pi$

$$x = dl \text{ m}$$

$$y = 4.83345d\left[\sqrt{1-\left(\frac{l}{2.08335}\right)^2}-0.96\right]\cos\varphi \quad (33)$$

$$z = 1.61115d\left[\sqrt{1-\left(\frac{l}{2.08335}\right)^2}-0.96\right]\sin\varphi$$

where d=2.52374 m.

The incident wave used in this example is a modulated Gaussian pulse with the form of (31). The problem is discretized into 626 CRWG basis functions and 100 temporal basis functions. The central frequency of the incident modulated Gaussian pulse is 110 MHz and the frequency bandwidth is 220 MHz. The scaling factor s is with the value of 1.5×10^9. After a Fourier transform, the bistatic RCS in $\varphi = 0^\circ$ plane at 20 MHz, 110 MHz and 200 MHz are given.

The result (labeled C 626 DFT) is compared with those obtained via frequency domain MoM using 626 CRWGs (labeled C 626) and TD-EFIE using 985 PRWGs (labeled P 985 DFT) in Fig. 4. 985 is found to be the minimum number of PRWGs for an almost indistinguishable result, which are more than that of the CRWGs.

The efficiency of the proposed method is further compared in Table 1. Considerable reduction to both memory requirement and total CPU time are achieved.

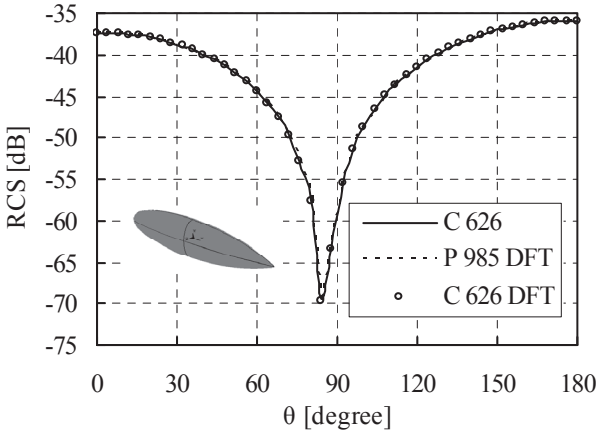

(a)

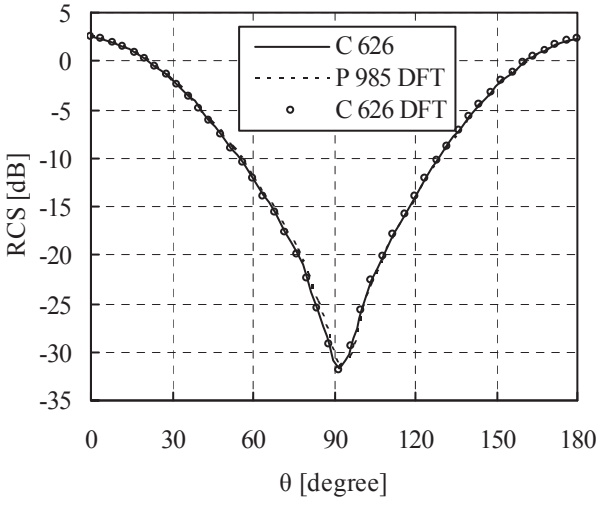

(b)

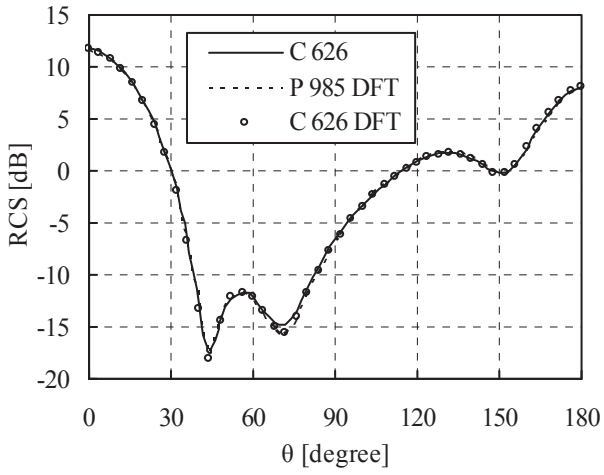

(c)

Fig. 4. Bistatic RCS of the NASA almond: (a) 20 MHz, (b) 110 MHz, and (c) 200 MHz.

Table 1: Comparison of memory requirement and total CPU time

		Geometries		
		Sphere	**Ogive**	**Almond**
Matrix Size	**PRWG**	795	648	985
	CRWG	219	444	626
RAM (MB)	**PRWG**	244	321	744
	CRWG	18	151	300
Total Time (s)	**PRWG**	275	754	1896
	CRWG	14	298	734

VI. CONCLUSION

In this paper, the marching-on-in-order time-domain integral equation method with curvilinear RWG spatial basis functions is presented to analyze transient electromagnetic scattering from arbitrarily shaped objects. Stable solutions can be ensured, and the memory requirement and CPU time are reduced without sacrificing the accuracy.

ACKNOWLEDGMENT

The authors would like to thank the editors and reviewers. The authors also appreciate the support of the Major State Basic Research Development Program of China (973 Program) under Grant No. 2009CB320201, the National Natural Science Foundation of China under Grant No. 60871013, and Jiangsu Natural Science Foundation under Grant No. BK2008048.

REFERENCES

[1] K. S. Yee, "Numerical Solution of Initial Boundary Value Problems Involving Maxwell's Equations in Isotropic Media," *IEEE Trans. Antennas Propagat.*, vol. AP-14, pp. 302-307, May 1966.

[2] D. Jiao, J. M. Jin, E. Michielssen, and D. J. Riley, "Time-Domain Finite-Element Simulation of Three-Dimensional Scattering and Radiation Problems using Perfectly Matched Layers," *IEEE Trans. Antennas Propagat.*, vol. 51, no. 2, pp. 296-305, Feb. 2003.

[3] S. M. Rao and T. K. Sarkar, "Numerical Solution of Time Domain Integral Equations for Arbitrarily Shaped Conductor/Dielectric Composite Bodies," *IEEE Trans. Antennas Propagat.*, vol. 50, no. 12, pp. 1831-1837, Dec. 2002.

[4] S. M. Rao and D. R. Wilton, "Transient Scattering by Conducting Surfaces of Arbitrary Shape," *IEEE Trans. Antennas Propagat.*, vol. 39, no. 1, pp. 56-61, Jan. 1991.

[5] F. P. Andriulli, K. Cools, F. Olyslager, and E. Michielssen, "Time Domain Calderón Identities and their Application to the Integral Equation Analysis of Scattering by PEC Objects Part II: Stability," *IEEE Trans. Antennas Propagat.*, vol. 57, no. 8, pp. 2365-2375, Aug. 2009.

[6] Y. F. Shi, M. Y. Xia, R. S. Chen, E. Michielssen, and M. Y. Lu, "Stable Electric Field TDIE Solvers Via Quasi-Exact Evaluation of MOT Matrix Elements," *IEEE Trans. Antennas Propagat.*, vol. 59, no. 2, pp. 574-585, Feb. 2011.

[7] S. M. Rao, D. R. Wilton, and A. W. Glisson, "Electromagnetic Scattering by Surfaces of Arbitrary Shape," *IEEE Trans. Antennas Propagat.*, vol. AP-30, no. 3, pp. 409-418, May 1982.

[8] G. K. Carvajal, D. J. Duque, and A. J. Zozaya, "RCS Estimation of 3D Metallic Targets using the Moment Method and Rao-Wilton-Glisson Basis Functions," *Applied Computational Electromagnetic Society (ACES) Journal*, vol. 24, no. 5, pp. 487-492, Oct. 2009.

[9] S. Wandzura, "Electric Current Basis Functions for Curved Surfaces,"

Electromagn., vol. 12, no. 1, pp. 77-91, Jan.-Mar. 1992.

[10] J. M. Song and W. C. Chew, "Moment Method Solutions using Parametric Geometry," *J. Electromagn. Waves Appl.*, vol. 9, no. 1/2, pp. 71-83, Jan.-Feb. 1995.

[11] M. J. Bluck and S. P. Walker, "Time-Domain BIE Analysis of Large Three-Dimensional Electromagnetic Scattering Problem," *IEEE Trans. Antennas Propagat.*, vol. 45, no. 5, pp. 894-901, May 1997.

[12] G. H. Zhang and M. Y. Xia, "An Enhanced TDIE Solver using Causal-Delayed Temporal Basis Functions and Curvilinear RWG Spatial Basis Functions," *Proc. Asia-Pacific Microwave Conf.*, Singapore, pp. 810-813, Dec. 2009.

[13] S. W. Huang, G. H. Zhang, M. Y. Xia, and C. H. Chan, "Numerical Analysis of Scattering by Dielectric Random Rough Surfaces using Modified SMCG Scheme and Curvilinear RWG Basis Functions," *IEEE Trans. Antennas Propagat.*, vol. 57, no. 10, pp. 3392-3397, Oct. 2009.

[14] G. H. Zhang and M. Y. Xia, "Time Domain Integral Equation Solvers using Curvilinear RWG Spatial Basis Functions and Quadratic B-Spline Temporal Basis Functions," *Proc. Asia-Pacific Microwave Conf.*, Hongkong, pp. 1-4, Dec. 2008.

[15] B. H. Jung, Y. S. Chung, M. T. Yuan, and T. K. Sarkar, "Analysis of Transient Scattering from Conductors using Laguerre Polynomials as Temporal Basis Functions," *Applied Computational Electromagnetic Society (ACES) Journal*, vol. 19, no. 2, pp. 84-92, Jul. 2004.

[16] Y. S. Chung, T. K. Sarkar, B. H. Jung, M. Salazar-Palma, Z. Ji, S.M. Jang, and K.J. Kim, "Solution of Time Domain Electric Field Integral Equation using the Laguerre Polynomials," *IEEE Trans. Antennas Propagat.*, vol. 52, no. 9, pp. 2319-2328, Sep. 2004.

[17] Y. S. Chung, Y. J. Lee, J. H. So, J. Y. Kim, C. Y. Cheon, B. J. Lee, and T. K. Sarkar, "A Stable Solution of Time Domain Electric Field Integral Equation using Weighted Laguerre Polynomials," *Microwave Opt. Technol. Lett.*, vol. 49, no. 11, pp. 2789-2793, Nov. 2007.

[18] B. H. Jung, Y. S. Chung, and T. K. Sarkar, "Time-Domain EFIE, MFIE, and CFIE Formulations using Laguerre Polynomials as Temporal Basis Functions for the Analysis of Transient Scattering from Arbitrary Shaped Conducting Structures," *Prog. Electromagn. Res.*, vol. 39, pp. 1-45, 2003.

Quan-quan Wang received the B.S. degree in Communication Engineering from Nanjing University of Science and Technology (NUST), China, in 2006.

He is currently working towards the Ph.D. degree in Electromagnetic Fields and Microwave Technology at NUST. His research interests include transient EM scattering and TDIE method.

Chao Yan received the B.S. degree in Electronic Information Engineering from Heilongjiang Institute of Science and Technology, China, in 2007, and the M.S. degree in Electromagnetic Fields and Microwave Technology from Nanjing University of Science and Technology, China, in 2010, respectively.

He is now an engineer in State-Owned Xianfeng Machinery Factory. His research interests include transient analysis and antennas.

Yi-fei Shi received the B.S. degree in Electrical Engineering from Nanjing University of Technology, China, in 2004.

He is currently working towards the Ph.D. degree in Electromagnetic Fields and Microwave Technology at Nanjing University of Science and Technology, China. His research interests include TDIE and its fast methods.

Da-zhi Ding received the B.S. and Ph.D. degrees in Electromagnetic Fields and Microwave Technology from Nanjing University of Science and Technology (NUST),

China, in 2002 and 2007, respectively. During 2005, he was with the Center of Wireless Communication in the City University of Hong Kong, Hong Kong SAR, China, as a Research Assistant.

He is currently an Associate Professor of NUST. He is the author or coauthor of over 30 technical papers. His current research interests include CEM and antennas.

Ru-shan Chen received the B.S. and M.S. degrees in Electronics from Southeast University, China, in 1987 and 1990, respectively, and the Ph.D. degree from the Department of Electronic Engineering, City University of Hong Kong (CUHK), Hong Kong SAR, China, in 2001. In 1990, he joined the Department of Electronic Engineering, Nanjing University of Science and Technology (NUST), China. Since 1996, he has been a Visiting Scholar with the Department of Electronic Engineering, CUHK. In 1999, he was promoted Full Professor of NUST, and in 2007, he was appointed Head of the Department of Communication Engineering.

His research interests mainly include CEM and millimeter wave systems. He has authored or coauthored more than 200 papers, including over 140 papers in international journals. Dr. Chen is the recipient of the Foundation for China Distinguished Young Investigators in 2003. In 2008, he became a Chang-Jiang Professor under the Cheung Kong Scholar Program of China.

Advanced Image Processing Techniques for the Discrimination of Buried Objects

Rodolfo Araneo[1] and Sami Barmada[2]

[1]Department of Electrical Engineering
Sapienza University of Rome, Rome, 00184, Italy
rodolfo.araneo@uniroma1.it

[2]Department of Energy and Systems Engineering
University of Pisa, Pisa, 56122, Italy
sami.barmada@dsea.unipi.it

Abstract ─ A numerical study for the electromagnetic detection of buried objects is presented. The whole GPR set-up is simulated through an integral formulation solved by means of the Method of Moments and a new discrimination process based on the 2D-Wavelet decomposition of computed electric field maps is proposed. The new wavelet methodology proves to be an effective tool for discrimination even in presence of noise.

Index Terms ─ 2D wavelet decomposition, GPR, MoM.

I. INTRODUCTION

Electromagnetic induction sensors (EMIS) and ground penetrating radars (GPR) are tools commonly used to find buried objects, such as antipersonnel landmines (APM) [1-3]. The basic concept they are based on is to illuminate the target with an incident field (low-frequency magnetic or high-frequency electric field) and measure the broadband spectrum of the scattered field. Different sources, antennas ,and sensors have been proposed in the past, such as horns, spirals, loaded-dipoles, or dielectric rods, loops [1-7].

The main issue is not the simple detection but the recognition of unknown buried objects, allowing to classify them as potential known targets or to discard them as clutters [1,2]. The recognition process necessarily needs the accurate design of the source system, detection sensors, and the development of post-processing algorithms [7,8]. Moreover it is worth noting that the recognition problem becomes deeply more difficult in the presence of plastic landmines, when reflections greatly surpass and hide the weak field scattered by the buried plastic targets.

In this work, the behavior of a new high frequency system for the detection of buried objects is numerically investigated by an integral approach in conjunction with a method of moments (MoM) numerical tool. The key feature of the system lies in the fact that both the magnitude and phase of all the components of the scattered electric field are used to collect information about the EM behavior of the buried object [9]. Furthermore, the potentiality of a two dimensional post processing of the collected data based on a wavelet decomposition approach is investigated. The purpose is to highlight the features of the two-dimensional signature of the buried object significantly, facilitating its discrimination.

The MoM code proves to be a suitable and efficient tool for the study of these configurations, allowing a sensitivity analysis on the influence of material and shape variations.

In order to assess the robustness of the proposed technique, a Gaussian white noise has been added to the collected data before post processing. By adding the noise we try to simulate the uncertainties and the so called “physical noise" normally encountered in practical measurements; even in this case, the signature detection is satisfactory.

II. EXPOSURE SET-UP

The set-up configuration is shown in Fig. 1. It consists of a double-ridged antenna which is used as a field source and an observation plane where the total field (incident plus scattered) is observed.

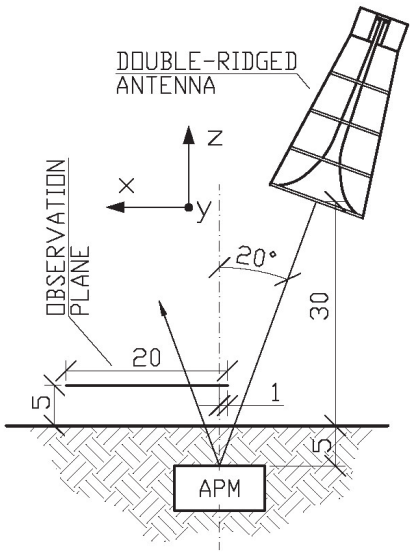

Fig. 1. Set-up configuration with a buried APM (units in cm).

The performances of the GPR are mainly affected by two key-points that must be accounted for in the optimization of the set-up.

The working frequency range must be a trade-off between penetration and resolution [2,5]. The direction and intensity of the reflection which occurs at the ground surface (ground bounce) depends on the electrical properties of the ground itself and the roughness of the surface while the penetration depth of the transmitted wave into the soil mainly depends on the ground humidity and the wavelength of the field. Lowering the working frequency of the GPR reduces the ground bounce and increases the penetration depth, but on the other side, it causes a loss of resolution in the received maps, which is necessary for an accurate detection of the buried object.

The height of the transmitting antenna must be a trade-off between transmitting antenna performance and enhancement of the received data [2,5]. A transmitting antenna closer to the ground surface shows better energy coupling with the target and reduced ground bounce, but the strong antenna-ground interaction can significantly change the antenna radiation properties, leading to a large number of false alarms. Anyway, if elevating the transmitting antenna reduces the antenna interaction with the target and the ground, on the other hand, due to the roughness of the ground surface, it makes the observation plane receive the field scattered by a larger portion of the ground, loading to a more difficult target detection. To reduce the superposition of the field scattered by the soil, the ground is usually illuminated with an oblique angle.

In light of these remarks, the set-up shown in Fig. 1 has been chosen. The double ridge antenna is the Electrometrics EM-6961 model, which shows efficient performance characteristics in the frequency range 1-6 GHz. It has been chosen since it constitutes a good tradeoff between penetration and resolution [2-8]. The antenna has been tilted 20° around the y-axis and has been oriented with his E-plane on the xz-plane, as shown in Fig. 1. The total electric field (i.e. electric field radiated by the antenna plus that scattered by the soil and the target), is computed on the observation plane showed in Fig. 1. As for the measurement procedure of this field, the photorefractive effect of thin ferroelectric films [10] can be used and is now under investigation.

III. NUMERICAL MODELING

A. Integral equations

The whole GPR configuration has been studied through a standard integral formulation. The set of equations which solve the problem can be derived through a customary application of the equivalence principle [11]. First an equivalent electric current density $\mathbf{J}_a$ is introduced over the PEC surface S_a of the antenna which is excited with a delta-gap voltage source. Next, equivalent electric $\mathbf{J}_s$ and magnetic $\mathbf{M}_s$ current densities are introduced on the surface S_s of the buried scattering object, which is considered penetrable. The boundary conditions at the surfaces S_a and S_s dictate a set of integral equations that can be written as

$$\mathbf{u}_n \times \left[\mathbf{E}^{\text{inc}} + \mathbf{E}^{\text{a}} + \mathbf{E}^{\text{s}} \right] = 0 \quad \mathbf{r} \in S_a \qquad (1a)$$

$$-\mathbf{u}_n \times \mathbf{E}^{\text{inc}} = \mathbf{u}_n \times \left[\mathbf{E}^{\text{a}} + \mathbf{E}^{\text{s}} + \mathbf{E}^{\text{s}}_{\text{d}} \right] \quad \mathbf{r} \in S_s \qquad (1b)$$

$$-\mathbf{u}_n \times \mathbf{H}^{\text{inc}} = \mathbf{u}_n \times \left[\mathbf{H}^{\text{a}} + \mathbf{H}^{\text{s}} + \mathbf{H}^{\text{s}}_{\text{d}} \right] \quad \mathbf{r} \in S_s, \qquad (1c)$$

where $\left(\mathbf{E}^{\text{inc}},\mathbf{H}^{\text{inc}}\right)$ is the incident field, $\left(\mathbf{E}^{\text{a}},\mathbf{H}^{\text{a}}\right)$ is the field scattered from the PEC antenna, $\left(\mathbf{E}^{\text{s}},\mathbf{H}^{\text{s}}\right)$ and $\left(\mathbf{E}^{\text{s}}_{\text{d}},\mathbf{H}^{\text{s}}_{\text{d}}\right)$ are, respectively, the field scattered by the currents $\left(\mathbf{J}_{\text{s}},\mathbf{M}_{\text{s}}\right)$ outside and inside the homogeneous penetrable target [11,12], $\mathbf{u}_n$ is the outward unit vector normal to the surface. Equations (1a-1c) can be cast into coupled integral equations by expressing all fields as superposition integrals (symbol $\otimes$) between the sources and the relevant dyadic Green functions (GFs):

$$\mathbf{E}^{\text{inc}}_0+\underline{\mathbf{G}}^{\text{EJ}}_{00}\otimes\mathbf{J}_{\text{a}}+ +\underline{\mathbf{G}}^{\text{EJ}}_{0\text{g}}\otimes\mathbf{J}_{\text{s}}+\underline{\mathbf{G}}^{\text{EM}}_{0\text{g}}\otimes\mathbf{M}_{\text{s}}=0\quad \mathbf{r}\in S_{\text{a}} \tag{2a}$$

$$\mathbf{E}^{\text{inc}}_{\text{g}}+\underline{\mathbf{G}}^{\text{EJ}}_{\text{g0}}\otimes\mathbf{J}_{\text{a}}+\underline{\mathbf{G}}^{\text{EJ}}_{\text{gg}}\otimes\mathbf{J}_{\text{s}}+\underline{\mathbf{G}}^{\text{EM}}_{\text{gg}}\otimes\mathbf{M}_{\text{s}}+ +\underline{\mathbf{G}}^{\text{EJ}}_{\text{d}}\otimes\mathbf{J}_{\text{s}}+\underline{\mathbf{G}}^{\text{EM}}_{\text{d}}\otimes\mathbf{M}_{\text{s}}=0\quad \mathbf{r}\in S_{\text{s}} \tag{2b}$$

$$\mathbf{H}^{\text{inc}}_{\text{g}}+\underline{\mathbf{G}}^{\text{HJ}}_{\text{g0}}\otimes\mathbf{J}_{\text{a}}+\underline{\mathbf{G}}^{\text{HJ}}_{\text{gg}}\otimes\mathbf{J}_{\text{s}}+\underline{\mathbf{G}}^{\text{HM}}_{\text{gg}}\otimes\mathbf{M}_{\text{s}}+ +\underline{\mathbf{G}}^{\text{HJ}}_{\text{d}}\otimes\mathbf{J}_{\text{s}}+\underline{\mathbf{G}}^{\text{HM}}_{\text{d}}\otimes\mathbf{M}_{\text{s}}=0\quad \mathbf{r}\in S_{\text{s}} \tag{2c}$$

where the cross product with $\mathbf{u}_n$ is suppressed for the sake of simplicity. In eqs (2), the incident fields $\left(\mathbf{E}^{\text{inc}}_{\text{g}},\mathbf{H}^{\text{inc}}_{\text{g}}\right)$ and $\mathbf{E}^{\text{inc}}_0$ are, respectively, those inside the ground and in free space due to the voltage source of the antenna, $\underline{\mathbf{G}}^{\text{PQ}}_{lm}\left(\mathbf{r},\mathbf{r}'\right)$ is the dyadic GF relating the P-type field at the observation point $\mathbf{r}$ in the medium l with the Q-type current source at source point $\mathbf{r}'$ in the medium m, and $\underline{\mathbf{G}}^{\text{PQ}}_{\text{d}}\left(\mathbf{r},\mathbf{r}'\right)$ is the PQ-type GF in the homogeneous dielectric space (inside the penetrable target). Obviously, when the target is a PEC object, $\mathbf{M}_{\text{s}}=0$ and eq. (2c) is not necessary anymore.

B. Solution of the integral equations

To efficiently solve the system of equations (2) by means of the MoM technique, it is better to recast it in a mixed potential form [11,12]. Anyway, since in a layered medium the scalar potentials of a point charges associated with horizontal and vertical current dipoles are in general different [13,14], it is necessary to modify either the scalar or the vector potential kernel. Choosing the so-called Formulation C in [13] leads to

$$\mathbf{E}(\mathbf{J})=\underline{\mathbf{G}}^{\text{EJ}}_{lm}\otimes\mathbf{J}=-j\omega\mu_0\underline{\mathbf{G}}^{\text{A}}_{lm}\otimes\mathbf{J}+ +\frac{1}{j\omega\varepsilon_0}\nabla\left(K^{\text{V}}_{lm}\otimes\nabla'\cdot\mathbf{J}\right)+C^{\text{V}}_{lm}\mathbf{u}_z\otimes\mathbf{J} \tag{3a}$$

$$\mathbf{E}(\mathbf{M})=\underline{\mathbf{G}}^{\text{EM}}_{lm}\otimes\mathbf{M} \tag{3b}$$

$$\mathbf{E}(\mathbf{J})=\underline{\mathbf{G}}^{\text{HJ}}_{lm}\otimes\mathbf{J} \tag{3c}$$

$$\mathbf{H}(\mathbf{M})=\underline{\mathbf{G}}^{\text{HM}}_{lm}\otimes\mathbf{M}=-j\omega\varepsilon_0\underline{\mathbf{G}}^{\text{F}}_{lm}\otimes\mathbf{M}+ +\frac{1}{j\omega\mu_0}\nabla\left(K^{\text{W}}_{lm}\otimes\nabla'\cdot\mathbf{M}\right)+C^{\text{W}}_{lm}\mathbf{u}_z\otimes\mathbf{M}, \tag{3d}$$

where $\underline{\mathbf{G}}^{\text{A/F}}_{lm}\left(\mathbf{r},\mathbf{r}'\right)$ are the magnetic/electric vector potential GFs , $K^{\text{V/W}}_{lm}$ are the corresponding scalar potentials and $C^{\text{V/W}}_{lm}$ are the so called correction factors [13,14]. All the expressions of the GFs can be obtained through a transmission line analogy in the transformed spectral domain as in [14].

A standard MoM procedure has been used to solve the integral equations system (2), once it has been cast in an MPIE form. In particular, the antenna and the target surfaces have been discretized through nonoverlapping triangles, and the unknown current densities have been expanded by a set of second-order subdomain basis functions, which provide a linear-normal/quadratic-tangent (LN/QT) representation of the vector quantities [15]. All encountered singular terms in the source integrals (proportional to 1/R) have been extracted and integrated analytically [16], while the remaining (source and testing) integrals have been computed by means of standard Gaussian formulas [17]. For an efficient computation of the Sommerfeld integrals necessary to transform the GFs from the spectral to the spatial domain, the weighted-averages method has been used [18].

C. Discretization of the problem

The antenna mesh is shown in Fig. 2a. The antenna is constituted of two exponentially shaped ridges, two lower and upper flares placed parallel to the H-plane (plane xz of Figs. 2) and thin copper straps placed parallel to the E-plane (plane yz of Figs. 2) [19,20]. The radiated field can be considered meanly linearly polarized with the E-field parallel to the y-axis and the H-field aligned with the x-axis.

The surface three-dimensional model of the antenna was entirely constructed with a

commercial CAD program and discretized with a professional mesh generator. The model is constituted of 3976 triangle patches, whose maximum edge length was forced to be below $\lambda/10$ at the frequency of 6 GHz. The coaxial type N input connector was not simulated as in [19], and the scheme was excited with a lumped delta-gap voltage source placed between the two ridges in the lower cavity.

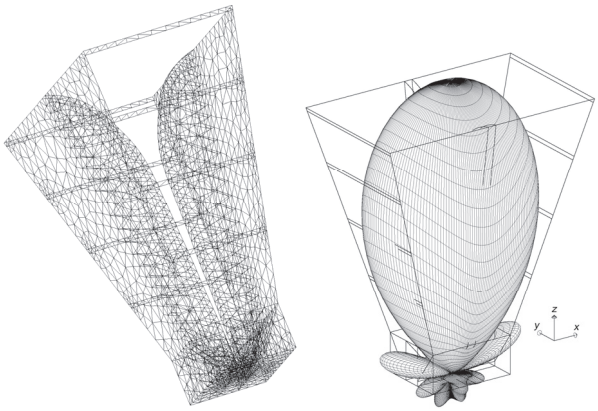

(a) (b)

Fig. 2. Simulation model of the double-ridged antenna (a) and E-field radiation pattern (b).

The computed three dimensional pattern of the radiated E-field at 2 GHz, in the near field region ($2D^2/\lambda = 52$ cm, with D maximum dimension of the radiating structure) at a distance of 50 cm, is shown in Fig. 2b, together with a magnification of the antenna (for the sake of clarity). Furthermore the electric field radiation patterns in the E- and H-planes are shown in Fig. 3. The 3dB beamwidth is around 52° and 40° in the E- and H- plane, respectively.

To test the effectiveness of the ground-penetrating system to distinguish between clutters and mines and to recognize the signature of a particular mine, the landmines and clutters shown in Fig. 4 have been considered [21]: the PMN (r=112 mm, h=56 mm) considered completely metallic, the PMA-1 (L=140 mm, H=30 mm, W=70 mm) made of plastic with dielectric constant ε_r = 4.8, a cylindrical clutter (r=10 mm, L= 100 mm) and a spherical one (R=20 mm), both considered perfectly conductive.

A realistic dielectric constant of 11.8 and loss tangent of 0.084 have been chosen for the ground in the frequency range of interest. The electric field has been computed on the observation plane on a grid of 64×64 points (2^6), in order to allow the wavelet decomposition to the fifth level. The number of MoM unknowns is 2350; the CPU time and memory requirement for solving the described problem are, respectively, five minutes and 3 Gb on a four-core 3 GHz 64-bit desktop workstation.

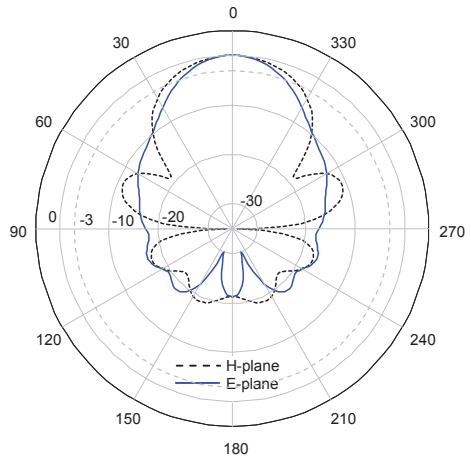

Fig. 3. E- and H- plane amplitude patterns of the double ridged antenna.

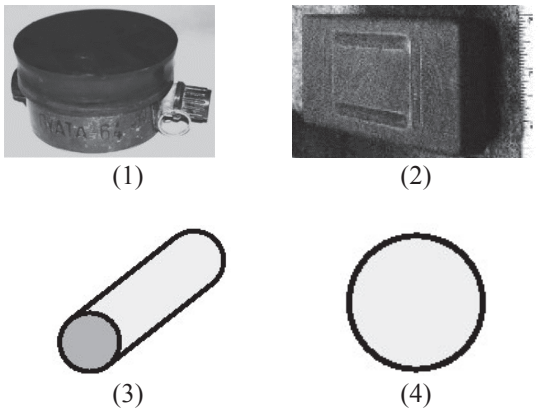

(1) (2)

(3) (4)

Fig. 4. Considered landmines – PMN (1) and PMA-1 (2) – and clutters – cylindrical (3) and spherical (4).

IV. IMAGE PROCESSING

As mentioned in the previous sections, both the magnitude and phase of all the components of the scattered electric field are used to collect information about the EM behavior of the buried object. This big amount of data can be easily represented by the use of two dimensional maps. The capability of the wavelet expansion tool in

signal processing is well established [22], and has been used also in electrical engineering in order to evidence special behavior of the analyzed quantities, which cannot be evidenced by a simple analysis of the signal in its unprocessed form [23, 24]. Furthermore, some attempts of wavelet based post processing in the area of discrimination of buried objects have been previously presented [25].

It is well-known that a multiresolution analysis is characterized by wavelet bases composed by the scaling functions $\phi(x)$ and wavelet functions $\psi(x)$, the former being a low pass filter and the latter a high pass filter. A single dimension wavelet expansion yields a set of coefficients related to the correlation between a general function $f(x)$ and the scaling and wavelet functions. In particular filtering performed by $\phi(x)$ leads to what is called a "blurred version" of the original signal, while filtering with $\psi(x)$ gives a signal containing the higher frequencies, called "detail". Iteratively performing this sub band filtering (on the blurred version) leads to the multi – resolution decomposition of a signal in sum between a smooth signal (qualitatively an averaged signal) and a set of details.

In this case, we deal with 2D signals (the value of electric field on a plane) which can be easily organized in 2D color maps, i.e. figures to be analyzed by a proper technique.

The construction of two dimensional bases, necessary for image processing, is performed by using the so called separable wavelet bases, i.e. using the following basis functions

$$\begin{aligned} \phi^1(x,y) &= \phi(x)\phi(y) \\ \psi^1(x,y) &= \phi(x)\psi(y) \\ \psi^2(x,y) &= \psi(x)\phi(y) \\ \psi^3(x,y) &= \psi(x)\psi(y) \end{aligned}, \tag{4}$$

in which functions at the same level of decomposition are used. Thinking about the frequency characteristics of the functions $\phi(x)$ and $\psi(x)$, it is evident that $\hat{\phi}^1(\omega_x,\omega_y)$ is a low pass filter in two dimensions, hence performing the role of extracting the average of the map; on the other hand $\left|\hat{\psi}^1(\omega_x,\omega_y)\right|$ is a low pass filter for the *x*-direction and a high pass filter for the *y*-direction, responding to variations in the vertical direction. In a similar way $\left|\hat{\psi}^2(\omega_x,\omega_y)\right|$ responds to variations on the horizontal direction, while $\left|\psi^3(\omega_x,\omega_y)\right|$ is a high pass filter both for horizontal and vertical frequencies, hence responding to variations along diagonals.

Each image is consequently decomposed following the same scheme of the multiresolution analysis into a set of blurred versions plus a set of details. The only difference is that at each level of decomposition a set of 3 matrices of details are obtained, called vertical, horizontal, and diagonal. Considering that this analysis can be performed on each field component, this results in a considerable amount of data to be analyzed.

Two main issues arise at this point: the first one comes from the previous consideration, since it is not always easy to deal with big amount of data. An efficient way to treat them is needed, and it should be characterized by a highly synthetic approach. This issue is addressed in the next section.

Furthermore, there is the need of a proper choice of the wavelet family to be used: after several different tests, the authors' choice is to use biorthogonal wavelets, since they are symmetric and are the best choice for image processing.

V. NUMERICAL RESULTS

A. Data post processing

A careful analysis of the whole set of data – i.e. E field in each direction decomposed at different levels – has been performed, with the aim of determining their most significant subset and define a simple technique which is able to solve our problem.

A simple 1-level wavelet decomposition is enough to evidence the signatures of the bombs and the clutters.

Furthermore, through numerous tests, it has been observed that the most significant information is given by the z component of the electric field. Figure 5 shows the color maps relative to the magnitude of the z component of the total electric field on the observation plane of two targets, PMA

and PMN, and of the two clutters, cylindrical (#1) and spherical (#2).

The wavelet expansion of the total field on the observation plane when the soil is absent is necessary to construct a first level signature of the considered target. The signature is a crucial parameter in the discrimination of the unknown object as a target or as a simple clutter.

Figure 6 reports the diagonal coefficients of the 1-level wavelet expansion performed on the previous map of the Ez-component of a PMN mine, respectively in vacuum and buried.

Figure 7 reports the diagonal coefficient of the 1-level wavelet expansion of the Ez-component of a PMA mine. Finally, Fig. 8 reports the diagonal coefficients of the 1-level wavelet expansion of the Ez-maps of the two considered buried clutters.

In all the previous figures, brighter colors are related to higher magnitudes on a scale of 255 tones.

At first sight, it is obvious how the use of the wavelet expansion allows determining the characteristic behavior of the different objects, which is not visible by simply analyzing the electric field maps.

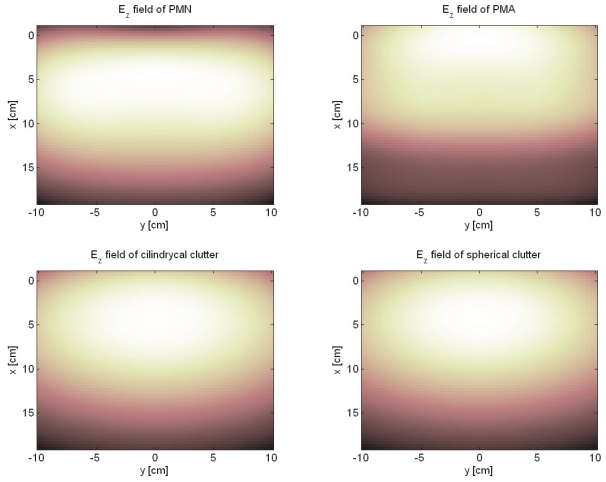

Fig. 5. z-component of the total electric field on the observation plane for the two targets and the two clutters.

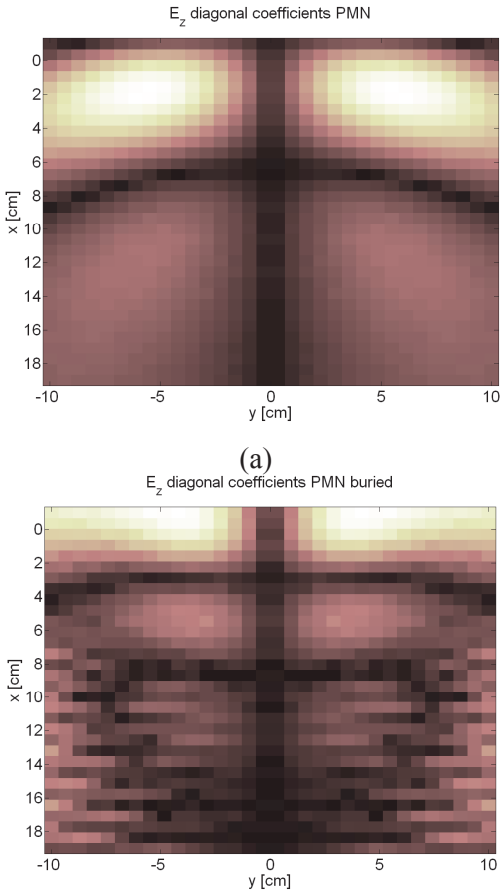

(a)

(b)

Fig. 6. Diagonal coefficients of the wavelet expansion of the Ez electric field related to the PMN bomb a) in vacuum , b) buried.

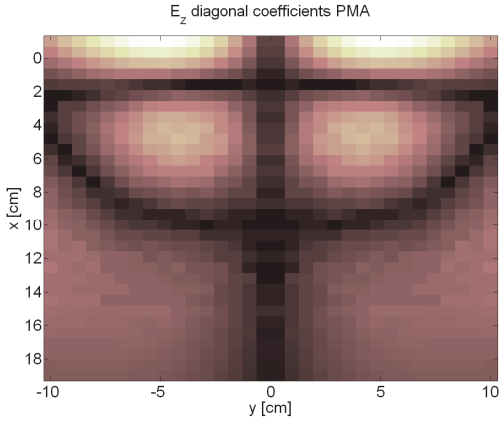

(a)

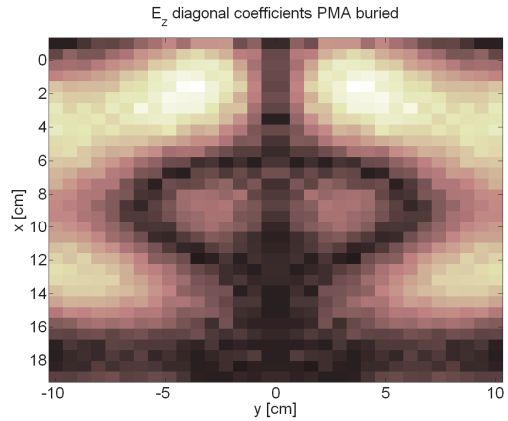

(b)

Fig. 7. Diagonal coefficients of the wavelet expansion of the Ez electric field related to the PMA bomb a) in vacuum, b) buried.

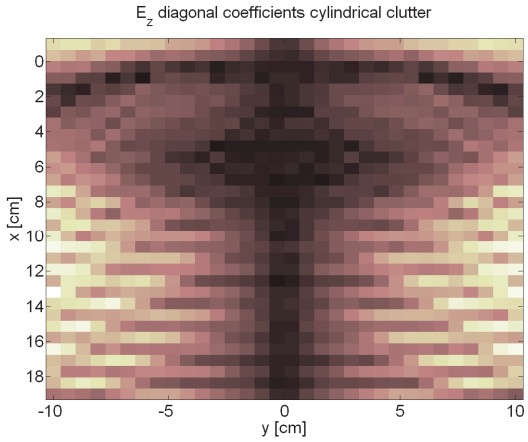

(a)

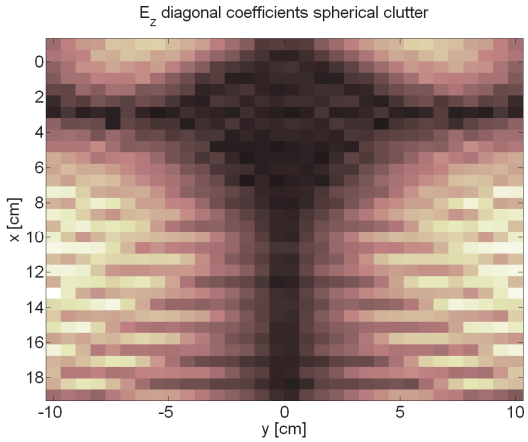

(b)

Fig. 8. Diagonal coefficients of the wavelet expansion of the Ez electric field related to a) the buried cylindrical, b) spherical clutters.

It is also easy to note how the signatures of the two clutters are very similar to each other and very different from the signatures of the bombs in empty spaces. On the other hand, the signatures of the buried bombs can be easily recognized in the figures, comparing them with the signature of the bombs in empty space.

The conclusion drawn by simply looking at the color maps of the details can also be obtained by calculating the correlation between the single maps. The correlation between two matrices yields a coefficient which gives information about how the two matrices are correlated: a higher coefficient means highly correlated matrices, while a lower coefficient substantially means two different matrices.

We start from the knowledge of the diagonal details for 4 levels of decomposition of the two bombs in free space. For each single level the correlation between the diagonal details of the unknown object and the two bombs in free space is calculated and the coefficients of all the levels of decomposition are added up to obtain a single coefficient. The results are shown in Table 1. It is worth noting that the 5-level decomposition is possible on a grid of 64 points but it is useless since it does not add any information content.

Table 1: Correlation coefficients of the unknown target (clutter or bomb) with the two bombs

	PMA	PMN
PMA buried	2.2	-3
PMN buried	-0.4	1.5
Clutter1	2.1	-2.2
Clutter2	2.2	-1.9

The grey cells show a high correlation, which means that the two bombs can be recognized, but at the same time the clutters would lead to a false alarm since they would be related to a PMA bomb. In this case, a visual analysis of the color maps is necessary to definitely discern the clutters from the real bomb.

B. Robustness analysis

In order to take into account the typical errors present in practical measurements, a Gaussian white noise has been added to all the simulations relative to buried objects (PMA, PMN, Clutter 1 and Clutter 2), while the vacuum simulations of

the PMA and PMN have been kept as in the previous subsection.

The procedure previously explained for the calculation of the correlation has been performed again for a statistically significant set of cases. The results are reported in Table 2, which shows the probability of positive correlation.

The results are in accordance with Table 1; the same grey cells show the highest probability of positive correlations, meaning that the two bombs can be recognized, but at the same time the clutters would lead to a false alarm since they would be related to a PMA bomb. At the same time, there is a 29% percent of probability that a PMN bomb would be recognized as PMA, which is of course not an exact detection but it doesn't lead to any risky situation.

Table 2: Correlation coefficients of the unknown target (clutter or bomb) with the two bombs when noise is added

	PMA	PMN
PMA buried	0.97	0.00
PMN buried	0.29	0.90
Clutter1	0.97	0.02
Clutter2	0.97	0.05

VI. CONCLUSION

The paper presents the numerical study of a GPR set-up for the electromagnetic detection of buried objects. The MoM method is used for the full-wave simulation of the whole set-up with targets and clutters. A post-processing based on the Wavelet decomposition of 2D electric field maps is proposed. The Wavelet decomposition makes easy the discrimination between targets and clutters but further investigations and improvements are necessary to reduce the false alarms.

REFERENCES

[1] I. J. Won, D. A. Keiswetter, and T. H. Bell, "Electromagnetic Induction Spectroscopy for Clearing Landmines," *IEEE Trans. Geosci. Remote Sensing*, vol. 39, no. 4, pp. 703-709, April 2001.

[2] D. J. Daniels, Ground Penetrating Radar 2nd Edition. *IEE Radar, Sonar, Navigation and Avionics Series 15*, Institution of Electrical Engineers, London 2004.

[3] K. P. Prokopidis, T. D. Tsiboukis, "Modeling of Ground-Penetrating Radar for Detecting Buried Objects in Dispersive Soils," *Applied Computational Electromagnetic Society (ACES) Journal*, vol. 22, no. 2, pp. 287–294, July 2007.

[4] C. H. Huang, C. C. Chiu, C. J. Lin, and Y. F. Chen, "Inverse Scattering of Inhomogeneous Dielectric Cylinders Buried in a Slab Medium by TE Wave Illumination," *Applied Computational Electromagnetic Society (ACES) Journal*, vol. 22, no. 2, pp. 295–301, July 2007.

[5] C. C. Chen, S. Nag, W. D. Burnside, J. I. Halman, K. A .Shubert, and L. Peters, "A Standoff Focused-Beam Land Mine Radar", *IEEE Trans. Geosci. Remote Sensing*, vol. 38, no. 1, pp. 507-514, Jan. 2000.

[6] C. C. Chen, K. R. Rao, R. Lee, "A New Ultrawide-Bandwidth Dielectric-Rod Antenna for Ground-Penetrating Radar Applications," *IEEE Trans. Antennas Propagat*., vol. 51, no. 3, pp. 371-377, March 2003.

[7] P. Van Genderen, L. Nicolaescu, and J. Zijderveld, "Some Experience with the Use of Spiral Antennas for a GPR for Landmine Detection," *Proc. Int. 2003 Radar Conference*, pp. 219-223.

[8] C. Huang, C. Chen, C. Chiu, and C. Li, "Reconstruction of the Buried Homogenous Dielectric Cylinder by FDTD and Asynchronous Particle Swarm Optimization," *Applied Computational Electromagnetic Society (ACES) Journal*, vol. 25, no. 8, pp. 672–681, August 2010.

[9] R. Araneo and S. Celozzi, "Numerical Analysis of Subsurface Objects Discrimination Systems," *IEEE Transactions on Magnetics*, vol. 39, no. 3, pp. 1219-1222, May 2003.

[10] S. C. Abrahams and K. Nassau, *Encyclopedia of Materials Science and Engineering*, Pergamon Press, 1986.

[11] A. F. Peterson, S. L. Roy, and R. Mittra, *Computational Methods for Electromagnetics*, IEEE Press, Piscataway, NJ, 1997.

[12] E. Miller, L. Medgyesi-Mitschang, and E. H. Newman, *Computational Electromagnetics,*

Frequency-Domain Method of Moments, Piscataway, NJ, IEEE Press, 1992.

[13] K. A. Michalski and D. Zheng, "Electromagnetic Scattering and Radiation by Surfaces of Arbitrary Shape in Layered Media, Part I: Theory," *IEEE Trans. Antennas Propagat.*, vol. 38, no. 3, pp. 335-344, March 1990.

[14] K. A. Michalski, J. R. Mosig, "Mulilayered media Green's Functions in Integral Equation Formulations", *IEEE Trans. Antennas Propagat.,* vol. 45, no. 3, pp. 508-519, March 1997.

[15] K. R. Aberegg, A. Taguchi, and A. F. Peterson, "Application of Higherorder Vector Basis Functions to Surface Integral Equation Formulations," *Radio Sci.*, vol. 31, no. 5, pp. 1207–1213, Sep. 1996.

[16] R. D. Graglia, "On the Numerical Integration of the Linear Shape Functions Times the 3-D Green's Function or its Gradient on a Plane Triangle," *IEEE Trans. Antennas Propagat.*, vol. 41, no. 10, pp. 1448–1455, Oct. 1993.

[17] D. A. Dunavant, "High Degree Efficient Symmetrical Gaussian Quadrature Rules for the Triangle," *Intern. J. Num. Meth. Engin.*, vol. 21, pp. 1129– 1148, Jun. 1985.

[18] K. A. Michalski, "Extrapolation Methods for Sommerfeld Integral Tails," *IEEE Trans. Antennas Propagat.*, vol. 46, no. 10, pp. 1405–1418, Oct. 1998.

[19] C. Bruns, P. Leuchtmann, and R. Vahldieck, "Analysis and Simulation of a 1–18 GHz Broadband Double-Ridged Horn Antenna", *IEEE Trans. Electromagn. Compatibil.*, vol. 45, no. 1, pp. 55-60, Feb. 2003.

[20] Z. Zhang and R. E. Diaz, "Simulation of Broadband Double-Ridged Horn in High-Fidelity Material Characterization using Finite-Difference Time-Domain Method," *2005 IEEE Antennas and Propagation Society Int. Symp.*, vol. 1B, pp. 561-564.

[21] MIMEVA: Study of generic Mine-like Objects for R&D in Systems for Humanitarian Demining, http://humanitarian-security.jrc.it/.

[22] S. G: Mallat, *A Wavelet Tour of Signal Processing*, Academic Press.

[23] W. Chen, X. Yang, and Z. Wang, "Application of Wavelets and Auto-Correlation-Function For Cancellation of High-Frequency EMI Noise," *Applied Computational Electromagnetic Society (ACES) Journal*, vol. 24, no. 3, pp. 332–336, June 2009.

[24] S. Barmada, A. Landi, M. Papi, and L. Sani, "Wavelet Multi-Resolution Analysis for Monitoring the Occurrence of Arcing on Overhead Electrified Railways," *Proc. Instn Mech. Engrs*, vol. 217, part. F: J. Rail and Rapid Transit, pp. 177-187.

[25] S. Perrin, A. Bibaut, E. Duflos, and P. Vanheeghe, "Use of Wavelets for Ground-Penetrating Radar Signal Analysis and Multisensor Fusion in the Frame of Land Mine Detection," 2000 *IEEE International Conference on Systems, Man, and Cybernetics*, vol. 4, pp. 2940-2945.

Rodolfo Araneo was born in Rome, Italy, on October 29, 1975. He received the M.S. (cum laude) and Ph.D. degrees in Electrical Engineering from the University of Rome "La Sapienza", Rome, in 1999 and 2002, respectively.

During the master thesis in 1999, he was a Visiting Student at the National Institute of Standards and Technology (NIST) Boulder, CO where he worked on TEM cells and shielding. During the second semester of the year 2000, he was a Visiting Researcher of the Department of Electrical and Computer Engineering of University of Missouri–Rolla (UMR) where he worked on printed circuit boards and finite difference time-domain techniques.

Dr. Araneo received the Past President's Memorial Awards in 1999 from IEEE EMC Society. His research activity is mainly in the field of electromagnetic compatibility (EMC) and includes numerical and analytical techniques for modeling high-speed printed circuit boards, shielding, and transmission line analysis.

Sami Barmada was born in Livorno, Italy, in 1970. He received the Master (cum laude) and Ph.D. degrees in Electrical Engineering from the University of Pisa, Italy, in 1995 and 2001, respectively.

From 1995 to 1997, he was with ABB Teknologi, Oslo, Norway, where he was involved with distribution network analysis and optimization. He is currently an Associate Professor with the Department of Energy and Systems Engineering, University of Pisa, where he is involved with numerical computation of electromagnetic fields, modeling of multiconductor transmission lines, powerline communications.

He is author of about 100 papers published on international journals and peer reviewed conference proceedings.

Prof. Barmada was the technical chairman of the Progress in Electromagnetic Research Symposium (PIERS), Pisa, Italy, 2004 and the general chairman of the ACES 2007 conference in Verona, Italy.

He was the recipient of the 2003 J F Alcock Memorial Prize, presented by The Institution of Mechanical Engineering, Railway Division, for the best paper in technical innovation and he currently is IEEE Senior Member and ACES member.

Design of a Half-Mode SIW High-Pass Filter

Wei Shao and Jia-Lin Li

Institute of Applied Physics
University of Electronic Science and Technology of China, Chengdu, 610054, P. R. China
weishao@uestc.edu.cn, jialinuestc@yahoo.com.cn

Abstract ─ A planar high-pass filter with simple topology, low insertion loss and high power handling is presented in this paper. It is based on the half-mode substrate-integrated waveguide (SIW) structure whose shorting wall is implemented with periodical via-holes. Meanwhile, bevel edges are embedded to achieve good impedance matching. Parameter studies are also performed to give design insights for practical applications. A planar waveguide filter with cutoff frequency of 10 GHz is designed and built. The measured data have a good agreement with the simulated responses, and demonstrate practical utility of the proposed topology.

Index Terms ─ Half-mode, high-pass filter, impedance matching, waveguide.

I. INTRODUCTION

Microwave filters, including low-pass, band-pass, band-stop and high-pass types, play a key role in modern wireless systems. Recent studies introduce some waveguide-based or other bandpass filter structures [1-6]. The design of high performance high-pass filters (HPFs) seems to be more challenging because the series connected capacitors from lumped prototype filters introduce extra loss by using distributed components. Waveguide-based structures characterize inherently high-pass responses [7], but its three dimensional (3-D) configuration is not easy to be integrated with planar circuits.

An HPF with planar structures based on an exponentially tapered nonuniform transmission line [8], but its size may be bulky. Using high performance inductors in advanced high resistivity SOI CMOS technology, [9] develops an ultra wideband HPF integrated into the silicon-based substrate. Based on complementary split ring resonators, HPFs can also obtain compact sizes, but the double-sided configuration leads to a relatively complicated circuit topology and assembly problems [10-11]. A filter in [12] based on modified double-sided parallel strip lines shows good electric performance, but it has a multilayer-based structure.

Using the conventional microstrip line with short-circuited edge for planar filter applications is an effective way to design HPFs since it is compatible with most of planar circuits with good performance [13-14]. By using an electric wall placed at the edge of wide microstrip line, the structure is analyzed and confirmed from measurements [13]. Further, it is incorporated with other circuits to demonstrate a practical application of a 20-40 GHz subharmonically pumped mixer [14]. A transmission line loaded at regular intervals with closely-spaced shorted stubs [15]. Such a periodic structure exhibits waveguide-like behavior with a first pass-band whose width is a function of the characteristic impedance and pitch of the stubs. It also shows that the structure degenerates into a planar waveguide whose cutoff frequency corresponds to a short-circuited stub length when the stub pitch vanishes. To achieve good impedance matching, on the other hand, the extra matching networks lead to a large circuit size.

In this paper, a planar HPF with simple topology, low insertion loss and high power handling is studied. It is a waveguide-based structure, specifically, a half-mode substrate-integrated waveguide (SIW) structure [16]. To obtain good impedance matching, a pair of bevel edges is adopted. Measurement results with cutoff

frequency of 10 GHz agree well with simulated characteristics, and demonstrate practical utility of the developed planar HPF topology.

II. DESIGN OF THE SIW FILTER

Figure 1 shows the 3-D view of the proposed filter structure. Basically, it can be treated as a section of the main transmission line with width w_f loaded unsymmetrically with a stepped microstrip line. The length of the stepped transmission line is L, and far away from the main line, a series of metalized via-holes with radius r and periodicity p are parallelly etched on the stepped edge. The distance from the hole center to another edge of the line is denoted as w. Meanwhile, a pair of tilting edges with an angle α and a length a are etched on the corners. The structure is etched on the upper side of a Rogers RT/Duroid 5870 substrate that has a relative permittivity of 2.33 with a thickness of 31 mils.

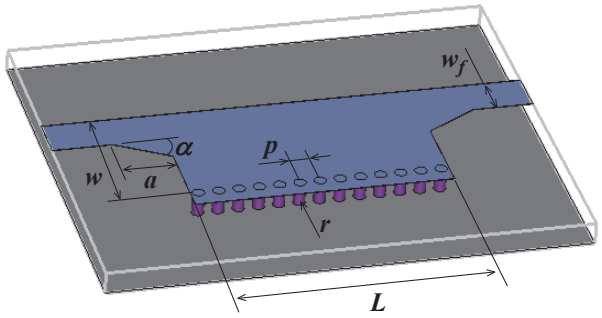

Fig. 1. 3-D view of the proposed filter.

Such a structure supports the microstrip higher-order field modes. The first HE_1 mode is similar to TE_{10} mode in a rectangular waveguide. Figure 2 illustrates the transition from a half-mode SIW mode to an equivalent TE_{10} mode. Fringe electric fields from the line to the ground plane are equivalent to a supplementary capacitor, which can be replaced with a slightly widened strip. Thus, the effective line width w_{eff} is observed with the needed line extension Δl for compensating the open-end effect. At the same time, the initial relative permittivity of the substrate is represented by an effective one ε_{eff} in this case. Finally, the equivalent result corresponding to TE_{10} mode of a rectangular waveguide is obtained by introducing a magnetic wall. Figure 3 shows that the electric field distribution in the proposed structure is similar to those in a rectangular waveguide.

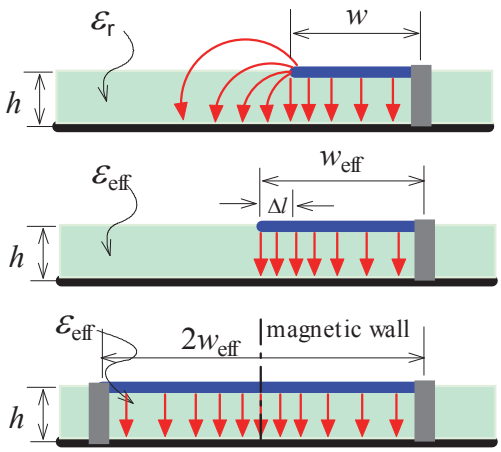

Fig. 2. Transition from the structure to an equivalent rectangular waveguide.

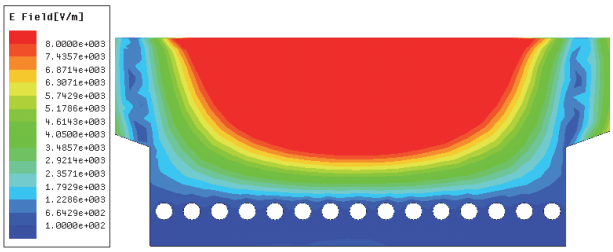

Fig. 3. Simulation results (by HFSS Software [17]) of electric field distribution in the structure.

Therefore, the half-mode SIW exhibits a cutoff frequency and high-pass filtering characteristic. It also exhibits low insertion loss and high power handling capacity like waveguides. Its cutoff frequency f_c can be evaluated from the equivalent rectangular waveguide model

$$f_c = \frac{c_0}{4w_{eff}\sqrt{\varepsilon_{eff}}}, \tag{1}$$

where c_0 is the light velocity in free space. The microstrip effective width w_{eff} is given by [18]

$$w_{eff} = w - \frac{r^2}{0.24p}. \tag{2}$$

The radius r and periodicity p of via-holes can be determined as follows [19]

$$\frac{p}{\lambda_g} \le 0.25, \tag{3}$$

and

$$\frac{r}{p} \le 0.5, \tag{4}$$

where λ_g is the guided wavelength at the cutoff frequency.

To simplify the design of an HPF with f_c=10GHz, ε_{eff} in (1) is approximated to ε_r. Therefore, w_{eff} should be 4.91 mm from (1). Via-holes with r=0.25mm and p=0.8mm, which satisfy design rules of (3) and (4), are adopted. Meanwhile, w is calculated from (2) to be 5.17 mm. After performing optimal electromagnetic design with junction discontinuities, the filter is designed with its physical parameters as: L=12mm, w=5mm, a=2.6 mm, α=30°, and w_f =2.2mm for a 50Ω microstrip line. Figure 4 shows the achieved performance of this filter.

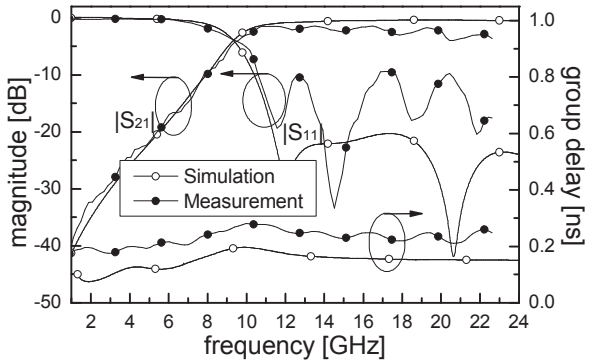

Fig. 4. Frequency responses of the filter.

To validate our design, a demonstrator filter shown in Fig. 5 is built. Measurements are performed by using a vector network analyzer [20]. The measured frequency responses are also recorded in Fig. 4, where the measured insertion loss involves the circuit loss and effects of SMA connectors (i.e., non-ideal coaxial/ microstrip-line transitions). Measurements indicate that the insertion loss is gradually increased with the increase of the operation frequency. This can be attributed to the following possible reasons: the substrate utilized in this demonstration generally works below 18GHz. Thus, its dielectric loss beyond this frequency may be relatively high. Another reason is due to the Ku-band SMA connectors employed in the measurement. A higher loss associated with the connectors is suffered from at the higher operation frequency band. It is found that the measured maximum insertion loss within the passband is approximately 3dB. Within the pass-band, the minimum return loss is better than 10dB. Figure 4 also plots the measured pass-band group delay variation of the fabricated circuit, and its value is less than 0.5ns. From these results, it is seen that the measured data reasonably match the predictions.

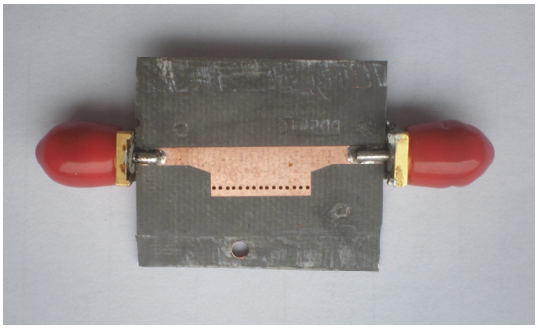

Fig. 5. Photograph of the fabricated circuit.

III. PARAMETER STUDIES

Purposes of parameter studies in this section are to provide some design insights for practical applications. It can be seen from above presentations that the metalized via-holes (r and p) are empirically predetermined based on (3) and (4). Although the parameter w needs fine tuning from optimal EM simulations, it is basically determined from (1) and (2). Hence, the first key parameter that needs studying is the length L of the short-circuited planar waveguide. By sweeping L (other parameters a, α, w, r, p, and w_f keep constant as mentioned before), it is interesting to find that L primarily affects the roll-off of the filter, as illustrated in Fig. 6(a). A shorter L corresponds to a more compact design at the cost of slightly poor roll-off or filter selectivity. Hence, L=12mm is utilized in this design for compactness considerations.

Results from sweeping simulations with the angle α indicate that α is not sensitive to filter selectivity or stop-band roll-off, but α primarily affects the pass-band return loss. A smaller angle cannot improve the lower pass-band return loss, while a larger α deteriorates the whole pass-band return loss, as shown in Fig. 6(b). Therefore, α=20° is adopted to obtain good return-loss performance.

Figure 6(c) shows that the bevel length a also influences the pass-band return loss. The lower pass-band return loss can achieve good performance under a small value of a. On the other hand, a larger bevel length a can worsen the whole pass-band performance when referring to a 20dB return loss. Consequently, a=2.6mm is selected from optimal simulations in our design.

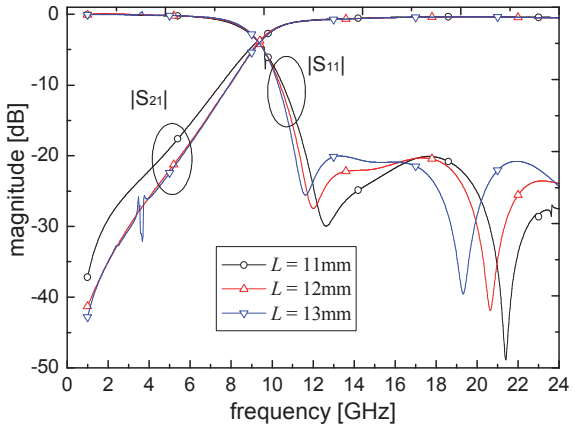

(a) Sweeping parameter *L*.

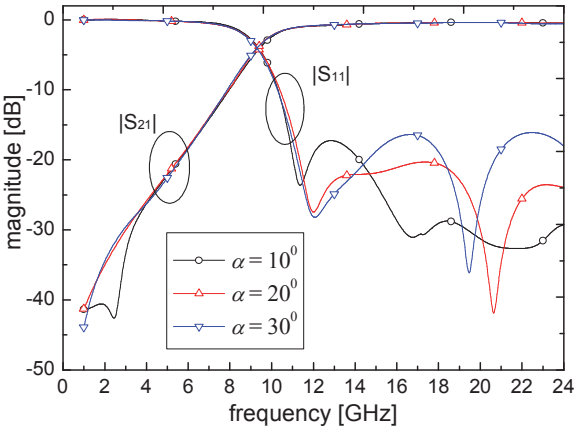

(b) Sweeping angle α.

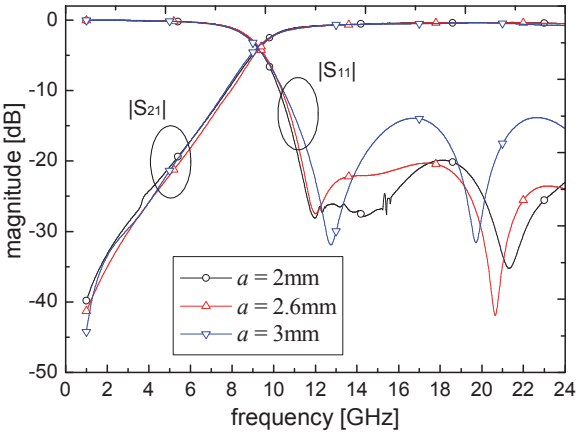

(c) Sweeping parameter *a*.

Fig. 6. Sweeping responses of the studied filter.

VI. CONCLUSION

By replacing electric walls in a rectangular waveguide with metalized via-holes, a planar waveguide-based HPF has been developed in this paper. Further, based on the symmetry of mode-field distribution, a half-mode structure is employed to get a compact circuit topology. A pair of bevel edges is embedded into the planar waveguide to obtain good impedance matching. Parameter studies have been performed to give more insights to design such a kind of filters. An example filter with cutoff frequency of 10 GHz has been designed, built, and experimentally examined, and results validate the predications well.

ACKNOWLEDGMENT

This work is partly supported by the National Natural Science Foundation of China (60901023), the DPR Foundation (9140A03011210DZ02) and the Fundamental Research Funds for the Central Universities (ZYGX2010J043).

REFERENCES

[1] C. Zhong, J. Xu, Z.-Y. Yu, M.-Y. Wang, and J.-H. Li, "Half Mode Substrate Integrated Waveguide Broadband Bandpass Filter," *Progress In Electromagn. Research Lett.*, vol. 4, pp. 131-138, 2008.

[2] Z. Sotoodeh, B. Biglarbegian, F. Hojat Kashani, and H. Ameri, "A Novel Bandpass Waveguide Filter Structure on SIW Technology," *Progress In Electromagn. Research Lett.*, vol. 2, pp. 141-148, 2008.

[3] Q. Lai, C. Fumeaux, W. Hong, and R. Vahldieck, "Characterization of the Propagation Properties of the Half-Mode Substrate Integrated Waveguide," *IEEE Trans. Microwave Theory Tech.*, vol. MTT-57, pp. 1996-2004, 2009.

[4] C. Zhong, J. Xu, Z.-Y. Yu, M.-Y. Wang, and J. Li, "Half Mode Substrate Integrated Waveguide Broadband Bandpass Filter using Photonic Band Gap Structures," *International Conf. on Microw. and Millimeter Wave Technol., ICMMT*, pp. 22-24, 2008.

[5] E. Mehrshahi and M. Salehi, "A Simple Technique for Propagation Characteristics of Substrate Integrated Waveguide," *Applied Computational Electromagn. Society Journal*, vol. 25, no. 8, pp. 690-695, 2010.

[6] A. Boutejdar, G. Nadim, and A. S. Omar, "Compact Bandpass Filter Structure using an Open Stub Quarter-Wavelength Microstrip Line Corrections," *Proc. 35th EuMC (Paris)*, 2005.

[7] U. Rosenberg, S. Amari, J. Bornemann, and R. Vahldieck, "Compact Pseudo-Highpass Filters Formed by Cavity and Iris Resonators," *34th European Microw. Conf.*, pp. 985–988, 2004.

[8] A. Toscano, L. Vegni, and F. Urbani, "Exponentially Tapered Nonuniform Transmission Lines for High-Pass Filter Design," *Microwave Opt. Technol. Lett.*, vol. 16, no 4, pp. 227-229, 1997.

[9] F. Gianesello, D. Gloria, C. Raynaud, C. Tinella, P. Vincent, F. Saguin, S. Boret, C. Clement, B.-V. Haaren, J.-M. Fournier, G. Dambrine, and P. Benech, "Integration of Ultra Wide Band High Pass Filter using High Performance Inductors in Advanced High Resistivity SOI CMOS Technology," *Silicon RF Conf.*, pp. 248-251, 2006.

[10] C. Li, K.-Y. Liu, and F. Li, "Design of Microstrip Highpass Filters with Complementary Split Ring Resonators," *Electron. Lett.*, vol. 43, no. 1, pp. 35-36, 2007.

[11] P. Mondal, and A. Chakrabarty, "Compact Highpass Filter using Complementary Split Ring Resonator," *Microwave Opt. Technol. Lett.*, vol. 49, no. 10, pp. 2469-2471, 2007.

[12] S. Misan, R. Haviv, D. Ackerman, H. Matzner, and M. Haridim, "A High-Pass Filter Based on Modified Double-Sided Parallel-Strip Lines," *Microwave Opt. Technol. Lett.*, vol. 51, no. 11, pp. 2691-2694, 2009.

[13] J. Chramiec, R. Kieda, and M. kitlinski, "Full-Wave Simulation of Microstrip Line with Short-Circuited Edge," *15th int. Conf. Microwave, Radar and Wireless Communications*, pp. 222-224, 2004.

[14] J. Chramiec, M. Kitlinski, and B.-J. Janiczak, "Microstrip Line with Short-Circuited Edge as a High-Pass Filter Operating up to Millimeter-Wave Frequencies," *Microwave Opt. Technol. Lett.*, vol. 49, no. 9, pp. 2177-2179, 2007.

[15] K.-M. Noujeim, "High-Pass Filtering Characteristics of Transmission-Line Combs," *IEEE Trans. Microwave Theory Tech.*, vol. MTT-57, pp. 2743-2752, 2009.

[16] W. Hong, B. Liu, Y. Wang, Y. Wang, Q. Lai, H. Tang, X. X. Yin, Y. D. Dong, Y. Zhang, and K. Wu, "Half Mode Substrate Integrated Waveguide: A New Guided Wave Structure for Microwave and Millimeter Wave Application," *IRMMW-THz*, pp. 219, 2006.

[17] Ansoft HFSS, ver. 10, ANSYS, Inc., Canonsburg, PA. Available: http: //www.ansoft.com/products/hf/hfss/

[18] X.-P. Chen, K. Wu, and Z.-L. Li, "Dual-Band and Triple-Band Substrate Integrated Waveguide Filters with Chebyshev and Quasi-Elliptic Responses," *IEEE Trans. Microwave Theory Tech.*, vol. MTT-55, pp. 2569-2578, 2007.

[19] D. Deslandes and K. Wu, "Accurate Modeling, Wave Mechanisms, and Design Considerations of a Substrate Integrated Waveguide," *IEEE Trans. Microwave Theory Tech.*, vol. MTT-54, pp. 2516-2526, 2006.

[20] ZVA40 vector analyzer, Rohde & Schwarz, Co., Munich, Germany. Available: http: //www2.rohde-schwarz.com/en/products/test_and_measurement/network_analysis/ZVA/.

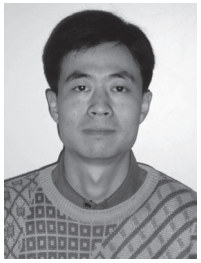

Wei Shao received the M.Sc. degree and Ph.D. degrees in Radio Physics from the University of Electronic Science and Technology of China (UESTC), Chengdu, China, in 2004 and 2006, respectively.

He joined the UESTC and is now an associate professor there. He has been a Visiting Scholar in the Electromagnetic Communication Laboratory, Pennsylvania State University in 2010. His research interests include the computational electromagnetic, EMC design, and antenna technique.

Jia-Lin Li received the M.Sc. degree from UESTC, Chengdu, China, in 2004, and the Ph.D. degree from the City University of Hong Kong, Hong Kong, in 2009, both in Electronic Engineering. Since Sept. 2009, he has been with the Institute of Applied Physics, School of Physical Electronics, UESTC, where he is currently a Professor. His research interests include the high performance active/passive microwave/millimeter-wave antennas, circuits and systems realized on PCB, multilayer PCB, LTCC, etc.

2011 INSTITUTIONAL MEMBERS

DTIC-OCP LIBRARY
8725 John J. Kingman Rd, Ste 0944
Fort Belvoir, VA 22060-6218

AUSTRALIAN DEFENCE LIBRARY
Northcott Drive
Canberra, A.C.T. 2600 Australia

BEIJING BOOK CO, INC
701 E Linden Avenue
Linden, NJ 07036-2495

DARTMOUTH COLLEGE
6025 Baker/Berry Library
Hanover, NH 03755-3560

DSTO EDINBURGH
AU/33851-AP, PO Box 830470
Birmingham, AL 35283

SIMEON J. EARL – BAE SYSTEMS
W432A, Warton Aerodome
Preston, Lancs., UK PR4 1AX

ENGINEERING INFORMATION, INC
PO Box 543
Amsterdam, Netherlands 1000 Am

ETSE TELECOMUNICACION
Biblioteca, Campus Lagoas
Vigo, 36200 Spain

GA INSTITUTE OF TECHNOLOGY
EBS-Lib Mail code 0900
74 Cherry Street
Atlanta, GA 30332

TIMOTHY HOLZHEIMER
Raytheon
PO Box 1044
Rockwall, TX 75087

HRL LABS, RESEARCH LIBRARY
3011 Malibu Canyon
Malibu, CA 90265

IEE INSPEC
Michael Faraday House
6 Hills Way
Stevenage, Herts UK SG1 2AY

INSTITUTE FOR SCIENTIFIC INFO.
Publication Processing Dept.
3501 Market St.
Philadelphia, PA 19104-3302

LIBRARY – DRDC OTTAWA
3701 Carling Avenue
Ottawa, Ontario, Canada K1A OZ4

LIBRARY of CONGRESS
Reg. Of Copyrights
Attn: 407 Deposits
Washington DC, 20559

LINDA HALL LIBRARY
5109 Cherry Street
Kansas City, MO 64110-2498

MISSOURI S&T
400 W 14th Street
Rolla, MO 56409

MIT LINCOLN LABORATORY
Periodicals Library
244 Wood Street
Lexington, MA 02420

NATIONAL CHI NAN UNIVERSITY
Lily Journal & Book Co, Ltd
20920 Glenbrook Drive
Walnut, CA 91789-3809

JOHN NORGARD
UCCS
20340 Pine Shadow Drive
Colorado Springs, CO 80908

OSAMA MOHAMMED
Florida International University
10555 W Flagler Street
Miami, FL 33174

NAVAL POSTGRADUATE SCHOOL
Attn:J. Rozdal/411 Dyer Rd./ Rm 111
Monterey, CA 93943-5101

NDL KAGAKU
C/0 KWE-ACCESS
PO Box 300613 (JFK A/P)
Jamaica, NY 11430-0613

OVIEDO LIBRARY
PO BOX 830679
Birmingham, AL 35283

DAVID PAULSEN
E3Compliance
1523 North Joe Wilson Road
Cedr Hill, TX 75104-1437

PENN STATE UNIVERSITY
126 Paterno Library
University Park, PA 16802-1808

DAVID J. PINION
1122 E Pike Street #1217
SEATTLE, WA 98122

KATHERINE SIAKAVARA
Gymnasiou 8
Thessaloniki, Greece 55236

SWETS INFORMATION SERVICES
160 Ninth Avenue, Suite A
Runnemede, NJ 08078

YUTAKA TANGE
Maizuru Natl College of Technology
234 Shiroya
Maizuru, Kyoto, Japan 625-8511

TIB & UNIV. BIB. HANNOVER
DE/5100/G1/0001
Welfengarten 1B
Hannover, Germany 30167

UEKAE
PO Box 830470
Birmingham, AL 35283

UNIV OF CENTRAL FLORIDA
4000 Central Florida Boulevard
Orlando, FL 32816-8005

UNIVERSITY OF COLORADO
1720 Pleasant Street, 184 UCB
Boulder, CO 80309-0184

UNIVERSITY OF KANSAS – WATSON
1425 Jayhawk Blvd 210S
Lawrence, KS 66045-7594

UNIVERSITY OF MISSISSIPPI
JD Williams Library
University, MS 38677-1848

UNIVERSITY LIBRARY/HKUST
Clear Water Bay Road
Kowloon, Honk Kong

CHUAN CHENG WANG
8F, No. 31, Lane 546
MingCheng 2nd Road, Zuoying Dist
Kaoshiung City, Taiwan 813

THOMAS WEILAND
TU Darmstadt
Schlossgartenstrasse 8
Darmstadt, Hessen, Germany 64289

STEVEN WEISS
US Army Research Lab
2800 Powder Mill Road
Adelphi, MD 20783

YOSHIHIDE YAMADA
NATIONAL DEFENSE ACADEMY
1-10-20 Hashirimizu
Yokosuka, Kanagawa,
Japan 239-8686

APPLIED COMPUTATIONAL ELECTROMAGNETICS SOCIETY JOURNAL
http://aces.ee.olemiss.edu

INFORMATION FOR AUTHORS

PUBLICATION CRITERIA

Each paper is required to manifest some relation to applied computational electromagnetics. **Papers may address general issues in applied computational electromagnetics, or they may focus on specific applications, techniques, codes, or computational issues.** While the following list is not exhaustive, each paper will generally relate to at least one of these areas:

1. **Code validation.** This is done using internal checks or experimental, analytical or other computational data. Measured data of potential utility to code validation efforts will also be considered for publication.

2. **Code performance analysis.** This usually involves identification of numerical accuracy or other limitations, solution convergence, numerical and physical modeling error, and parameter tradeoffs. However, it is also permissible to address issues such as ease-of-use, set-up time, run time, special outputs, or other special features.

3. **Computational studies of basic physics.** This involves using a code, algorithm, or computational technique to simulate reality in such a way that better, or new physical insight or understanding, is achieved.

4. **New computational techniques** or new applications for existing computational techniques or codes.

5. **"Tricks of the trade"** in selecting and applying codes and techniques.

6. **New codes, algorithms, code enhancement, and code fixes.** This category is self-explanatory, but includes significant changes to existing codes, such as applicability extensions, algorithm optimization, problem correction, limitation removal, or other performance improvement. **Note: Code (or algorithm) capability descriptions are not acceptable, unless they contain sufficient technical material to justify consideration.**

7. **Code input/output issues.** This normally involves innovations in input (such as input geometry standardization, automatic mesh generation, or computer-aided design) or in output (whether it be tabular, graphical, statistical, Fourier-transformed, or otherwise signal-processed). Material dealing with input/output database management, output interpretation, or other input/output issues will also be considered for publication.

8. **Computer hardware issues.** This is the category for analysis of hardware capabilities and limitations of various types of electromagnetics computational requirements. Vector and parallel computational techniques and implementation are of particular interest.

Applications of interest include, but are not limited to, antennas (and their electromagnetic environments), networks, static fields, radar cross section, inverse scattering, shielding, radiation hazards, biological effects, biomedical applications, electromagnetic pulse (EMP), electromagnetic interference (EMI), electromagnetic compatibility (EMC), power transmission, charge transport, dielectric, magnetic and nonlinear materials, microwave components, MEMS, RFID, and MMIC technologies, remote sensing and geometrical and physical optics, radar and communications systems, sensors, fiber optics, plasmas, particle accelerators, generators and motors, electromagnetic wave propagation, non-destructive evaluation, eddy currents, and inverse scattering.

Techniques of interest include but not limited to frequency-domain and time-domain techniques, integral equation and differential equation techniques, diffraction theories, physical and geometrical optics, method of moments, finite differences and finite element techniques, transmission line method, modal expansions, perturbation methods, and hybrid methods.

Where possible and appropriate, authors are required to provide statements of quantitative accuracy for measured and/or computed data. This issue is discussed in "Accuracy & Publication: Requiring, quantitative accuracy statements to accompany data," by E. K. Miller, *ACES Newsletter*, Vol. 9, No. 3, pp. 23-29, 1994, ISBN 1056-9170.

SUBMITTAL PROCEDURE

All submissions should be uploaded to ACES server through ACES web site (http://aces.ee.olemiss.edu) by using the upload button, journal section. Only pdf files are accepted for submission. The file size should not be larger than 5MB, otherwise permission from the Editor-in-Chief should be obtained first. Automated acknowledgment of the electronic submission, after the upload process is successfully completed, will be sent to the corresponding author only. It is the responsibility of the corresponding author to keep the remaining authors, if applicable, informed. Email submission is not accepted and will not be processed.

EDITORIAL REVIEW

In order to ensure an appropriate level of quality control, papers are peer reviewed. They are reviewed both for technical correctness and for adherence to the listed guidelines regarding information content and format.

PAPER FORMAT

Only camera-ready electronic files are accepted for publication. The term **"camera-ready" means that the material is neat, legible, reproducible, and in accordance with the final version format listed below.**

The following requirements are in effect for the final version of an ACES Journal paper:

1. The paper title should not be placed on a separate page.

The title, author(s), abstract, and (space permitting) beginning of the paper itself should all be on the first page. The title, author(s), and author affiliations should be centered (center-justified) on the first page. The title should be of font size 16 and bolded, the author names should be of font size 12 and bolded, and the author affiliation should be of font size 12 (regular font, neither italic nor bolded).

2. An abstract is required. The abstract should be a brief summary of the work described in the paper. It should state the computer codes, computational techniques, and applications discussed in the paper (as applicable) and should otherwise be usable by technical abstracting and indexing services. The word "Abstract" has to be placed at the left margin of the paper, and should be bolded and italic. It also should be followed by a hyphen (—) with the main text of the abstract starting on the same line.

3. All section titles have to be centered and all the title letters should be written in caps. The section titles need to be numbered using roman numbering (I. II. ….)

4. Either British English or American English spellings may be used, provided that each word is spelled consistently throughout the paper.

5. Internal consistency of references format should be maintained. As a guideline for authors, we recommend that references be given using numerical numbering in the body of the paper (with numerical listing of all references at the end of the paper). The first letter of the authors' first name should be listed followed by a period, which in turn, followed by the authors' complete last name. Use a coma (,) to separate between the authors' names. Titles of papers or articles should be in quotation marks (" "), followed by the title of journal, which should be in italic font. The journal volume (vol.), issue number (no.), page numbering (pp.), month and year of publication should come after the journal title in the sequence listed here.

6. Internal consistency shall also be maintained for other elements of style, such as equation numbering. Equation numbers should be placed in parentheses at the right column margin. All symbols in any equation have to be defined before the equation appears or right immediately following the equation.

7. The use of SI units is strongly encouraged. English units may be used as secondary units (in parentheses).

8. Figures and tables should be formatted appropriately (centered within the column, side-by-side, etc.) on the page such that the presented data appears close to and after it is being referenced in the text. When including figures and tables, all care should be taken so that they will appear appropriately when printed in black and white. For better visibility of paper on computer screen, it is good to make color figures with different line styles for figures with multiple curves. Colors should also be tested to insure their ability to be distinguished after black and white printing. Avoid the use of large symbols with curves in a figure. It is always better to use different line styles such as solid, dotted, dashed, etc.

9. A figure caption should be located directly beneath the corresponding figure, and should be fully justified.

10. The intent and meaning of all text must be clear. For authors who are not masters of the English language, the ACES Editorial Staff will provide assistance with grammar (subject to clarity of intent and meaning). However, this may delay the scheduled publication date.

11. Unused space should be minimized. Sections and subsections should not normally begin on a new page.

ACES reserves the right to edit any uploaded material, however, this is not generally done. It is the author(s) responsibility to provide acceptable camera-ready files in pdf and MSWord formats. Incompatible or incomplete files will not be processed for publication, and authors will be requested to re-upload a revised acceptable version.

COPYRIGHTS AND RELEASES

Each primary author must execute the online copyright form and obtain a release from his/her organization vesting the copyright with ACES. Both the author(s) and affiliated organization(s) are allowed to use the copyrighted material freely for their own private purposes.

Permission is granted to quote short passages and reproduce figures and tables from and ACES Journal issue provided the source is cited. Copies of ACES Journal articles may be made in accordance with usage permitted by Sections 107 or 108 of the U.S. Copyright Law. This consent does not extend to other kinds of copying, such as for general distribution, for advertising or promotional purposes, for creating new collective works, or for resale. The reproduction of multiple copies and the use of articles or extracts for commercial purposes require the consent of the author and specific permission from ACES. Institutional members are allowed to copy any ACES Journal issue for their internal distribution only.

PUBLICATION CHARGES

All authors are allowed for 8 printed pages per paper without charge. Mandatory page charges of $75 a page apply to all pages in excess of 8 printed pages. Authors are entitled to one, free of charge, copy of the printed journal issue in which their paper was published. Additional reprints are available for $ 50. Requests for additional re-prints should be submitted to the managing editor or ACES Secretary.

Corresponding author is required to complete the online form for the over page charge payment right after the initial acceptance of the paper is conveyed to the corresponding author by email.

ACES Journal is abstracted in INSPEC, in Engineering Index, DTIC, Science Citation Index Expanded, the Research Alert, and to Current Contents/Engineering, Computing & Technology.